A&A 669, A83 (2023)
https://doi.org/10.1051/0004-6361/202243801

Astronomy & Astrophysics

High-redshift quasars along the main sequence⋆,⋆⋆

A. Deconto-Machado[1], A. del Olmo Orozco[1], P. Marziani[2], J. Perea[1], and G. M. Stirpe[3]

[1] Instituto de Astrofísica de Andalucía, IAA-CSIC, Glorieta de la Astronomia s/n, 18008 Granada, Spain
e-mail: adeconto@iaa.es, chony@iaa.es
[2] INAF, Osservatorio Astronomico di Padova, vicolo dell' Osservatorio 5, 35122 Padova, Italy
e-mail: paola.marziani@inaf.it
[3] INAF, Osservatorio di Astrofisica e Scienza dello Spazio, Via Gobetti 93/3, 40129 Bologna, Italy

Received 16 April 2022 / Accepted 7 November 2022

ABSTRACT

Context. The 4D Eigenvector 1 empirical formalism (4DE1) and its main sequence (MS) for quasars has emerged as a powerful tool for organising the diversity among quasar populations, as several key observational measures and physical parameters are systematically changing along it.

Aims. Trends revealed by 4DE1 are very well established to explain all the diverse characteristics seen in low-redshift quasar samples. Nevertheless, the situation is far less clear when dealing with high-luminosity and high-redshift sources. Here, we aim to evaluate the behaviour of our sample of 22 quasars at high redshift ($2.2 \leq z \leq 3.7$) and high luminosity ($47.39 \leq L_{\rm bol} \leq 48.36$) in the context of the 4DE1.

Methods. Our approach involves studying quasar physics through a spectroscopic exploration of UV and optical emission line diagnostics. We used new observations from the ISAAC instrument at ESO-VLT and primarily from the SDSS to cover the optical and the UV rest-frames, respectively. The emission lines were characterised both via a quantitative parametrisation of the line profiles and a decomposition of the emission line profiles using multicomponent fitting routines.

Results. We provide spectrophotometric properties and line profile measurements for Hβ+[O III]$\lambda\lambda$4959,5007, as well as Si IVλ1397+O IV]λ1402, C IVλ1549+He IIλ1640, and the 1900 Å blend (including Al IIIλ1860, Si III]λ1892, and C III]λ1909). For six out of the 22 objects, a significantly blueshifted component on the Hβ profile is present. In 14 out of 22 cases, an Hβ outflowing component associated with [O III] is detected. The majority of [O III]$\lambda\lambda$4959,5007 emission line profiles show blueshifted velocities higher than 250 km s^{-1}. We find extremely broad [O III]$\lambda\lambda$4959,5007 emission that is comparable to the width of Hβ broad profile in some highly accreting quasars. The [O III]$\lambda\lambda$4959,5007 and C IVλ1549 blueshifts show very high amplitudes and a high degree of correlation. The line widths and shifts are correlated for both [O III]$\lambda\lambda$4959,5007 and C IVλ1549, suggesting that emission from outflowing gas is providing a substantial broadening effect to both lines. Otherwise, the links between C IVλ1549 centroid velocity at half intensity ($c(1/2)$), Eddington ratio ($L/L_{\rm Edd}$), and bolometric luminosity are found to be in agreement with previous studies of high-luminosity quasars.

Conclusions. Our analysis suggests that the behaviour of quasars of very high luminosity all along the main sequence is strongly affected by powerful outflows involving a broad range of spatial scales. The main sequence correlations remain valid at high redshift and high luminosity even if a systematic increase in line width is observed. Scaling laws based on UV Al IIIλ1860 and Hβ emission lines are equally reliable estimators of $M_{\rm BH}$.

Key words. quasars: general – quasars: emission lines – quasars: supermassive black holes

1. Introduction

The nature of the many differences seen in quasar spectra has been a key topic of interest in recent years and it continues to be a topic of active discussion. One of the first successful attempts to define the systematic trends of quasar spectra was carried out by Boroson & Green (1992). These authors organised the relations between the optical and radio spectral ranges into an Eingenvector 1 scheme based on studies of the 80 quasars from the Palomar-Green sample (Schmidt & Green 1983) and using a principal component analysis (PCA). This scheme primarily considers the anticorrelation seen between the optical Fe II strength and peak intensity of the [O III]λ5007 emission line as well as the full width at half maximum (FWHM) of the broad component of Hβ (H$\beta_{\rm BC}$, typically $\gtrsim$4000 km s^{-1}). A more overarching possibility for the arrangement of the individual characteristics found in the quasar spectra has been suggested by Sulentic et al. (2000a), taking into account several observational measures in the optical, UV, and X-ray spectral ranges as well as physical parameters such as outflow relevance and accretion mode. According to those authors, it is possible to organise the quasar diversity into a fourth dimensional (4D) correlation space known as Eigenvector 1 (4DE1).

One of the four key parameters considered by the 4DE1 is the FWHM of the Hydrogen Hβ broad component. Since the emission of Balmer lines like Hβ are thought to be arising from the quasar broad line region (BLR), this parameter can be used to measure black hole mass assuming gas to be virialised (Collin-Souffrin & Lasota 1988; Small & Blandford 1992; Marziani et al. 1996; McLure & Jarvis 2002; McLure & Dunlop 2004; Sulentic et al. 2006a; Assef et al. 2011; Shen 2013;

⋆ Spectra are only available at the CDS via anonymous ftp to cdsarc.cds.unistra.fr (130.79.128.5) or via https://cdsarc.cds.unistra.fr/viz-bin/cat/J/A+A/669/A83

⋆⋆ Based on observations collected at ESO under programmes 083.B-0273(A) and 085.B-0162(A).

Gaskell & Harrington 2018, and references therein). In addition, 4DE1 also considers the ratio between the intensities of the blend of Fe II emission lines at 4570 Å and Hβ ($R_{\rm Fe\,II}$ = I(Fe IIλ4570)/I(Hβ)), which can be used for the estimation of physical properties of the BLR such as the ionisation state, the electron density, and the column density of the ionised gas (Ferland et al. 2009; Panda et al. 2020).

The other parameters of the 4DE1 are the blueshifts of high-ionisation lines (HILs) with respect to the quasar systemic redshift and the soft X-ray photon index ($\Gamma_{\rm soft}$). Examples of HILs include the C IVλ1549 emission line and they are considered a strong diagnostic of outflows; there is also some evidence that the optical and UV properties are related (Bachev et al. 2004; Du et al. 2016; Śniegowska et al. 2020). Similarly, the equivalent width of the optical Fe II contribution is seen as a measure of the thermal emission from the accretion disc (Singh et al. 1985; Walter & Fink 1993). The $R_{\rm Fe\,II}$, soft X-ray photon index, and the line width of Hβ are also significantly correlated among themselves (Wang et al. 1996; Boller et al. 1996; Sulentic et al. 2000b).

Explorations of the distribution of low-redshift ($z \lesssim 0.8$) quasars in the optical plane of the 4DE1 – defined by FWHM(H$\beta_{\rm BC}$) versus $R_{\rm Fe\,II}$ and referred to as the main sequence (MS) of quasars – have given rise to the identification of two main populations with very significant differences among their spectra (Zamfir et al. 2010). Population A quasars show low FWHM (usually $\leq$4000 km s^{-1}) and a wide range of $R_{\rm Fe\,II}$, while Population B sources present a very wide range of FWHM(H$\beta_{\rm BC}$) but usually small $R_{\rm Fe\,II}$ ($\lesssim$1.). Marziani et al. (2018) summarised more than 15 yr of discussion on the empirical parametrisation of the quasar properties and their trends as well as the ways physical parameters are related to the accretion rate and feedback seem to be changing along the MS, going from quasars with low Fe II emission and high black hole mass ($\gtrsim$10^9 $M_\odot$, Pop. B) to the extreme Pop. A, xA (Martínez-Aldama et al. 2018), with strong Fe II emission ($R_{\rm Fe\,II}$ > 1) and strong blueshifts in HILs such as C IVλ1549, indicating strong wind effects on the quasars (i.e. 'wind-dominated' sources, Richards et al. 2011).

The Eddington ratio as well as the orientation effect are seen as key properties in the MS context (Sulentic et al. 2000a; Marziani et al. 2001; Boroson 2002; Shen & Ho 2014; Sun & Shen 2015). The $R_{\rm Fe\,II}$ parameter along with the H$\beta_{\rm BC}$ FWHM can be associated with $L/L_{\rm Edd}$ (Marziani et al. 2001; Panda et al. 2019). Low values of the $L/L_{\rm Edd}$ (typically $\lesssim$0.2) are usually found in Pop. B sources, while Pop. A sources are found to be high accretors (in extreme cases reaching $L/L_{\rm Edd} \gtrsim 1$). Consequently, sources with the highest $R_{\rm Fe\,II}$ are thought to be the ones with the highest Eddington ratios. Consistent results were also reported by Du et al. (2016), denoting the strong correlation found between the Eddington ratio, shape of the broad profile of the Hβ emission line, and the flux ratio I(Hβ)/I(Fe II) as the fundamental plane of accreting black holes. According to these authors, the shape of both Lorentzian and Gaussian profiles may reveal details on the BLR dynamic and may be different depending on the Eddington ratio (cf. Collin et al. 2006; Kollatschny & Zetzl 2011). Regarding the width of the emission line profiles, the broadest sources that are more Gaussian-like due to a redward asymmetry can be seen as the sum of two Gaussians (usually a BC and a very broad component, VBC) and the sources that present a VBC, usually with $FWHM$ > 7000 km s^{-1}, are the ones displaying lower Eddington ratios (Marziani et al. 2003, 2019). However, the line width is believed to be highly influenced by source orientation and the Eddington ratio (Marziani et al. 2001; McLure & Jarvis 2002; Zamfir et al. 2008; Panda et al. 2019). Since it is likely that Hβ lines are emitted by flattened systems, orientation may affect the FWHM(Hβ), going from broader (bigger θ, with θ indicating the inclination of the source with respect to the line-of-sight) to narrower (smaller θ) profiles.

Of special relevance is also the issue of sources that are radio-loud. Only about 10% of quasars are strong emitters in radio. Zamfir et al. (2010) analysed ~470 low-redshift (z < 0.8) quasars from the SDSS DR5 (Adelman-McCarthy et al. 2007) and found that in general the radio-loud sources are located in the Pop. B domain of the MS, while the radio-quiet are found in both populations. The location of the radio-loud (RL) quasars seems to indicate different properties with respect to a large fraction of the radio-quiet (RQ) sources. However, the fact that the RQs are distributed in both populations (A and B) complicates the interpretation. For instance, radio-loud and a large fraction of radio-quiet quasars both present strong asymmetries towards red wavelengths in the emission line profiles (Marziani et al. 1996; Punsly 2010). The paucity of radio-loud Pop. A sources at low-z implies that the Eddington ratio and the black hole mass distributions are different for radio-quiet and radio-loud sources matched in redshift and luminosity (Woo & Urry 2002; Marziani et al. 2003; Fraix-Burnet et al. 2017). In the two cases, the radio-quiet quasars are the ones that usually present smaller masses and larger Eddington ratio. This is not necessarily true for sources at high redshift (Sikora et al. 2007; Marinello et al. 2020; Diana et al. 2022).

The 4DE1 formalism and especially the MS represent the most effective way to distinguish quasars according to their BLR structural and kinematic differences. It has been extensively analysed in samples at z < 0.8 (e.g. Zamfir et al. 2010; Negrete et al. 2018). Trends among the optical plane of the 4DE1 and the $L/L_{\rm Edd}$ (e.g. sources with strong $L/L_{\rm Edd}$ are usually found to have strong $R_{\rm Fe\,II}$) are also seen in high-luminosity high- and intermediate-redshift sources ($z \gtrsim 2$ and $L \gtrsim 47$, Yuan & Wills 2003; Netzer et al. 2004; Sulentic et al. 2004). However, high-z quasar samples that have been studied including NIR observations of the Hβ spectral range are relatively few (e.g. McIntosh et al. 1999; Capellupo et al. 2015; Coatman et al. 2016; Bischetti et al. 2017; Vietri et al. 2018, 2020; Matthews et al. 2021). One of the studies of high-z quasars under this context was performed by Marziani et al. (2009, hereafter M09). These authors analysed the optical region of 53 Hamburg-ESO sources in a redshift range of $z \approx$ 0.9–3.0 using VLT ISAAC spectra (Sulentic et al. 2004, 2006a, M09). Additional UV spectra were obtained for some of these sources and the results are reported by Sulentic et al. (2017, hereafter S17). The authors found that both Pop. A and Pop. B quasars present evidences of significant outflows at high redshift while at low z only Pop. A sources tend to show strong contribution of outflowing gas. Extreme Pop. A quasars (xA) in a redshift range of z = 2.0–2.9 and with an averaged bolometric luminosity of log $L \sim 47$ [erg s^{-1}] have been analysed in details on the UV region by Martínez-Aldama et al. (2018) using GTC spectra. These authors found that the xA sources at high z share the same characteristics of the sources at low redshift, albeit with the higher outflow velocities (reaching values of ~4000 km s^{-1}).

In this paper, we report new observations from VLT/ISAAC for 22 high-redshift and high-luminosity quasars, along with a data analysis of the UV and optical regions along the main sequence and discussion. Our goal is to improve the sampling of the MS and the understanding of high-z, high-luminosity quasars. To do so, we take advantage of previous high- and

Table 1. Source identification.

Source (1)	RA (J2000) (2)	Dec (J2000) (3)	z (4)	δz (5)	$m^{(b)}$ (6)	Band (7)	M_i (8)	$m_{\rm VCV10}$ (9)	$f_{\rm Radio}$ (mJy) $^{(h)}$ (10)	Survey (11)	Radio class (12)
HE 0001−2340	00 03 44.95	−23 23 54.7	2.2651 $^{(a)}$	0.0036	14.78	H	−29.68	16.70 $^{(c)}$	<2.70	NVSS	RQ
[HB89] 0029+073	00 32 18.37	+07 38 32.4	3.2798 $^{(a)}$	0.0055	15.12	K	−29.26	17.44 $^{(d)}$	<0.86	FIRST	RQ
CTQ 0408	00 41 31.49	−49 36 12.4	3.2540	0.0048	14.02	K	−29.86	16.10 $^{(d)}$	7.26	SUMSS	RI
SDSSJ005700.18+143737.7	00 57 00.19	+14 37 37.7	2.6638	0.0023	15.70	H	−29.06	17.96 $^{(e)}$	<2.70	NVSS	RQ
H 0055−2659	00 57 57.92	−26 43 14.1	3.6599	0.0062	15.50	K	−30.74	17.47 $^{(f)}$	<2.70	NVSS	RQ
SDSSJ114358.52+052444.9	11 43 58.52	+05 24 44.9	2.5703	0.0038	15.54	H	−29.47	17.27 $^{(e)}$	<0.96	FIRST	RQ
SDSSJ115954.33+201921.1	11 59 54.33	+20 19 21.1	3.4277	0.0068	15.13	K	−29.92	17.92 $^{(e)}$	<0.97	FIRST	RQ
SDSSJ120147.90+120630.2	12 01 47.91	+12 06 30.2	3.5136	0.0063	14.60	K	−29.76	18.16 $^{(e)}$	<0.98	FIRST	RQ
SDSSJ132012.33+142037.1	13 20 12.34	+14 20 37.1	2.5356	0.0023	15.52	H	−28.87	17.82 $^{(e)}$	<0.98	FIRST	RQ
SDSSJ135831.78+050522.8	13 58 31.79	+05 05 22.7	2.4627	0.0020	15.40	H	−29.21	17.33 $^{(e)}$	<0.94	FIRST	RQ
Q 1410+096	14 13 21.05	+09 22 04.8	3.3240	0.0029	14.83	K	−29.44	17.80 $^{(g)}$	<0.99	FIRST	RQ
SDSSJ141546.24+112943.4	14 15 46.23	+11 29 43.4	2.5531	0.0043	14.53	H	−29.40	17.23 $^{(e)}$	7.80	NVSS	RI
B1422+231	14 24 38.10	+22 56 01.0	3.6287	0.0031	12.66	K	−29.85	15.84 $^{(e)}$	273.42	FIRST	RL
SDSSJ153830.55+085517.0	15 38 30.55	+08 55 17.1	3.5554	0.0060	14.72	K	−30.07	17.98 $^{(e)}$	<1.02	FIRST	RQ
SDSSJ161458.33+144836.9	16 14 58.34	+14 48 36.9	2.5698	0.0022	15.23	H	−29.41	17.43 $^{(e)}$	<0.94	FIRST	RQ
PKS 1937−101	19 39 57.30	−10 02 41.0	3.7908	0.0032	13.81	K	−30.40	17.00 $^{(g)}$	838.30	NVSS	RL
PKS 2000−330	20 02 24.00	−32 51 47.0	3.7899	0.0033	15.15	K	−30.99	17.30 $^{(g)}$	446.00	NVSS	RL
SDSSJ210524.49+000407.3	21 05 24.47	+00 04 07.3	2.3445	0.0020	14.59	H	−29.96	16.98 $^{(e)}$	3.20	NVSS	RI
SDSSJ210831.56−063022.5	21 08 31.56	−06 30 22.6	2.3759 $^{(a)}$	0.0016	15.77	H	−29.11	17.41 $^{(e)}$	<1.18	FIRST	RQ
SDSSJ212329.46−005052.9	21 23 29.46	−00 50 52.9	2.2800	0.0017	14.61	H	−29.76	16.62 $^{(e)}$	<0.96	FIRST	RQ
PKS 2126−15	21 29 12.10	−15 38 42.0	3.2987	0.0042	14.22	K	−29.88	17.00 $^{(g)}$	589.70	NVSS	RL
SDSSJ235808.54+012507.2	23 58 08.62	+01 24 34.8	3.4009	0.0029	14.84	K	−29.58	17.50 $^{(d)}$	<0.96	FIRST	RQ

Notes. $^{(a)}$Redshift estimation based on the [O III]λ5007. $^{(b)}$2MASS magnitude. $^{(c)}m_{\rm O}$. $^{(d)}m_{\rm R}$. $^{(e)}m_{\rm B}$. $^{(f)}$Photographic $m_{\rm B}$. $^{(g)}m_{\rm V}$. $^{(h)}$Values with < are the upper limits.

low-z samples and perform a comparison between the different data under the 4DE1 context. Details on the sample and on the observations are presented in Sects. 2 and 3. The procedures and the approach followed during the line decomposition are presented in detail on Sect. 4. Results on the complete analysis of both optical (Hβ+[O III]$\lambda\lambda$4959,5007) and UV (Si IVλ1392, C IVλ1549, and the 1900 Å blend) regions are reported in Sect. 5. Additional discussions are provided in Sect. 6. In Sect. 7, we list the main conclusions of our work.

2. The sample

Our sample consists of 22 quasars with high redshift, going from $z = 2.2$ to $z = 3.7$, and with high luminosity ($47.39 \leq \log L_{\rm bol} \leq 48.36$ [erg s^{-1}]), including both radio-loud and radio-quiet sources that were observed under the ESO programmes 083.B-0273(A) and 085.B-0162(A). These sources were selected from the Hamburg-ESO survey (HE, Wisotzki et al. 2000), which consists of a flux-limited ($m_{\rm B} \approx 17.5$), colour-selected survey with a redshift range $0 \lesssim z \lesssim 3.2$. Our sample covers a redshift that allows for the detection and observation of the Hβ+[O III]$\lambda\lambda$4959,5007 region through the transparent window in the near-infrared with the ISAAC spectrograph at VLT (Sulentic et al. 2006a, 2017). There is also a cut in δ at +25° due to the geographic location of the telescope. Table 1 presents the main properties of our sample, reporting the source identification according to the different catalogues (Col. 1); right ascension and declination at J2000 coordinates (Cols. 2 and 3, respectively); redshift estimated as explained in Sect. 2.1 (Col. 4); redshift uncertainties (Col. 5); the H- or K-band (depending on the range of the spectrum) apparent magnitude m_H or m_K from the 2-MASS catalogue (Col. 6); the respective band (H or K, Col. 7); the i-band absolute magnitude M_i (Col. 8) estimated for our data; the apparent magnitude from Véron-Cetty & Véron (2010; Col. 9); the radio flux in mJy (Col. 10) in the frequency of the survey listed in Col. 11; radio classification according Ganci et al. (2019) is shown in Col. 12 and explained in Sect. 3.3. The k-correction used is the one available on Richards et al. (2006) for sources with similar redshift and the galactic extinction were collected from the DR16 catalogue (Lyke et al. 2020). The luminosity distance was computed from the redshift using the approximation of Sulentic et al. (2006a), valid for $\Omega_{\rm M} = 0.3$, $\Omega_\Lambda = 0.7$, and $H_0 = 70$ km s^{-1} Mpc^{-1}.

For all sources, we have computed synthetic magnitudes H or K from our flux-calibrated spectra, and we have compared them with the 2MASS H- and K-band apparent magnitudes. In cases in which the difference between our m synthetic magnitudes and the 2MASS catalogue magnitudes is higher than 0.5 mag we use the m from 2MASS (these sources are identified in Table 1). Also, in one very special source (B1422+231) a magnification correction is applied lowering the flux by a factor of 6.6, which leads to a change in the magnitude, since this source is a gravitationally lensed quasar with four images (Patnaik et al. 1992; Assef et al. 2011; see Appendix A for notes on individual objects). Apart from the well-known lensed quasar B1422+231, our sample includes other quasars known or suspected to undergo micro-lensing: SDSSJ141546.24+112943.4 (Sluse et al. 2012; Takahashi & Inoue 2014) and some candidates, as [HB89] 0029+073 (Jaunsen et al. 1995), but we did not apply any magnitude correction for lensing on these sources.

2.1. Redshift estimations and sample location in the Hubble diagram

Redshift measurements were based on the Hβ emission line profile and were obtained from the observed wavelength of the Hβ narrow component ($FWHM \lesssim 1000$ km s^{-1}). The values are reported in Table 1. In the case of HE 0001−2340 and SDSSJ210831.56−063022.5 the redshift was estimated through the [O III]λ5007 emission line, due to the difficulty of isolating a

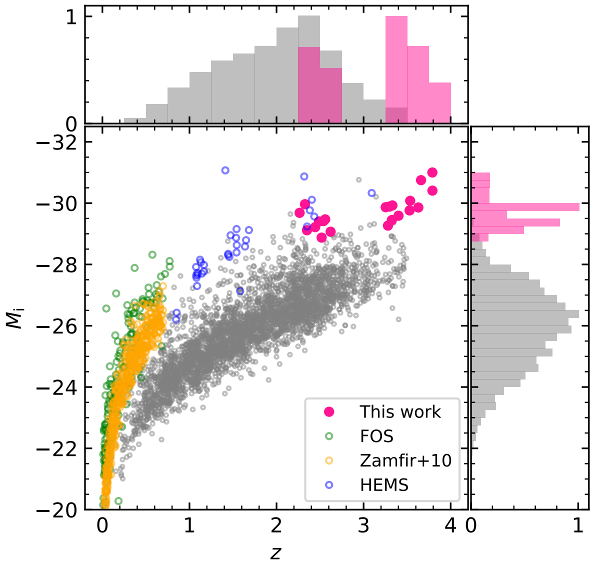

Fig. 1. Location of the complete sample in the Hubble diagram (pink spots). Gray dots represent a random subsample of the DR16 catalogue from Lyke et al. (2020) and green, yellow, and blue dots represent the comparison samples defined in Sect. 2.2.

narrow component of Hβ. Before performing the spectral analysis, as described in Sect. 4, both optical and UV spectra are set at rest-frame using the IRAF task `dopcor`.

Figure 1 shows the location of the objects of the sample (pink spots) in the i-band absolute magnitude M_i versus redshift plane. Our sample as well as the comparison samples (defined in Sect. 2.2) are located at the high end of the luminosity distribution when compared with the SDSS DR16 data (grey spots, Lyke et al. 2020). Moreover, some of our sources are well located within the region with the highest values of the SDSS redshift distribution for quasars.

2.2. Comparison samples

We chose comparison samples that include high and low redshifts, as well as high- and low-luminosity sources that have been studied in the recent literature, as follows:

Low-z SDSS sources. Zamfir et al. (2008, 2010) analysed ~470 low-redshift ($z \leq 0.7$) quasars with high signal-to-noise ($S/N \sim 29$) ratio optical spectra observed with the Sloan Digital Sky Survey data release (DR) 5 (Adelman-McCarthy et al. 2007), including both radio-loud and radio-quiet sources. This sample covers a wide range of bolometric luminosity, going from $\log L_{\rm bol} = 10^{43}$ to $\log L_{\rm bol} = 10^{47}$ erg s^{-1}.

High-luminosity Hamburg-ESO sample (hereafter, HEMS). Sulentic et al. (2004, 2006a) and M09 obtained, using the VLT-ISAAC camera, Hβ region measurements for a sample of 53 high-redshift high-luminosity objects, selected from the Hamburg-ESO survey. The sources are extremely luminous ($47 \lesssim L_{\rm bol} \lesssim 48$) and are located in a redshift range of $0.9 \lesssim z \lesssim 3.1$. We use these data as comparison sample at high L, for both Hβ and [O III] lines. For the UV region we use the results provided by S17, who studied 28 quasars of the previous sample, and from which they obtained C IVλ1549 observations with the VLT and TNG telescopes. The redshift range of the HEMS is $1.4 \leq z \leq 3.1$ and a typical bolometric luminosity is $L_{\rm bol} \gtrsim 10^{47.5}$ erg s^{-1}. The location of the HEMS in the Hubble diagram is similar to the one of our data (Fig. 1) in terms of absolute magnitudes, although a large fraction of HE sources displays $1 \lesssim z \lesssim 2$.

Low-luminosity FOS data. The low-luminosity Faint Object Spectrograph (FOS) comparison sample was selected from Sulentic et al. (2007, S07 from now on), where the authors analysed the C IV line parameters. Marziani et al. (2003, hereafter M03) provide measurements on the Hβ emission line for most sources in this sample. The typical bolometric luminosity of this sample is $\log L_{\rm bol} \sim 45.6$ [erg s^{-1}] and a redshift range $z \leq 0.5$.

Table 2. Log of optical observations with VLT/ISAAC.

Source	Date obs. (start)	Band	DIT (s)	$N_{\rm exp}$	Airmass start-end	Averaged seeing
(1)	(2)	(3)	(4)	(5)	(6)	(7)
HE 0001−2340	2010-07-06	*sH*	180	12	1.05−1.02	1.03
	2010-07-24	*sH*	180	12	1.03−1.01	0.55
	2010-08-04	*sH*	180	12	1.06−1.12	1.44
[HB89] 0029+073	2009-09-03	*sK*	180	20	1.43−1.25	1.08
	2010-07-08	*sK*	180	20	1.25−1.19	0.49
	2010-08-04	*sK*	180	20	1.19−1.18	1.31
CTQ 0408	2009-07-09	*sK*	180	8	1.11−1.12	0.51
	2009-08-31	*sK*	180	8	1.11−1.12	3.05
SDSSJ005700.18+143737.7	2009-09-04	*sH*	180	28	1.44−1.98	1.99
H 0055−2659	2009-09-02	*sK*	180	40	1.01−1.23	1.25
SDSSJ114358.52+052444.9	2009-07-08	*sH*	180	20	1.34−1.67	0.83
SDSSJ115954.33+201921.1	2010-04-05	*sK*	175	24	2.35−1.69	1.08
SDSSJ120147.90+120630.2	2010-04-15	*sK*	180	20	1.92−1.49	1.23
SDSSJ132012.33+142037.1	2009-05-04	*sH*	180	24	1.36−1.28	1.37
SDSSJ135831.78+050522.8	2010-04-18	*sH*	180	20	1.23−1.18	0.73
Q 1410+096	2010-04-20	*sK*	180	28	1.45−1.23	0.83
SDSSJ141546.24+112943.4	2009-05-04	*sH*	180	20	1.24−1.26	0.50
B1422+231	2009-04-13	*sK*	180	12	1.50−1.48	0.98
SDSSJ153830.55+085517.0	2010-04-05	*sK*	180	20	1.20−1.24	1.14
SDSSJ161458.33+144836.9	2009-07-08	*sH*	180	20	1.33−1.30	1.35
	2009-09-22	*sH*	180	20	1.73−2.05	2.24
PKS 1937−101	2009-09-03	*sK*	180	12	1.13−1.23	1.07
PKS 2000−330	2009-08-31	*sK*	180	20	1.43−1.89	2.03
SDSSJ210524.49+000407.3	2010-07-23	*sH*	180	12	1.29−1.45	1.80
SDSSJ210831.56−063022.5	2010-06-19	*sH*	175	24	1.07−1.18	0.93
SDSSJ212329.46−005052.9	2010-07-08	*sH*	180	12	1.12−1.18	0.48
	2010-07-24	*sH*	180	12	1.41−1.27	0.90
PKS 2126−15	2009-09-01	*sK*	180	12	1.84−2.36	1.41
	2010-06-09	*sK*	180	16	1.26−1.12	1.07
SDSSJ235808.54+012507.2	2010-06-21	*sK*	180	20	1.25−1.13	1.01

3. Observations and data

3.1. Near-infrared observations and data reduction

Spectra were taken in service mode in 2009 and 2010, with the infrared spectrometer ISAAC, mounted at the Nasmyth B focus of VLT-U1 (Antu) until August 2009, and later at the Nasmyth A focus of VLT-U3 (Melipal) at the ESO Paranal Observatory. Table 2 summarises the NIR observations, listing the date of observation (Col. 2), used grating (Col. 3), individual detector integration time (DIT) in seconds (Col. 4), number of exposures with single exposure time equal to DIT (Col. 5), range of air mass of the observations (Col. 6), and the averaged seeing (Col. 7). When the source was observed more than once (HE 0001−2340, [HB89] 0029+073, CTQ 0408, SDSSJ161458.33+144836.9, SDSSJ212329.46−005052.9, and PKS 2126−15), we combine the individual spectra to obtain a median weighted final spectrum for the analysis. Spectral resolutions are $FWHM$ = 16 Å in the H band and $FWHM$ = 22 Å in the K band.

Reductions were performed using standard IRAF routines. Several spectra for each source were taken, nodding the telescope between two positions (nodding amplitude = 20″). Each obtained frame was divided by the flat field provided by the ESO automated reduction pipeline. The 1D spectra were extracted using the IRAF program 'apall'. Cosmic ray hits were eliminated by interpolation using a median filter, comparing the affected spectrum with the other spectra of the same source.

For each position along the slit, a 1D xenon/argon arc spectrum was extracted from the calibration lamp frame, using the same extraction parameters as the corresponding target spectrum. The wavelength calibration was well modeled by 3rd order Chebyshev polynomial fits to the positions of 15−30 lines, with rms residuals of 0.3 Å in sH and 0.6 Å in sK. The wavelength calibration is usually affected by a small 0-order offset caused by grism and telescope movement, because the arc lamp frames were obtained in the daytime. A correction for these shifts was obtained by measuring the centroids of 2−3 OH sky against the arc calibration and calculating the average difference, which reached at most 2−3 pixels in either direction. Once matched with the corresponding arc calibrations, the individual spectra of each source were rebinned to a common linear wavelength scale and stacked.

The spectra of the atmospheric standard stars were extracted and wavelength-calibrated in the same way. All clearly identifiable stellar features (H and HeI absorption lines) were eliminated from the stellar spectra by spline interpolation of the surrounding continuum intervals. Each target spectrum was then divided by its corresponding standard star spectrum in order to correct for the atmospheric absorption features. This was achieved with the IRAF routine 'telluric', which allows to optimise the correction with slight adjustments in shift and scaling of the standard spectrum. The correct flux calibration of each spectrum was achieved by scaling it according to the magnitude of the standard star and to the ratio of the respective DITs. Because the seeing often exceeded the width of the slit, significant light loss occurred and, therefore, the absolute flux scale of the spectra is not to be considered as accurate. However, in this long-wavelength range we consider the light losses to be independent of wavelength (i.e. we assume that differential atmospheric refraction is negligible) and thus they are not expected to affect the relative calibration of the spectra. We carried out an a posteriori evaluation of the absolute flux calibration uncertainty performing a comparison between the H/K-band magnitudes estimated by convolving the H/K filter with the observed spectrum and the H/K magnitudes in NED. The differences are smaller than 0.5 mag, except for SDSSJ132012.33+142037.1, SDSSJ141546.24+112943.4, and SDSSJ153830.55+085517.0, where a correction factor ∼0.880 ± 0.176 mag was applied.

3.2. UV

We found useful UV spectra (i.e. those including at least one of the three UV regions of our interest) for the 15/22 sources that are listed in Table 3, where we also list in Col. 2 the database and reference from which each spectrum was obtained and then the broad absorption line (BAL) quasars in Col. 3. We report the BAL sources as the analysis of the region in which the broad absorptions are located should be taken with care, once it demands the addition of absorption components in the fitting routine. The other seven quasars do not have useful UV spectra, either because they are old spectra that are not digitally available and have low S/N not suitable for accurate profile fitting, or because they do not include any of the three UV regions we want to analyse (Si IVλ1397+O IVλ1402, C IVλ1549+He IIλ1640, and the 1900 Å blend). For the UV spectral range (observed in the optical domain at the redshift of this sample), the spectra were collected mainly from the SDSS DR16 database (Ahumada et al. 2020, and references therein). For one source (PKS 2000−330), the UV spectrum was digitalised from Barthel et al. (1990). Four out of the 22 quasars (Q 1410+096, SDSSJ141546.24+112943.4, SDSSJ153830.55+085517.0, and SDSSJ210524.49+000407.3) are classified as BAL quasars, due to strong absorption lines (Gibson et al. 2009; Scaringi et al. 2009; Allen et al. 2011; Welling et al. 2014; Bruni et al. 2019; Yi et al. 2020).

Table 3. UV spectra information.

Source (1)	UV spect. (2)	Comments (3)
SDSSJ005700.18+143737.7	BOSS	
SDSSJ114358.52+052444.9	BOSS	
SDSSJ115954.33+201921.1	SDSS	
SDSSJ120147.90+120630.2	BOSS	
SDSSJ132012.33+142037.1	BOSS	
SDSSJ135831.78+050522.8	BOSS	
Q 1410+096	SDSS	BAL
SDSSJ141546.24+112943.4	SDSS	BAL
SDSSJ153830.55+085517.0	BOSS	BAL [(a)]
SDSSJ161458.33+144836.9	BOSS	
PKS 2000−330	Barthel et al. (1990)	
SDSSJ210524.49+000407.3	SDSS	BAL
SDSSJ210831.56−063022.5	SDSS	
SDSSJ212329.46−005052.9	BOSS	
SDSSJ235808.54+012507.2	BOSS	

Notes. [(a)]In this case, there is only a small but significant absorption close to Si IVλ1397 and do not affect the other UV emission lines that we are considering in the fittings.

3.3. Radio data

The radio fluxes presented in Table 1 were collected from the 1.4-GHz NRAO VLA Sky Survey (NVSS, Condon et al. 1998) and from the VLA FIRST Survey (Gregg et al. 1996; Becker et al. 1995). The flux in radio is reported for seven of our sources and in the case the object is not detected we provide an upper limit to the flux, which corresponds to the detection limit (≈5 times the rms in both FIRST and NVSS catalogue) at the position of the source. In the case of CTQ 0408, there is no coverage either in the FIRST survey or in the NVSS survey. The radio flux for this source is obtained at 408 MHz from the Sidney University Molonglo Sky Survey catalogue (Mauch et al. 2003). The radio classification is shown in Col. 12 of Table 1 and was determined following Ganci et al. (2019) via the estimation of a modified rest-frame radio loudness parameter $R_{\rm K} = f_{\nu,\rm radio}/f_{\nu,\rm optical}$ (Kellermann et al. 1989), defined as the ratio between the specific flux at 1.4 GHz and in the g-band. Accordingly, our sample is separated into three different ranges: radio-quiet (RQ; $R_{\rm K} < 10$), radio-intermediate (RI; $10 \leq R_{\rm K} < 70$), and radio-loud (RL; $R_{\rm K} \geq 70$). Of the seven sources with radio detection, three of them (CTQ 0408, SDSSJ141546.24+112943.4, and SDSSJ210524.49+000407.3) are classified as radio-intermediate. The radio-loud sources from our sample are B1422+231, PKS 1937−101, PKS 2000−330, and PKS 2126−15, about 20% of the sources of this sample. We

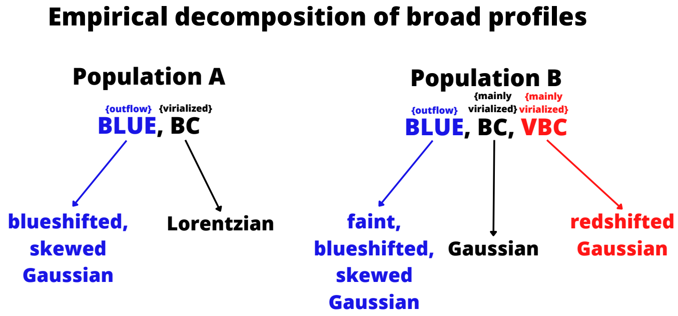

Fig. 2. Sketch of the approach followed for broad profile fittings.

plan to carry out a similar spectroscopic study focused on RL quasars to supplement those listed in Table 1 in a forthcoming paper.

4. Spectral analysis

4.1. Optical range: Multicomponent fitting

4.1.1. Hβ

The multicomponent fits were performed, after the spectra were set at rest-frame, using the SPECFIT routine from IRAF (Kriss 1994). This routine allows for simultaneous minimum-χ^2 fit of the continuum approximated by a power-law and the spectral line components yielding FWHM, peak wavelength, and intensity of all line components. In the optical range, we fit the Hβ profile as well as the [O III]$\lambda\lambda$4959, 5007 emission lines and the Fe II multiplets for the 22 objects.

Our approach includes the continuum (a power law), a semi-empirical scalable Fe II emission template and the emission line components to fit the Hβ+[O III]$\lambda\lambda$4959, 5007 region. The Fe II template used is almost identical to the one of Boroson & Green (1992). The specfit routine allows for the scaling, broadening, and shifting of the Fe II template to model the observed features (Marziani et al. 2003). A sketch illustrating the decomposition approach performed on the fits of the broad profiles for the is presented in Fig. 2. The fit of the Hβ full profile takes into account three main components:

Broad component (BC): this component is kept symmetric, set almost always at rest-frame, and presents a FWHM range that goes from $\gtrsim$3000 km s^{-1} for some Pop. A and $\lesssim$6000 km s^{-1} for Pop. B quasars. The profile changes depending on the quasar population, presenting a Lorentzian-like shape for Pop. A and a Gaussian-like one for Pop. B sources (Sulentic et al. 2002; Marziani et al. 2003; Zamfir et al. 2010; Cracco et al. 2016);

Blueshifted component (BLUE): our first assumption is to model this component by only a blue-shifted Gaussian (symmetric or skewed) profile with FWHM and shift similar to the [O III]$\lambda\lambda$4959,5007 semi-broad component (SBC, explained in Sect. 4.1.2). When the Hβ profile does not correspond to the blueshifted SBC of [O III]$\lambda\lambda$4959,5007 profile, it is included in the fitting an additional Gaussian blue-shifted component that may not belong to NLR emission (BLUE). Unlike the SBC, BLUE is believed to be associated with emission of outflowing gas from within the BLR (Negrete et al. 2018);

Very broad component (VBC): this is clearly observed in Population B sources (Sulentic et al. 2017; Wolf et al. 2020). It is always represented by a redshifted Gaussian profile and it is thought to be related with the high-ionisation virialised region closest to the continuum source (Peterson & Ferland 1986; Snedden & Gaskell 2007; Wang & Li 2011). This component can easily achieve $FWHM \gtrsim 10\,000$ km s^{-1}.

In addition, we include a narrow component (NC) superimposed to the broad emission line profile and it is fitted as an unshifted Gaussian. The population classification depends on the FWHM of the full profile. Depending on the population assignment, different components are included and they assume different line shapes. An exhaustive analysis of the fittings were performed and in borderline cases (i.e. with line width close to the boundary between Pop. A and B), the final conclusion on the population of the source is based on the χ^2 of the fitting (i.e. the fittings with the minimum χ^2 are selected).

4.1.2. [O III]$\lambda\lambda$4959,5007

An approach similar to the one used for Hβ is also followed for the [O III]$\lambda\lambda$4959, 5007 emission line profiles. The [O III]$\lambda\lambda$4959, 5007 full profile is assumed to be well represented by a Gaussian narrow ($FWHM \lesssim 1200$ km s^{-1}) component set at rest-frame or shifted to the blue and a semi-broad component (SBC, FWHM typically $\lesssim$3000 km s^{-1}) that usually appears more shifted to the blue (~1000 km s^{-1}, Zhang et al. 2011; Marziani et al. 2016a, 2022a). The NC is modelled as a Gaussian profile for the two populations and in a first approach the NC of both Hβ and [O III]$\lambda\lambda$4959,5007 share the same line width. The blueshifted contributions can be modelled by one or more Gaussian profiles and in some cases the Gaussian needs to be asymmetric towards the blue to account for the line shape, namely, to be a 'skewed' Gaussian. The use of a skewed Gaussian has a physical motivation, as it might be associated with bipolar outflow emission in which the receding side of the outflow is obscured. Apart from that, both [O III]λ4959 and [O III]λ5007 emission line profiles are assumed to have the same FWHM and shifts, and the intensity ratio between the two lines is kept fixed at 1:3 (Dimitrijević et al. 2007).

4.2. UV range: Multicomponent fitting

Fits were performed for three different regions centred on Si IVλ1397+O IV]λ1402, C IVλ1549+He IIλ1640, and the 1900 Å blend that includes the Al IIIλ1860 doublet, Si III]λ1892, Si IIλ1816, and C III]λ1909. The UV fittings are presented for 15 sources. The fits were not carried out in cases where the emission lines are strongly affected by BALs. The fittings of the absorption lines are performed in sources in which the presence of these lines allows to clearly see the emission line profile (as in the case of mini-BALs; Sulentic et al. 2006b). The UV blends are fit following the population assignments from the Hβ spectral range. The only exception is SDSSJ153830.55+085517.0, where its UV spectrum cannot be fitted in agreement with its classification as Pop. B in the Hβ region, as highlighted in the Appendix A.

4.2.1. 1900 Å blend

In the UV region corresponding to the 1900 Å blend, the fittings are performed considering the Al IIIλ1860 doublet, Si III]λ1892, Si IIλ1816, and C III]λ1909 emission line profiles. Here, Fe III is especially relevant on the red side of the 1900 Å blend and its modelling was performed using the Vestergaard & Wilkes (2001) empirical template, and following the same approach as for the optical Fe II. Broad line components of the 1900 Å blend in Pop. A sources are fitted by Lorentzian profiles while in Pop. B by Gaussian functions (as is the case of Hβ in the optical spectral range), keeping the same (or at least a comparable) FWHM to the broad component of Hβ.

In several Pop. A and more frequently in xA quasars, the Fe III template and the C III]λ1909 broad component do not adequately reproduce the shape of the red side of the 1900 Å blend. A better model of the C III]λ1909 region is achieved assuming an additional contribution mostly likely due to the Fe III line at 1914 Å. The same approach was employed in Martínez-Aldama et al. (2018).

Regarding the Pop. B sources, the C III]λ1909 emission line is well represented by the same combination applied for Pop. B Hβ: VBC+BC+NC. The VBC FWHM is expected to be ≥4000 km s^{-1}, and the NC $FWHM \sim 1000$ km s^{-1} (there is only one source that shows a significant NC in C III]). Differently from C III]λ1909, lines such as the Al IIIλ1860 doublet, Si III]λ1892, and Si IIλ1816 are assumed not to present a very broad component (Buendia-Rios et al. 2022). They are fit by only one BC.

4.2.2. C IVλ1549+He IIλ1640

In order to fit the C IVλ1549+He IIλ1640 blend and contaminant lines within it, we use the approach followed by S17. As in the previous fits, we represent Pop. A profiles of C IVλ1549 and He IIλ1640 by a broad and a blueshifted component. Pop. B are represented by the combination VBC+BC+BLUE. The broad components of C IVλ1549 and He IIλ1640 are fixed at rest-frame and the other components are left free to vary in wavelength. Nevertheless, the FWHM and shapes of He IIλ1640 BC and BLUE are restricted to be equal (or comparable) to the corresponding ones of C IVλ1549. These constraints are physically motivated since both C IVλ1549 and He IIλ1640 are expected to be emitted from the same regions, because of the similar ionisation potential of the parent ionic species. An additional condition is that the broad component (BC) of C IVλ1549 and He IIλ1640 FWHM should be equal or larger to the one of Hβ, following previous works (e.g. Sulentic et al. 2017, and references therein).

4.2.3. Si IVλ1397+O IV]λ1402

For the Si IVλ1397+O IV]λ1402 emission lines region, we follow the same steps as in the C IV+He II blend. The Si IVλ1397+O IV]λ1402 feature profile is similar to the one of C IVλ1549, and is therefore expected to present BC and blueshifted component similar to those of C IVλ1549. The broad component in this case is also kept at rest-frame and any other necessary component is free to change in all the parameters.

4.3. Analysis of the full profile parameters for the optical and UV regions

Apart from the multicomponent analysis, the Hβ and [O III] emission line profiles are also characterised through the parametrisation of the full profile by measuring centroids and widths at different fractional intensities (1/4, 1/2, 3/4, and 9/10), as well as asymmetry and kurtosis indexes in order to provide a quantitative description independent of the SPECFIT modelling. In the case of Hβ, the full profile (H$\beta_{\rm full}$) for Pop. B quasars is represented by BC+VBC plus BLUE when detected. For Pop. A quasars, full Hβ profile consists of BC plus BLUE if an additional blue component is present. For [O III] we consider NC and one (or more, if needed) blueshifted SBC. Full profile parameters for the UV region are provided for the C IVλ1549 broad emission line, excluding NC.

4.4. Error estimates

Uncertainties in the multicomponent fits were estimated by running Markov chain Monte Carlo (MCMC) simulations, following the approach described in Marziani et al. (2022b) for both optical and UV spectral ranges. Observed spectra were modeled using the components employed in the best fit, with a Markov chain to sample the domain around the minimum χ^2. The dispersion in the posterior distribution of a parameter was assumed to be its 1σ confidence interval. For the optical range, the errors are around the order of 10% for the FWHM of the H$\beta_{\rm BC}$ and [O III]$_{\rm SBC}$. Larger uncertainties (~30%) are found for the narrow components of both lines and for the blueshifted component of Hβ. Flux uncertainties for strong or sharp emission lines are ~10%, while typical errors for the continuum and Fe II are ~5% and ~15% respectively, if Fe II is reasonably strong. For the UV, the FWHM uncertainties are between 10% and 15% and errors on intensity measurements are usually ≲10% for the strongest emission line components.

5. Results

5.1. Location in the optical plane of main sequence

After performing the multicomponent fitting, we can locate the sample in the MS optical plane, using the FWHM(H$\beta_{\rm full}$) as well as the flux ratio of Fe IIλ4570 and Hβ, $R_{\rm Fe\,II}$. Figure 3 shows the location of the sources and a comparison between our sample and low- and high-z samples. The grey- and green-shaded areas in the plot indicate the location of low-redshift quasars on the MS, with the xA sources situated on the green shadow.

Our sample shows a slight displacement in the direction of increasing FWHM(Hβ), if compared to low-z samples (e.g. Zamfir et al. 2010, and the shaded area in Fig. 3). There are some Pop. A sources that present a FWHM(H$\beta_{\rm full}$) ~ 5000 km s^{-1}. The Pop. A-B boundary at FWHM(Hβ) = 4000 km s^{-1} is reasonable when considering low redshift and, consequently, lower luminosity ranges than those of high-z quasars (Sulentic et al. 2004). However, at high luminosity there is a significant effect on the Hβ profile width that may shift the boundary between Pop. A and B by more than 1000 km s^{-1} (M09). Up and bottom purple shadows in Fig. 3 indicate, respectively, the Pop. A-B boundary and the minimum FHWM(Hβ) found in a 47 ≤ log $L_{\rm bol}$ ≤ 48 range that are representative of our sample. Both boundaries were determined following M09.

Of the 22 sources of our sample, 12 are classified as Pop. A and 10 as Pop. B quasars. We found three sources to belong to spectral type (ST) A1; six Pop. A2; three Pop. A3 (extreme A); eight to be Pop. B1; and two Pop B2. The four radio-loud objects (B1422+231, PKS 1937−101, PKS 2000−330, and PKS 2126−15) are identified in Fig. 3 by the blue and red symbols surrounded by a open circle. Three of them are classified as Pop. A and only PKS 2126−15 is a Pop. B quasar. Of the three radio-intermediate, two (SDSSJ141546.24+112943.4, ST B2; SDSSJ210524.49+000407.3, A3) show significant Fe II and an overall spectrum associated with high accretion rates (Ganci et al. 2019; del Olmo et al. 2021; Marziani et al. 2022c). Only CTQ 0408 is classified as B1, with an optical spectrum resembling the powerful jetted sources at low z. The orientation may strongly affect the classification of the sources, especially

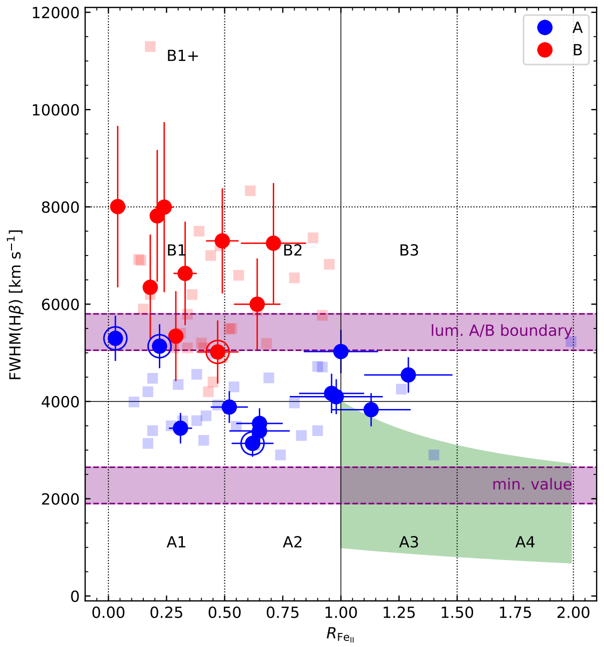

Fig. 3. Location of our sources through the optical plane of the 4DE1. Pop. A quasars are represented by blue circles and Pop. B by red circles. The radio-loud sources from the sample are surrounded by a circle in the plot. Grey and green regions indicate the distribution of the main sequence of quasars across the 4DE1 optical plane in a low-z context (Marziani et al. 2018). Spectral types (ST) of the MS are labelled according to Sulentic et al. (2002). Blue and red squares indicate high-redshift Pop. A and Pop. B quasars from M09, respectively. Purple-shaded areas show the luminosity-dependent boundary between Pops. A and B and the minimum FWHM value for sources with $47 \leq L_{\mathrm{bol}} \leq 48$ and assuming $\alpha = 0.67$ (Marziani et al. 2009).

Table 4. Spectrophotometric measurements on Hβ.

Source (1)	Spectral type (2)	$f_{\lambda,5100}$ [(a)] (3)	W(Hβ) (4)	W([O III]) [Å] (5)	$R_{\mathrm{Fe\,II}}$ (6)
		Population A			
SDSSJ005700.18+143737.7	A3	2.5 ± 0.3	53 ± 6	4.5 ± 0.5	1.13 ± 0.17
SDSSJ132012.33+142037.1	A1	1.2 ± 0.1	74 ± 9	19.8 ± 2.4	0.31 ± 0.05
SDSSJ135831.78+050522.8	A2	2.2 ± 0.3	68 ± 8	16.3 ± 2.0	0.65 ± 0.10
Q 1410+096	A2	3.0 ± 0.4	57 ± 7	13.7 ± 1.6	0.65 ± 0.13
B1422+231	A1	4.0 ± 0.5	78 ± 9	9.3 ± 1.1	0.22 ± 0.03
SDSSJ161458.33+144836.9	A2	2.3 ± 0.3	83 ± 9	16.8 ± 2.0	0.52 ± 0.08
PKS 1937−101	A1	7.6 ± 0.9	62 ± 7	13.5 ± 1.6	0.03 ± 0.01
PKS 2000−330	A2	2.8 ± 0.3	59 ± 7	15.1 ± 1.8	0.62 ± 0.09
SDSSJ210524.49+000407.3	A3	3.9 ± 0.5	31 ± 4	0.4 ± 3.0	1.00 ± 0.16
SDSSJ210831.56−063022.5	A3	1.4 ± 0.2	44 ± 6	4.7 ± 0.6	1.29 ± 0.19
SDSSJ212329.46−005052.9	A2	4.4 ± 0.5	34 ± 5	5.5 ± 0.7	0.96 ± 0.14
SDSSJ235808.54+012507.2	A2	4.7 ± 0.6	63 ± 8	10.7 ± 1.3	0.98 ± 0.20
		Population B			
HE 0001−2340	B1	1.6 ± 0.2	77 ± 9	10.6 ± 1.3	0.33 ± 0.05
[HB89] 0029+073	B1	2.4 ± 0.3	62 ± 7	7.8 ± 0.9	0.18 ± 0.02
CTQ 408	B1	6.9 ± 0.8	53 ± 6	2.5 ± 4.0	0.49 ± 0.07
H 0055−2659	B1	1.9 ± 0.2	92 ± 11	40.6 ± 4.9	0.29 ± 0.03
SDSSJ114358.52+052444.9	B2	1.1 ± 0.1	82 ± 10	5.4 ± 0.6	0.64 ± 0.10
SDSSJ115954.33+201921.1	B1	2.5 ± 0.3	78 ± 9	15.2 ± 1.8	0.04 ± 0.01
SDSSJ120147.90+120630.2	B1	4.3 ± 0.5	117 ± 14	21.0 ± 2.5	0.24 ± 0.04
SDSSJ141546.24+112943.4	B2	2.1 ± 0.3	108 ± 13	33.9 ± 4.1	0.71 ± 0.14
SDSSJ153830.55+085517.0	B1	1.1 ± 0.1	94 ± 11	5.5 ± 0.7	0.21 ± 0.03
PKS 2126−15	B1	4.8 ± 0.6	93 ± 11	10.0 ± 1.2	0.47 ± 0.09

Notes. [(a)]In units of 10^{-15} erg s^{-1} cm^{-2} Å^{-1}.

in the cases when the FWHM(Hβ) is at the border line of the A-B boundary. Orientation effects could be particularly important in the case of core-dominated RL sources, as the pole-on orientation may imply a narrowing of low-ionisation emission line widths (Wills & Browne 1986; Marziani et al. 2001; Sulentic et al. 2003; Rokaki et al. 2003; Zamfir et al. 2008; Bisogni et al. 2017).

There is just one case of a blatant disagreement between the classification deduced from the optical and UV spectra of the same source: SDSSJ153830.55+085517.0, which is optically classified as Pop. B but presents clearly Pop. A-like profiles in the UV spectrum (see Appendix A.14 and Fig. A.14). In this case, it was necessary to fit the optical as Pop. B and the UV as Pop. A.

5.2. Optical

5.2.1. Hβ

Appendix A shows the full VLT-ISAAC optical spectra and their respective Hβ+[O III]$\lambda\lambda$4959, 5007 fittings. Spectrophotometric measurements on Hβ are presented in Table 4. The ST of each source is listed in Col. 2; the specific continuum flux at 5100 Å (in rest-frame) is in Col. 3; equivalent width (EW) of the Hβ and [O III]$\lambda\lambda$4959,5007 full profiles in Cols. 4 and 5, respectively; and the Fe II prominence parameter ($R_{\mathrm{Fe\,II}}$) is listed in Col. 7.

Table 5 reports measurements on the Hβ profile. First we present the parameters obtained through the analysis of the Hβ full broad profile, including FWHM(Hβ_{full}), (Col. 2), asymmetry index (Col. 3), kurtosis (Col. 4), and the centroid velocity shifts at $\frac{1}{4}$, $\frac{1}{2}$, $\frac{3}{4}$, and $\frac{9}{10}$ fractional intensity (Cols. 5–8, respectively). In Col. 9, we list the full Hβ line flux (i.e., the flux for all broad line components, BC and VBC and BLUE, whenever appropriate). For each broad component isolated with the SPECFIT analysis we report, from Cols. 10–18, flux normalised by the total flux (I/I_{tot}), FWHM, and velocity shift. Then, Col. 19 shows the total flux of the narrow profile (SBC+NC) and from Cols. 20–25 we report I/I_{tot}, FWHM, and shift for these components. Additionally, we provide, in the last row of Pop. A and B, respectively, the median values of the measurements, together with the interquartile range.

The centroid velocities are close to the rest-frame wavelength for the majority of Pop. A and only two of the Pop. A quasars present $c(1/2)$ strongly shifted towards the blue with an averaged value of $\approx$−271 km s^{-1}. These sources are SDSSJ005700−18+14737.7 (ST A3) and SDSSJ132012.33+142037.1 (A1), both of them presenting a clear blueshifted contribution in Hβ profile. In the case of Pop. B quasars, the centroid velocities are significantly shifted towards the red wing of the profile in every fractional intensity for the majority of the sources, with an averaged $c(1/2)$ value of ~640 km s^{-1}. Even higher values are found for $c(1/4)$: Pop. B present an averaged value of $\approx$1780 km s^{-1} while Pop. A have $c(1/4) \approx -149$ km s^{-1}.

Overall, Pop. B sources show FWHM(Hβ_{full}) values that are much larger than those of Pop. A, usually ~6000 km s^{-1}. This difference is a direct consequence of the definition of Pop. A and B. The Pop. B asymmetry index is positive and very significantly different from 0, since the contribution of the VBC – that reaches FWHM values $\gtrsim$10 000 km s^{-1} – in all cases represents $\gtrsim$50% of the full emission line profile. In other words, differently from Pop. A sources (in which only a symmetric BC is enough to represent the full profile in the majority of the cases), a second redshifted component is always needed to reproduce the strong red wing of the observed Hβ profile.

Table 5. Results from SPECFIT analysis on Hβ.

	Hβ full broad profile							Full broad profile (BLUE+BC+VBC)										Narrow profile (SBC+NC)						
									BLUE[a]			BC			VBC				SBC			NC		
Source	$FWHM$ [km s^{-1}]	A.I.	Kurt.	$c(\frac{1}{4})$ [km s^{-1}]	$c(\frac{1}{2})$ [km s^{-1}]	$c(\frac{3}{4})$ [km s^{-1}]	$c(\frac{9}{10})$ [km s^{-1}]	I_{tot}[b]	I/I_{tot}	$FWHM$ [km s^{-1}]	Shift [km s^{-1}]	I/I_{tot}	$FWHM$ [km s^{-1}]	Shift [km s^{-1}]	I/I_{tot}	$FWHM$ [km s^{-1}]	Shift [km s^{-1}]	I_{tot}[c]	I/I_{tot}	$FWHM$ [km s^{-1}]	Shift [km s^{-1}]	I/I_{tot}	$FWHM$ [km s^{-1}]	Shift [km s^{-1}]
(1)	(2)	(3)	(4)	(5)	(6)	(7)	(8)	(9)	(10)	(11)	(12)	(13)	(14)	(15)	(16)	(17)	(18)	(19)	(20)	(21)	(22)	(23)	(24)	(25)
Population A																								
SDSSJ005700.18+143737.7	3830 ± 342	−0.09 ± 0.01	0.33 ± 0.01	−359 ± 237	−326 ± 83	−137 ± 107	−82 ± 118	1.66 ± 0.20	0.08 ± 0.03	2562 ± 359	−2154 ± 548	0.92 ± 0.06	3255 ± 346	0 ± 10	…	…	…	1.89 ± 0.23	0.00	…	…	1.00 ± 0.32	873 ± 93	0 ± 10
SDSSJ132012.33+142037.1	3450 ± 314	−0.11 ± 0.03	0.31 ± 0.01	−476 ± 323	−215 ± 72	−138 ± 93	−125 ± 110	0.91 ± 0.11	0.12 ± 0.05	7519 ± 1053	−1745 ± 584	0.88 ± 0.05	3224 ± 343	−41 ± 14	…	…	…	1.13 ± 0.14	0.00	…	…	1.00 ± 0.32	623 ± 66	−22 ± 17
SDSSJ135831.78+050522.8	3548 ± 314	0.00 ± 0.12	0.33 ± 0.01	−1 ± 297	0 ± 60	0 ± 97	0 ± 120	1.58 ± 0.19	0.00	…	…	0.92 ± 0.06	3548 ± 377	0 ± 10	…	…	…	1.49 ± 0.18	1.00 ± 0.32	5497 ± 770	−1712 ± 572	0.00	…	…
Q 1410+096	3394 ± 299	0.00 ± 0.08	0.33 ± 0.01	54 ± 279	54 ± 58	54 ± 92	54 ± 112	1.79 ± 0.21	0.00	…	…	1.00 ± 0.06	3394 ± 361	54 ± 58	…	…	…	0.37 ± 0.04	1.00 ± 0.32	4581 ± 320	−3144 ± 1051	0.00	…	…
B1422+231	5136 ± 452	0.00 ± 0.06	0.33 ± 0.01	−1 ± 422	−1 ± 89	0 ± 139	0 ± 169	3.20 ± 0.38	0.00	…	…	1.00 ± 0.06	5135 ± 546	0 ± 10	…	…	…	0.57 ± 0.07	0.00	…	…	1.00 ± 0.32	1113 ± 118	0 ± 10
SDSSJ161458.33+144836.9	3885 ± 349	−0.06 ± 0.11	0.33 ± 0.01	−241 ± 327	−98 ± 73	−51 ± 106	−38 ± 130	1.89 ± 0.21	0.09 ± 0.03	7224 ± 506	−1713 ± 571	0.91 ± 0.06	3721 ± 396	0 ± 10	…	…	…	0.54 ± 0.06	0.70 ± 0.25	2445 ± 170	−1709 ± 569	0.30 ± 0.09	439 ± 47	0 ± 10
PKS 1937−101	5298 ± 466	0.00 ± 0.07	0.33 ± 0.01	56 ± 434	56 ± 92	56 ± 144	56 ± 174	5.15 ± 0.62	0.00	…	…	1.00 ± 0.06	5296 ± 563	56 ± 92	…	…	…	1.57 ± 0.19	0.29 ± 0.09	2618 ± 183	−555 ± 183	0.71 ± 0.22	852 ± 91	−47 ± −77
PKS 2000−330	3230 ± 294	−0.06 ± 0.07	0.32 ± 0.01	−175 ± 306	−30 ± 61	1 ± 89	9 ± 108	1.92 ± 0.22	0.05 ± 0.01	5499 ± 385	−3127 ± 1031	0.95 ± 0.06	3138 ± 334	28 ± 54	…	…	…	2.31 ± 0.28	0.36 ± 0.11	1499 ± 105	−599 ± 197	0.63 ± 0.20	1082 ± 115	−46 ± −89
SDSSJ210524.49+000407.3	5026 ± 446	0.00 ± 0.06	0.33 ± 0.01	−1 ± 420	0 ± 85	0 ± 137	0 ± 169	1.28 ± 0.15	0.00	…	…	1.00 ± 0.6	5026 ± 534	0 ± 10	…	…	…	0.40 ± 0.05	0.00	…	…	1.00 ± 0.32	1407 ± 150	0 ± 10
SDSSJ210831.56−063022.5	4545 ± 200	0.00 ± 0.04	0.33 ± 0.01	93 ± 372	93 ± 79	93 ± 124	93 ± 149	0.60 ± 0.08	0.00	…	…	0.91 ± 0.06	4543 ± 483	93 ± 16	…	…	…	0.68 ± 0.08	0.89 ± 0.28	2597 ± 364	−2018 ± 347	0.11 ± 0.03	1403 ± 149	0 ± 10
SDSSJ212329.46−005052.9	4165 ± 366	0.00 ± 0.03	0.33 ± 0.01	−1 ± 342	−1 ± 72	0 ± 200	−1 ± 231	1.60 ± 0.22	0.00	…	…	0.89 ± 0.05	4164 ± 443	0 ± 10	…	…	…	2.40 ± 0.29	0.86 ± 0.27	4969 ± 696	−1844 ± 323	0.14 ± 0.04	1188 ± 126	0 ± 10
SDSSJ235808.54+012507.2	4098 ± 360	0.03 ± 0.06	0.35 ± 0.01	0 ± 336	0 ± 70	0 ± 111	−1 ± 136	2.88 ± 0.35	0.00	…	…	1.00 ± 0.06	4098 ± 436	0 ± 10	…	…	…	3.76 ± 0.45	0.38 ± 0.12	2463 ± 172	−1030 ± 340	0.61 ± 0.19	954 ± 101	0 ± 10
Median	3991 ± 1141	0.00 ± 0.06	0.33 ± 0.01	−1 ± 205	−0.5 ± 61	0 ± 27	0 ± 51	1.72 ± 0.65	0.08 ± 0.02	6362 ± 2533	−1949 ± 660	0.93 ± 0.09	3909 ± 1305	0 ± 34	…	…	…	1.31 ± 1.43	0.78 ± 0.54	2607 ± 2219	−1710 ± 965	0.67 ± 0.62	1018 ± 312	0 ± 16
Population B																								
HE 0001−2340	6632 ± 1065	0.16 ± 0.22	0.37 ± 0.01	1757 ± 873	1134 ± 153	960 ± 354	909 ± 471	1.30 ± 0.16	0.00	…	…	0.42 ± 0.06	5063 ± 366	681 ± 92	0.58 ± 0.06	10982 ± 1955	2538 ± 342	0.33 ± 0.04	0.34 ± 0.11	3772 ± 264	−414 ± 136	0.65 ± 0.21	1067 ± 77	0 ± 10[d]
[HB89] 0029+073	6347 ± 1085	0.18 ± 0.05	0.37 ± 0.01	932 ± 757	292 ± 138	51 ± 339	−19 ± 442	1.54 ± 0.18	0.07 ± 0.01	4995 ± 837	−1216 ± 575	0.33 ± 0.05	4508 ± 326	−310 ± 147	0.60 ± 0.06	9609 ± 1710	1430 ± 193	1.54 ± 0.18	0.00	…	…	1.00 ± 0.32	1024 ± 74	0 ± 10
CTQ 408	7301 ± 1081	0.10 ± 0.09	0.40 ± 0.02	724 ± 910	306 ± 179	197 ± 390	164 ± 528	3.90 ± 0.47	0.00	…	…	0.52 ± 0.08	6050 ± 437	0 ± 10	0.48 ± 0.05	13243 ± 2357	1963 ± 264	2.54 ± 0.30	0.00	…	…	1.00 ± 0.32	1500 ± 108	0 ± 10
H 0055−2659	5342 ± 925	0.36 ± 0.13	0.30 ± 0.03	2249 ± 1085	580 ± 101	380 ± 283	329 ± 377	1.85 ± 0.22	0.00	…	…	0.27 ± 0.04	4609 ± 333	−224 ± 39	0.73 ± 0.07	13355 ± 2377	2527 ± 340	0.82 ± 0.10	0.00	…	…	1.00 ± 0.32	1500 ± 108	0 ± 10
SDSSJ114358.52+052444.9	5999 ± 942	0.24 ± 0.15	0.34 ± 0.05	1485 ± 1408	354 ± 133	210 ± 319	170 ± 431	1.00 ± 0.12	0.00	…	…	0.52 ± 0.08	5007 ± 362	0 ± 10	0.48 ± 0.05	13341 ± 2375	4095 ± 552	0.34 ± 0.04	0.47 ± 0.15	1830 ± 128	−1277 ± 421	0.53 ± 0.17	1304 ± 94	0 ± 10[d]
SDSSJ115954.33+201921.1	8006 ± 1659	0.29 ± 0.10	0.33 ± 0.01	2389 ± 1025	950 ± 133	469 ± 422	359 ± 536	2.05 ± 0.25	0.00	…	…	0.36 ± 0.05	5458 ± 395	−35 ± 15	0.64 ± 0.06	12924 ± 2300	3287 ± 443	0.42 ± 0.05	0.72 ± 0.23	2660 ± 186	−1215 ± 401	0.27 ± 0.08	995 ± 72	−101 ± 14
SDSSJ120147.90+120630.2	7995 ± 1748	0.28 ± 0.11	0.33 ± 0.01	2331 ± 947	1124 ± 140	540 ± 421	414 ± 519	4.31 ± 0.52	0.00	…	…	0.30 ± 0.0	4986 ± 360	9 ± 10	0.70 ± 0.07	12190 ± 2170	2850 ± 384	6.33 ± 0.76	0.05 ± 0.01	1879 ± 131	−246 ± 81	0.95 ± 0.30	1879 ± 136	−1 ± 10
SDSSJ141546.24+112943.4	7253 ± 1237	0.23 ± 0.11	0.36 ± 0.02	1769 ± 952	736 ± 145	447 ± 387	367 ± 510	1.59 ± 0.19	0.00	…	…	0.45 ± 0.07	5544 ± 401	14 ± 13	0.55 ± 0.05	11523 ± 2051	3144 ± 423	1.31 ± 0.16	0.29 ± 0.09	1000 ± 70	−784 ± 258	0.71 ± 0.22	1162 ± 84	14 ± 13
SDSSJ153830.55+085517.0	7816 ± 1354	0.25 ± 0.11	0.35 ± 0.02	2090 ± 1081	800 ± 152	478 ± 415	390 ± 548	1.16 ± 0.14	0.00	…	…	0.47 ± 0.07	6038 ± 437	9 ± 12	0.53 ± 0.05	12642 ± 2250	3869 ± 521	0.50 ± 0.06	0.00	…	…	1.00 ± 0.32	1000 ± 72	−1 ± 10
PKS 2126−15[e]	5018 ± 648	0.50 ± 0.09	0.22 ± 0.01	2104 ± 414	81 ± 51	−303 ± 168	−713 ± 90	4.28 ± 0.51	0.09 ± 0.02	4662 ± 781	−4717 ± 2970	0.35 ± 0.05	4074 ± 295	−589 ± 371	0.56 ± 0.05	9992 ± 1779	3585 ± 483	3.34 ± 0.40	0.17 ± 0.05	1345 ± 94	−426 ± 140	0.83 ± 0.26	922 ± 67	0 ± 10
Median	6942 ± 1601	0.24 ± 0.09	0.34 ± 0.03	1929 ± 659	658 ± 594	413 ± 275	344 ± 218	1.72 ± 2.07	0.08 ± 0.01	4828 ± 166	−2966 ± 1750	0.39 ± 0.13	5035 ± 819	0 ± 186	0.57 ± 0.09	12416 ± 2046	2997 ± 980	1.06 ± 1.85	0.31 ± 0.23	1854 ± 998	−605 ± 690	0.89 ± 0.33	1114 ± 445	0 ± 1

Notes. [a]In these columns, we report additional blueshifted components that were included in the Hβ profile. [b]In units of 10^{-13} erg s^{-1} cm^{-2}. [c]In units of 10^{-14} erg s^{-1} cm^{-2}. [d]There is an additional contribution due to small blueshifted components associated with narrow line emission. [e]Full profile centroid velocities and the presence of a BLUE Hβ component in this case are affected by the location of the continuum.

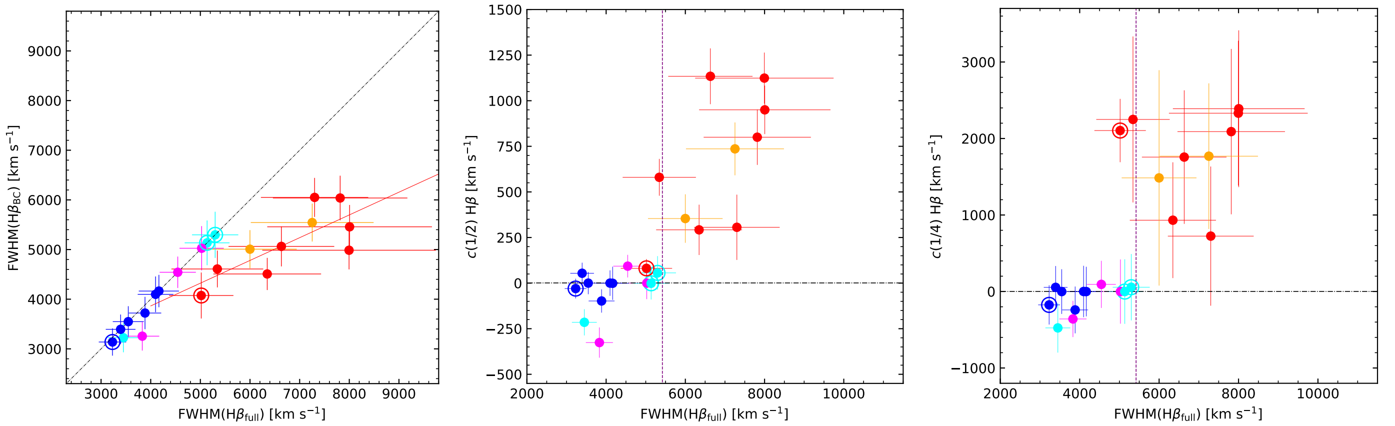

Fig. 4. Comparison between the different properties of the Hβ emission line profile. *Left panel*: FWHM(H$\beta_{\rm BC}$) vs. FWHM of the full Hβ profile. *Central panel*: velocity centroid at 1/2 intensity $c(1/2)$ vs. FWHM(H$\beta_{\rm full}$). *Right panel*: velocity centroid at 1/4 flux intensity $c(1/4)$ vs. FWHM(H$\beta_{\rm full}$). Symbols surrounded by open circles show the radio-loud sources and filled circles represent the radio-quiet from the sample. Red line represent the linear regression performed for Pop. B. Horizontal dashed lines in the *central* and *right panels* indicate $c(1/4) = 0$ and $c(1/2) = 0$ for Hβ, respectively. Purple vertical dashed lines shows the boundary between Pop. A and Pop. B. The many MS spectral type (ST) are represented in different colours: A1 (•); A2 (•); A3 (•); B1 (•); and B2 (•).

Semi-broad Hβ blueshifts could be mainly associated with the [O III]$\lambda\lambda$4959,5007 SBC. However, in some cases, an additional BLUE Hβ component is needed (see Table 5). In particular, PKS 2126−15 presents a huge BLUE blueshift of ≈ -4700 km s^{-1}, associated with a boxy termination of the Hβ blue wing. A second peculiarity of this source is that the Hβ BC is significantly shifted to the blue, down to half maximum, which is at variance with all other Pop. B sources.

The Hβ NC is weak especially in Pop. A ($\lesssim$0.02 of the Hβ line flux), although it is observed in all cases save two Pop. A2 sources (SDSSJ132012.33+142037.1 and Q 1410+096). In Pop. B, the narrow component is somewhat stronger but always $\lesssim$0.05 of the line flux. Given its weakness, the NC is therefore not significantly affecting the flux of any broad component measured in this paper.

Relation between FWHM(H$\beta_{\rm full}$) and FWHM(H$\beta_{\rm BC}$). This work confirms previous studies (e.g. Sulentic et al. 2006a; Marziani et al. 2009, and references therein) that showed that the full Hβ profile of Pop. A can be accounted for mostly by the BC, and that a redshifted VBC seems to be absent in Pop. A but present in Pop. B sources: Table 5 lists centroid and asymmetry index values for Pop. B sources of $1000 \lesssim c(\frac{1}{4}) \lesssim 2000$ km s^{-1} and $\approx$0.2, respectively. For Pop. A these values are $\lesssim$0 km s^{-1} and 0.

The left plot of Fig. 4 shows the relation between the FWHM of the BC and the FWHM of the full profile of Hβ for the two populations. Pop. A and Pop. B sources follow different trends for the ratio ξ(Hβ) = $FWHM$(H$\beta_{\rm BC}$)/$FWHM$(H$\beta_{\rm full}$). For Pop. A quasars, we obtain ξ(Hβ) = 1.00 for all sources but four (SDSSJ005700.18+143737.7, SDSSJ132012.33+142037.1, SDSSJ161458.33+144836.9, and PKS 2000−330, with ξ(Hβ) $\approx$ 0.9 due to the presence of a blueshifted component). The ξ(Hβ) ratio for Pop. B is only $\approx$0.76, indicating that the Pop. B Hβ full profile is less representative of the BC than the Pop. A sources. Similar results were also shown by Marziani et al. (2013): they obtain ξ(Hβ) = 1.00 for Pop. A and $\sim$0.78 for Pop. B quasars. In our sample Pop. B sources usually present a very strong and wide VBC component that accounts for $\approx$0.57 of the profile, with a mean FWHM of 11 240 km s^{-1}. Meanwhile, as mentioned, the Pop. A sources in general are well represented by only a BC. This also seems to be true for the radio-loud Pop. A sources from the sample.

Clear distinctions between Pop. A and Pop. B are also seen in the center and left panels of Fig. 4, which present the $c(1/2)$ and $c(1/4)$ vs. FWHM(H$\beta_{\rm full}$) relations, respectively. Pop. A sources show in general no shift, within the uncertainties, or a negative value of velocity centroids in the case of the 4 sources with a BLUE component (with average centroid values at 1/2 and 1/4 of −167 and −312 km s^{-1}, respectively). On the other hand, Pop. B sources always present positive velocities for $c(1/2)$ and $c(1/4)$, with a mean value of 658 and 1929 km s^{-1}, respectively, as a consequence of a very strong VBC. The VBC individually has a median velocity shift of $\sim$3000 km s^{-1}, in a range from −1500 to 4000 km s^{-1}. These results are in complete agreement with previous results (e.g. Wolf et al. 2020, and references therein).

5.2.2. [O III]$\lambda\lambda$4959, 5007

High-ionisation lines like [O III]$\lambda\lambda$4959,5007 are seen as one of the main detectors of outflowing gas in radio-quiet sources (Zamanov et al. 2002; Komossa et al. 2008; Zhang et al. 2011; Marziani et al. 2016a). In the case of radio-loud sources, narrow-line outflowing gas has been associated with jets through the blueshifted line components (Capetti et al. 1996; Axon et al. 2000; Bicknell 2002; Kauffmann et al. 2008; Best & Heckman 2012; Reynaldi & Feinstein 2013; Jarvis et al. 2019; Berton & Järvelä 2021). Outflows are also detected in Hβ. Usually, the blueshifted components on the Hβ profile are related to those found for the [O III]$\lambda\lambda$4959,5007 lines (Carniani et al. 2015; Cresci et al. 2015; Brusa et al. 2015; Marziani et al. 2022a). The results obtained for [O III]λ5007 full profile and individual components are reported in Table 6. We present FWHM (Col. 2), asymmetry (Col. 3), kurtosis (Col. 4), and the centroid velocities at 1/2 and 9/10 intensities (Cols. 5 and 6, respectively) for the full profile. Relative intensities, FWHM, and shifts are reported for the [O III]λ5007 blueshifted components (Cols. 7–9) and for the narrow components (Cols. 10–12) of each quasar. It is difficult to distinguish the relative contribution of the two components in the majority of the cases. One of the main reasons for this is that in many sources the full [O III]λ5007 emission is shifted to the

Table 6. Measurements on the [O III]λ5007 full line profile.

Source	[O III]λ5007 full profile					SBC			NC		
	FWHM [km s^{-1}]	A.I.	Kurtosis	$c(1/2)$ [km s^{-1}]	$c(9/10)$ [km s^{-1}]	I/I_{tot}	*FWHM* [km s^{-1}]	Shift [km s^{-1}]	I/I_{tot}	*FWHM* [km s^{-1}]	Shift [km s^{-1}]
(1)	(2)	(3)	(4)	(5)	(6)	(7)	(8)	(9)	(10)	(11)	(12)
Population A											
SDSSJ005700.18+143737.7 [(a)]	764::	−0.01::	0.45::	−89::	−88::	0.27::	1214::	−1856::	0.732::	761::	−87::
SDSSJ132012.33+142037.1	2124 ± 147	−0.54 ± 0.01	0.23 ± 0.01	−770 ± 62	−221 ± 36	0.64 ± 0.06	2275 ± 235	−1429 ± 115	0.357 ± 0.114	895 ± 95	−149 ± 22
SDSSJ135831.78+050522.8	4320 ± 297	−0.43 ± 0.05	0.19 ± 0.10	−1895 ± 91	−630 ± 59	0.90 ± 0.08	5422 ± 561	−2080 ± 100	0.096 ± 0.031	1000 ± 106	−534 ± 80
Q 1410+096	3363 ± 283	−0.52 ± 0.01	0.28 ± 0.01	−1404 ± 107	−656 ± 72	0.73 ± 0.07	5573 ± 577	−1255 ± 96	0.267 ± 0.085	1379 ± 147	−260 ± 39
B1422+231	1535 ± 99	−0.18 ± 0.01	0.43 ± 0.01	−217 ± 26	−88 ± 47	0.32 ± 0.03	1128 ± 117	−850 ± 102	0.680 ± 0.218	1117 ± 119	27 ± 4
SDSSJ161458.33+144836.9	2616 ± 160	−0.49 ± 0.01	0.28 ± 0.02	−1452 ± 54	−800 ± 50	0.75 ± 0.07	2759 ± 286	−1875 ± 70	0.245 ± 0.078	1006 ± 107	−667 ± 100
PKS 1937−101	1046 ± 79	−0.15 ± 0.09	0.35 ± 0.02	−155 ± 17	−135 ± 31	0.57 ± 0.05	2657 ± 275	−484 ± 53	0.432 ± 0.138	832 ± 88	−120 ± 18
PKS 2000−330	1314 ± 89	−0.13 ± 0.01	0.42 ± 0.01	−425 ± 22	−371 ± 41	0.42 ± 0.04	1500 ± 155	−827 ± 43	0.578 ± 0.185	1082 ± 115	−263 ± 39
SDSSJ210524.49+000407.3	1365::	0.00::	0.45::	201::	202::	1.00::	1361::	203::	0.000	…	…
SDSSJ210831.56−063022.5	3665::	0.00::	0.46::	−1243::	−1242::	1.00::	3679::	−1244::	0.000	…	…
SDSSJ212329.46−005052.9	3656 ± 247	−0.04 ± 0.04	0.39 ± 0.02	−2885 ± 58	−2584 ± 119	0.88 ± 0.08	4719 ± 488	−2376 ± 48	0.115::	2043::	174::
SDSSJ235808.54+012507.2	1870 ± 224	0.00 ± 0.03	0.46 ± 0.01	−943 ± 78	−942 ± 49	1.00 ± 0.09	2464 ± 255	−1053 ± 87	0.000	…	…
Median	1997 ± 2045	−0.14 ± 0.42	0.40 ± 0.17	−856 ± 1214	−500 ± 707	0.68 ± 0.49	2560 ± 2032	−1249 ± 1016	0.312 ± 0.493	1082 ± 427	−120 ± 288
Population B											
HE 0001−2340	1029 ± 145	−0.07 ± 0.10	0.40 ± 0.02	−24 ± 30	−12 ± 64	0.43 ± 0.03	2768 ± 90	−443 ± 554	0.565 ± 0.202	894 ± 65	−1 ± 10
[HB89] 0029+073	1866 ± 271	−0.47 ± 0.01	0.38 ± 0.01	−922 ± 97	−562 ± 114	1.00 ± 0.06	3431 ± 168	−397 ± 42	0.000	…	…
CTQ 408	1497 ± 190	0.00 ± 0.01	0.46 ± 0.01	−524 ± 37	−524 ± 97	1.00 ± 0.09	1500 ± 401	−524 ± 37	0.000	…	…
H 0055−2659	1405 ± 325	−0.47 ± 0.06	0.25 ± 0.01	−198 ± 103	−91 ± 81	0.50 ± 0.07	3204 ± 412	−599 ± 312	0.496 ± 0.177	912 ± 66	69 ± 10
SDSSJ114358.52+052444.9	2577 ± 251	0.05 ± 0.03	0.54 ± 0.02	−968 ± 52	−1079 ± 186	0.78 ± 0.03	1982 ± 83	−1295 ± 70	0.220 ± 0.078	1304 ± 94	−1 ± 10
SDSSJ115954.33+201921.1	1233 ± 186	−0.20 ± 0.10	0.37 ± 0.03	−347 ± 46	−302 ± 76	0.55 ± 0.07	2684 ± 204	−499 ± 66	0.448 ± 0.160	995 ± 72	−261 ± 39
SDSSJ120147.90+120630.2	2584 ± 200	−0.10 ± 0.01	0.61 ± 0.01	−594 ± 49	−504 ± 126	0.72 ± 0.05	1879 ± 196	−978 ± 81	0.280 ± 0.100	1129 ± 82	244 ± 37
SDSSJ141546.24+112943.4	1193 ± 204	−0.37 ± 0.01	0.38 ± 0.01	−116 ± 70	55 ± 75	0.47 ± 0.04	1499 ± 111	−415 ± 250	0.526 ± 0.188	700 ± 51	151 ± 23
SDSSJ153830.55+085517.0	1520 ± 192	0.00 ± 0.01	0.46 ± 0.01	−545 ± 38	−545 ± 97	1.00 ± 0.09	1523 ± 101	−545 ± 38	0.000	…	…
PKS 2126−15	1212 ± 167	−0.22 ± 0.03	0.41 ± 0.01	−441 ± 44	−355 ± 75	0.30 ± 0.09	1332 ± 272	−988 ± 99	0.702 ± 0.250	937 ± 68	−285 ± 43
Median	1451 ± 562	−0.15 ± 0.31	0.40 ± 0.08	−482 ± 346	−429 ± 396	0.52 ± 0.32	1930 ± 1241	−534 ± 426	0.364 ± 0.463	937 ± 159	−1 ± 241

Notes. [(a)] [O III]λ5007 location is not clear for this source since it is placed at the red end of the observed spectrum. In this case, the measurements were performed with [O III]λ4959.

blue, implying a shift of [O III]λ5007 NC with respect to the rest-frame. Some sources like SDSSJ135831.78+050522.8 and SDSSJ161458.33+144836.9 present a NC strongly shifted to the blue, reaching shifts of ≈ -530 and -670 km s^{-1} respectively, comparable to the shifts found for the semi-broad component (see e.g. Figs. A.10 and A.15).This is consistent with outflowing gas dominating the [O III]λ5007 luminosity in luminous quasars (Shen & Ho 2014; Bischetti et al. 2017; Zakamska et al. 2016).

The remarkable feature of the [O III]$\lambda\lambda$4959,5007 profiles is a very intense and blueshifted SBC, such as the one of SDSSJ135831.78+050522.8 (Fig. A.10), which presents a blueshifted SBC that accounts for the full [O III]λ5007 profile with a $FWHM \approx 5422$ km s^{-1} and a shift of ≈ -2080 km s^{-1}. In this case, the blueshifted SBC corresponds to 90% of the full profile and can be interpreted as a strong indicative of outflowing gas. SDSSJ135831.78+050522.8, along with Q 1410+096 (Fig. A.11), which shows a very similar profile, requires a strong and broad [O III]λ5007 to account for the flux on the red side of Hβ. In our high luminosity sample, for 15/22 objects (~70%) the blueshifted SBC accounts for more than 50% of the total intensity of the [O III] profile. In fact, in six of these sources, the [O III] consists of exclusively a blueshifted SBC.

Very small blueshifted components are found in low-redshift [O III]$\lambda\lambda$4959,5007 profiles of Pop. B AGN (Zamfir et al. 2008; Sulentic et al. 2004) and even in Population A, shifts at peak above 250 km s^{-1} are very rare (the so-called 'blue-outliers'; Zamanov et al. 2002). At high-redshift, Pop. B [O III]$\lambda\lambda$4959,5007 profiles do present significant blueshifted SBC components but they still present different properties when compared to Pop. A sources: in our sample, the full profiles of Pop. A present a [O III] $FWHM \approx 2000$ km s^{-1} while Pop. B profiles have $FWHM \approx 1450$ km s^{-1}. The more remarkable difference is seen in the shifts at 9/10 and 1/2 intensities of the full profile ($c(1/2) \approx -850$ km s^{-1} for Pop. A and ≈ -480 km s^{-1} for Pop. B). However, the A.I. of the two populations are almost the same, indicating that the lines present similar profile shapes. The [O III]$\lambda\lambda$4959,5007 emission of both Pop. A and Pop. B appears to be strongly affected (if not dominated) by outflowing gas.

An important consequence for redshift estimates is that the [O III]$\lambda\lambda$4959,5007 lines should be avoided when considering high-z quasars. In addition, three Pop. A (SDSSJ210524.49+000407.3, SDSSJ210831.56−063022.5, and SDSSJ235808.54+012507.2) and three Pop. B sources ([HB89] 0029+073, CTQ 0408, and SDSSJ153830.55+085517.0) present [O III]λ5007 full profiles that can be well represented only by the blueshifted component (see the respective spectra in Figs. A.22, A.2, A.3, and A.14).

Figure 5 shows the relation between W([O III]) and $|c(9/10)|$ of [O III]λ5007. For our sample, the W([O III]) ranges from ≈50 Å for some Pop. B sources to <1 Å for xAs, reaching the detection limit. It shares the same location as the high-redshift HE data. No clear difference between the location of Pop. A and Pop. B is confirmed by the median values of equivalent widths, 12 Å vs 10 Å for Pop. A and B, respectively (the average W is affected by the two A3 extremely faint sources with W([O III]) $\lesssim 1$ Å). At low z (and low luminosity), sources have considerably larger W values but lower velocity centroids than the high-z sample. Our sample is located at the low end of the W([O III]) distribution of low-z sources as expected for luminous quasars (Shen & Ho 2014), and in a shift range that at low z is the exclusive domain of the rare, namesake 'blue outliers' (Marziani et al. 2016b). Figure 5 also shows that the radio-loud quasars from our sample are very tightly grouped together with moderate blueshifts for high-L quasars ($\lesssim$500 km s^{-1} at 0.9 fractional intensity).

A comparison between $c(1/2)$ and FWHM of the [O III]λ5007 profiles is shown in Fig. 6. There is a strong

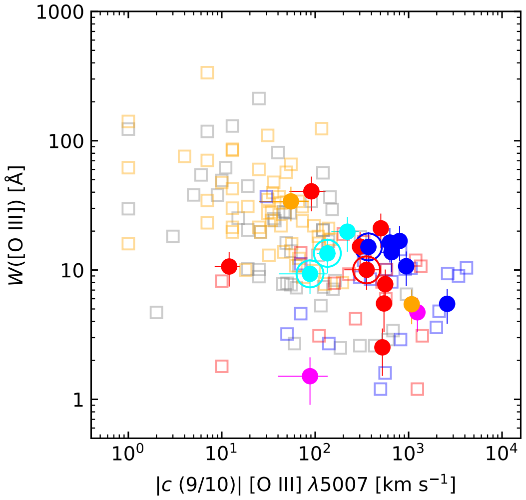

Fig. 5. W([O III]λ5007) versus c(9/10). Blue and red squares indicate high-redshift Pop. A and Pop. B quasars from M09 while grey and orange open squares represent low-z sources from Marziani et al. (2003), respectively. Colour scheme for our sample as the same as in Fig. 4. Error bars refer to 1σ level of confidence and were estimated only for our sample.

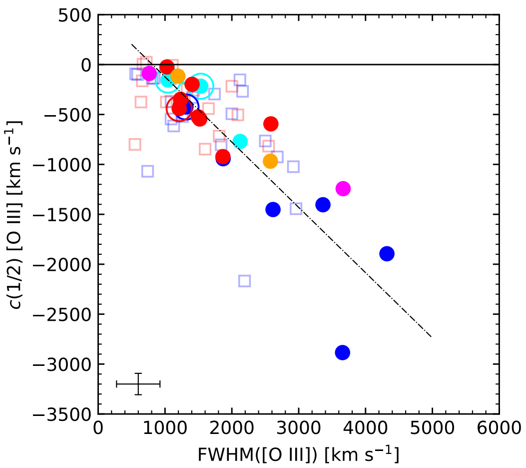

Fig. 6. FWHM of the full profile of [O III]$\lambda\lambda$4959,5007 versus centroid at 1/2 flux intensity (c(1/2)) for the [O III]$\lambda\lambda$4959,5007 emission line. Blue and red squares indicate high-redshift sources from M09. Dashed line represents a linear regression. Colour scheme is the same as in Fig. 4. Error bars refer to 1σ level of confidence and were estimated only for our sample.

correlation between the blueshift of [O III], parameterised by the centroid at 1/2 intensity, and the FWHM. The dashed line in the plot traces the linear regression between both parameters, derived from an unweighted least squares fit:

$$c(1/2)_{[\mathrm{O\,III}]} \approx (-0.65 \pm 0.08) FWHM([\mathrm{O\,III}]) + (530 \pm 205). \quad (1)$$

Table 7 lists this linear relation, along with the other that relates to C IVλ1549. We report the fitted parameters (Cols. 1 and 2), the method used (Col. 3), the linear correlation coefficients (Cols. 4 and 5), the rms (Col. 6), the Pearson r score (Col. 7), and its associated null hypothesis probability value (Col. 8). Equation (1) confirms several previous works (Komossa et al. 2008; Marziani et al. 2016a) and justifies the interpretation of the [O III]λ5007 profile in terms of a blueshifted semibroad component and of a narrow component (Zhang et al. 2011).

5.3. UV

The fits for the UV emission lines are shown in Appendix A, along with the full UV spectra of the 15 available sources (10 Pop. A and 5 Pop. B). Spectrophotometric measurements in the UV region are reported in Table 8 and concern the 1900 Å blend, C IVλ1549+He IIλ1640, as well as flux intensity and equivalent width of Si IV+O IV (Cols. 3–4), C IV (Cols. 5–6), He II (Cols. 7–8), Al III (Cols. 9–10), C III] (Cols. 11–12), and Si III (Cols. 13–14).

5.3.1. 1900 Å blend

Table 9 presents the measurements resulting from the `specfit` analysis of the 1900 Å blend. Intensities, FWHM, and shifts are shown for the emission line profiles and their components, whenever the profile presents more than just one component. In Cols. 2–4, we list the relative intensity, FWHM, and shift of the blueshifted component of Al IIIλ1860; Cols. 5–7 show the broad component of Al IIIλ1860; Cols. 8–10 for Si III]λ1892 BLUE; Cols. 11–13 for Si III]λ1892 BC; Cols. 14–16, the BC of C III]λ1909; Cols. 17–19, the VBC of C III]λ1909; Cols. 20–22, the NC of C III]λ1909; and, finally, Cols. 23–25 for a Fe III]λ1914 emission line component.

The Al IIIλ1860 contribution can be well fitted assuming only a BC for all Pop. A sources but four: SDSSJ005700.18+143737.7, SDSSJ210524.49+000407.3, SDSSJ210831.56−063022.5, and SDSSJ132012.33+142037.1. These same three sources are the ones that are located in the A3 region of the quasar MS. In these cases, we need to add a BLUE component with $3000 \leq FWHM \leq 4500$ km s^{-1} in the Al IIIλ1860 doublet and in the Si III]λ1892 emission line profile. We have imposed the same FWHM for both components.

The Pop. A C III]λ1909 profile can be well reproduced by a strong BC at rest-frame in combination with a component that accounts for the Fe IIIλ1914 contributions in its red wing. The motivation to include the Fe IIIλ1914 line resides in the selective enhancement due to Lyman α fluorescence that is well-known to affect the UV Fe II emission and Fe III emission as well (Sigut & Pradhan 1998; Sigut et al. 2004). Of the Fe II features the UV multiplet 191 at λ1785 is known to be enhanced by Lyα fluorescence: a strong Fe II UV multiplet 191 may suggest a strong Fe IIIλ1914 line. There is an overall consistency between the presence of the Fe IIIλ1914 line and the detection of the Fe II feature (8 out of 10 Pop. A sources with UV suitable data have both). However, the relative contribution of the C III]λ1909 and Fe IIIλ1914 remains difficult to ascertain because the two lines are severely blended together and some Fe IIIλ1914 emission is already included in the Fe III template.

For Pop. B sources, Al IIIλ1860 and Si III]λ1892 are well represented by only one component and in the five cases these emission lines share the same FWHM and are centred at the respective rest-frame wavelength. However, the C III]λ1909 VBC is systematically less broad than the Hβ VBC: average FWHM is ≈7000 km s^{-1} for C III] versus ≈12 000 km s^{-1} for Hβ.

5.3.2. C IVλ1549+He IIλ1640

Measurements related to the C IVλ1549+He IIλ1640 blend are reported in Table 10. As for Hβ, we list FWHM (Col. 2), A.I. (Col. 3), kurtosis (Col. 4), and centroids c(1/4), c(1/2), c(3/4) and c(9/10) in Cols. 5–8 for the C IVλ1549 full line profile. Information on individual components is also given for both C IVλ1549 and He IIλ1640. Columns 9–11 give the

Table 7. Linear relations ($y = a + b * x$) between different emission line properties.

y (1)	x (2)	Method (3)	$a \pm \delta a$ (4)	$b \pm \delta b$ (5)	RMSE (6)	CC (7)	ρ-value (8)
$c(1/2)_{\mathrm{[O\,III]}}$	$FWHM$([O III])	Least squares	530 ± 205	−0.65 ± 0.08	402	−0.86	4.1×10^{-7}
$c(1/2)_{\mathrm{C\,IV}}$	$FWHM$(C IV)	Least squares	2000 ± 737 [(a)]	−0.68 ± 0.10 [(a)]	429	−0.90 [(a)]	1.1×10^{-4} [(a)]
log W(C IV)	log $\lvert c(1/2)\rvert_{\mathrm{C\,IV}}$	Bisector	3.21 ± 0.17 [(a)]	−0.58 ± 0.05 [(a)]	0.28	−0.64 [(a)]	2.1×10^{-12} [(a)]
log W(C IV)	log $FWHM$(C IV)	Bisector	8.31 ± 0.71 [(a)]	−1.84 ± 0.19 [(a)]	0.31	−0.49 [(a)]	2.5×10^{-7} [(a)]
$c(1/2)_{\mathrm{C\,IV}}$	$c(1/2)_{\mathrm{[O\,III]}}$	Orthogonal	−1239 ± 276	1.50 ± 0.31	1086	0.45	4×10^{-3}

Notes. [(a)]Only for Pop. A.

Table 8. Spectrophotometric measurements on the UV region.

Source (1)	$f_{\lambda,1750}$ [(a)] (2)	f(Si IV+O IV) [(b)] (3)	W(Si IV+O IV) [Å] (4)	f(C IV) [(b)] (5)	W(C IV) [Å] (6)	f(He II) [(b)] (7)	W(He II) [Å] (8)	f(Al III) [(b)] (9)	W(Al III) [Å] (10)	f(C III]) [(b)] (11)	W(C III]) [Å] (12)	f(Si III]) [(b)] (13)	W(Si III]) [Å] (14)
Population A													
SDSSJ005700.18+143737.7 [(e)]	5.9 ± 0.9	1.29 ± 0.19	16 ± 2	1.58 ± 0.24	22 ± 3	0.33 ± 0.05	5 ± 1	0.41 ± 0.06	8 ± 1	0.23 ± 0.03	5 ± 1	0.42 ± 0.06	8 ± 1
SDSSJ132012.33+142037.1	7.9 ± 1.2	1.77 ± 0.27	18 ± 2	3.66 ± 0.55	40 ± 5	0.81 ± 0.12	10 ± 1	0.31 ± 0.05	4 ± 1	0.57 ± 0.09	8 ± 1	0.75 ± 0.11	11 ± 1
SDSSJ135831.78+050522.8	13.6 ± 2.0	3.78 ± 0.57	20 ± 2	5.43 ± 0.81	34 ± 4	1.31 ± 0.20	9 ± 1	0.89 ± 0.13	7 ± 1	1.01 ± 0.15	9 ± 1	1.52 ± 0.23	13 ± 2
Q 1410+096	14.1 ± 2.1	2.45 ± 0.37	15 ± 2	3.50 ± 0.53	23 ± 3	1.50 ± 0.23	10 ± 1	0.96 ± 0.14	7 ± 1	1.17 ± 0.18	9 ± 1	1.18 ± 0.18	9 ± 1
SDSSJ161458.33+144836.9	15.4 ± 2.3	2.90 ± 0.44	14 ± 2	5.74 ± 0.86	31 ± 4	0.94 ± 0.14	6 ± 1	0.57 ± 0.09	4 ± 1	1.41 ± 0.21	11 ± 1	1.32 ± 0.20	10 ± 1
PKS 2000−330 [(c)]	–	3.20 ± 0.48	4 ± 2	4.50 ± 0.68	19 ± 2	–	–	–	–	–	–	–	–
SDSSJ210524.47+000407.3 [(d),(e)]	21.8 ± 3.3	–	–	1.50 ± 0.23	6 ± 1	0.75 ± 0.11	3 ± 1	2.19 ± 0.33	10 ± 1	0.51 ± 0.08	2 ± 1	1.97 ± 0.30	9 ± 1
SDSSJ210831.56−063022.5 [(e)]	14.3 ± 2.1	2.47 ± 0.37	14 ± 2	2.25 ± 0.34	13 ± 2	0.14 ± 0.02	1 ± 1	1.01 ± 0.15	7 ± 1	0.31 ± 0.05	2 ± 1	0.94 ± 0.14	7 ± 1
SDSSJ212329.46−005052.9	23.9 ± 3.6	3.58 ± 0.54	9 ± 1	6.09 ± 0.91	19 ± 2	0.85 ± 0.13	3 ± 1	1.77 ± 0.27	9 ± 1	0.59 ± 0.09	3 ± 1	1.89 ± 0.28	10 ± 1
SDSSJ235808.54+012507.2	7.5 ± 1.1	1.52 ± 0.23	12 ± 1	2.55 ± 0.38	25 ± 3	0.71 ± 0.11	8 ± 1	1.91 ± 0.29	5 ± 1	0.47 ± 0.07	8 ± 1	0.61 ± 0.09	10 ± 1
Population B													
SDSSJ114358.52+052444.9	20.2 ± 3.0	2.28 ± 0.34	8 ± 1	5.86 ± 0.88	24 ± 3	1.42 ± 0.21	6 ± 1	0.71 ± 0.11	4 ± 1	1.30 ± 0.20	7 ± 1	0.98 ± 0.15	5 ± 1
SDSSJ115954.33+201921.1	24.3 ± 3.6	3.64 ± 0.55	12 ± 1	5.55 ± 0.83	20 ± 2	0.92 ± 0.14	4 ± 1	1.14 ± 0.17	5 ± 1	1.94 ± 0.29	9 ± 1	0.62 ± 0.09	3 ± 1
SDSSJ120147.90+120630.2	16.3 ± 2.4	3.44 ± 0.52	15 ± 2	7.57 ± 1.14	37 ± 4	1.63 ± 0.24	9 ± 1	0.67 ± 0.10	5 ± 1	3.00 ± 0.45	22 ± 3	1.13 ± 0.17	8 ± 1
SDSSJ141546.24+112943.4 [(d)]	16.8 ± 2.5	–	–	–	–	–	–	1.59 ± 0.24	7 ± 1	5.10 ± 0.77	23 ± 3	2.83 ± 0.42	13 ± 2
SDSSJ153830.55+085517.0 [(f)]	17.4 ± 2.6	4.92 ± 0.74	19 ± 2	5.34 ± 0.80	24 ± 3	0.64 ± 0.10	3 ± 1	1.91 ± 0.29	12 ± 1	0.94 ± 0.14	6 ± 1	1.27 ± 0.19	8 ± 1

Notes. [(a)]In units of 10^{-15} erg s^{-1} cm^{-2} Å^{-1}. [(b)]In units of 10^{-13} erg s^{-1} cm^{-2}. [(c)]The UV spectrum does not cover the 1900 Å blend. [(d)]Presents broad absorption lines in the regions of C IVλ1549+He IIλ1640 and Si IVλ1397+O IV]λ1402. [(e)]We consider BLUE+BC when estimating fluxes and equivalent widths of Al IIIλ1860 and Si III]λ1892. [(f)]This source is optically classified as Pop. B, but the UV spectrum fits perfectly with the one of a Pop. A quasar.

relative intensity I/I_{tot}, FWHM, and shift for C IVλ1549 BLUE; Cols. 12–14 for C IVλ1549 BC; Cols. 15–17 for C IVλ1549 VBC; Cols. 18–20 for He IIλ1640 BLUE; Cols. 21–23 for He IIλ1640 BC; and Cols. 24–26 for He IIλ1640 VBC.

We have 10 out of 12 Pop. A sources and four out of 10 Pop. B quasars with C IV covered for analysis. The fits are remarkably good and allow for the 'plateau' found as an extension of the red wing of C IVλ1549 close to 1575 Å, which can usually be well reproduced by fitting C IVλ1549 and He IIλ1640 with the same FWHM for blueshifted, broad, and very broad components (Fine et al. 2010; Marziani et al. 2010). In general, Pop. A objects present a larger FWHM of the full profile, always $\geq$4900 km s^{-1}, with respect to Pop. B. Pop. A are also those that in general present higher asymmetries and shifts towards the blue. Apart from SDSSJ212329.46−005052.9, all Pop. A sources present a FWHM(C IV$_{\mathrm{BC}}$) $\leq$ 4500 km s^{-1}. The Pop. A3 SDSSJ210831.56−063022.5 is the source with the strongest blueshift, reaching $c(1/2) \approx -4980$ km s^{-1} and with similar values of fractional intensities along the profile (as can be seen in the top plot of Fig. 7).

In the case of Pop. B sources, we have found that the VBC accounts for only ~15% of the full profile. The widest VBC FWHM is seen in SDSSJ114358.52+052444.9, which reaches 11 848 km s^{-1} with a shift of 3822 km s^{-1}. This same source is the one that also presents the broadest FWHM of the BLUE (14 345 km s^{-1}) and larger shift (−1497 km s^{-1}). In all Pop. B cases, the BLUE component accounts for at least 50% of the C IVλ1549 full profile, but still a fraction that is lower than in Pop. A (~70%). Correspondingly, the Pop. A C IVλ1549 profiles in general present higher blueshifts and asymmetry indexes than the ones measured in Pop. B.

The top and bottom panels from Fig. 7 show the relation between the rest-frame equivalent widths of C IVλ1549 and the centroid velocities at 1/2 peak intensity ($c(1/2)$ and FWHM respectively). We also include in the figure the bright, high-z xA sample of Martínez-Aldama et al. (2018) as well as the high-z data from S17 and the FOS low-z data from S07. Our data are in good agreement with the ones of Martínez-Aldama et al. (2018) and S17. Our sample, together with the high-L comparison samples, presents smaller values of C IVλ1549 equivalent width when compared with the FOS data. Additionally, the high-z, high-L sources are those that present the most blueshifted C IVλ1549 profiles among all quasars (Shen et al. 2011; Rankine et al. 2020; Vietri et al. 2018, 2020). The Pearson correlation coefficient between W and $c(1/2)$ of C IVλ1549 for the Pop. A sources is −0.64 (with $\rho = 2.1 \times 10^{-12}$) and their relation is given in Table 7. There is also a correlation between W and FWHM C IVλ1549 with $r \approx -0.49$, if we restrict the samples to only Pop. A objects (Table 7).

Figure 8 presents the strong correlation between FWHM and $c(1/2)$ of the C IV line, with a Pearson $r \approx -0.90$ for high-z Pop. A sources:

$$c(1/2)_{\mathrm{C\,IV}} = (-0.68 \pm 0.10) FWHM(\mathrm{C\,IV}) + (2000 \pm 737). \quad (2)$$

Table 9. Measurements on the 1900 Å blend.

Source	Al III λ1860 BLUE			Al III λ1860 BC			Si III] λ1892 BLUE			Si III] λ1892 BC		
	$I/I_{\rm tot}$	*FWHM* [km s^{-1}]	Shift [km s^{-1}]	$I/I_{\rm tot}$	*FWHM* [km s^{-1}]	Shift [km s^{-1}]	$I/I_{\rm tot}$	*FWHM* [km s^{-1}]	Shift [km s^{-1}]	$I/I_{\rm tot}$	*FWHM* [km s^{-1}]	Shift [km s^{-1}]
(1)	(2)	(3)	(4)	(5)	(6)	(7)	(8)	(9)	(10)	(11)	(12)	(13)
Population A												
SDSSJ005700.18+143737.7	0.47 ± 0.04	3268 ± 396	−1686 ± 202	0.53 ± 0.04	2792 ± 283	0 ± 10	0.36 ± 0.07	3268 ± 392	−1686 ± −202	0.64 ± 0.13	2792 ± 335	−3 ± 11
SDSSJ132012.33+142037.1	0.27 ± 0.02	1731 ± 210	−967 ± 116	0.72 ± 0.06	2029 ± 206	0 ± 10	0.00	...	...	0.08 ± 0.02	3030 ± 364	0 ± 10
SDSSJ135831.78+050522.8	0.00	...	...	1.00 ± 0.08	4225 ± 428	0 ± 10	0.00	...	...	1.00 ± 0.21	4225 ± 507	0 ± 10
Q 1410+096	0.00	...	...	1.00 ± 0.08	2604 ± 264	279 ± 33	0.00	...	...	1.00 ± 0.21	2604 ± 312	279 ± 33
SDSSJ161458.33+144836.9	0.00	...	...	1.00 ± 0.08	3374 ± 342	0 ± 10	0.00	...	...	1.00 ± 0.21	3374 ± 405	0 ± 10
SDSSJ210524.49+000407.3	0.61 ± 0.05	4365 ± 529	−2003 ± 240	0.39 ± 0.03	3672 ± 372	0 ± 10	0.23 ± 0.04	3415 ± 410	−2002 ± −240	0.77 ± 0.16	4169 ± 500	0 ± 10
SDSSJ210831.56−063022.5	0.36 ± 0.03	3181 ± 386	−1951 ± 234	0.64 ± 0.05	4173 ± 423	0 ± 10	0.21 ± 0.04	3187 ± 382	−1951 ± −234	0.79 ± 0.17	4173 ± 501	0 ± 10
SDSSJ212329.46−005052.9	0.00	...	...	1.00 ± 0.08	5122 ± 519	0 ± 10	0.00	...	...	1.00 ± 0.21	5122 ± 615	0 ± 10
SDSSJ235808.54+012507.2	0.00	...	...	1.00 ± 0.08	3243 ± 329	0 ± 10	0.00	...	...	1.00 ± 0.21	3243 ± 389	0 ± 10
Median	0.00 ± 0.36	3224 ± 723	−1818 ± 457	1.00 ± 0.36	3374 ± 1381	...	0.23 ± 0.07	3268 ± 114	−1951 ± 158	...	3374 ± 1381	...
Population B												
SDSSJ114358.52+052444.9	0.00	...	...	1.00 ± 0.08	3967 ± 402	0 ± 10	0.00	...	...	1.00 ± 0.18	3967 ± 476	−3 ± 11
SDSSJ115954.33+201921.1	0.00	...	...	1.00 ± 0.08	4999 ± 506	0 ± 10	0.00	...	...	1.00 ± 0.18	4999 ± 600	0 ± 10
SDSSJ120147.90+120630.2	0.00	...	...	1.00 ± 0.08	3999 ± 405	0 ± 10	0.00	...	...	1.00 ± 0.18	3999 ± 480	0 ± 10
SDSSJ141546.24+112943.4	0.00	...	...	1.00 ± 0.08	5105 ± 517	0 ± 10	0.00	...	...	1.00 ± 0.18	5105 ± 613	0 ± 10
SDSSJ153830.55+085517.0 [(a)]	0.00	...	...	1.00 ± 0.08	3085 ± 313	0 ± 10	0.00	...	...	1.00 ± 0.18	3085 ± 370	0 ± 10
Median	...	...	...	...	3999 ± 1032	...	...	...	...	...	3999 ± 1032	...

Source	C III] λ1909 BC			C III] λ1909 VBC			C III] λ1909 NC			Fe III λ1914		
	$I/I_{\rm tot}$	*FWHM* [km s^{-1}]	Shift [km s^{-1}]	$I/I_{\rm tot}$	*FWHM* [km s^{-1}]	Shift [km s^{-1}]	$I/I_{\rm tot}$	*FWHM* [km s^{-1}]	Shift [km s^{-1}]	$I/I_{\rm tot}$	*FWHM* [km s^{-1}]	Shift [km s^{-1}]
(1)	(14)	(15)	(16)	(17)	(18)	(19)	(20)	(21)	(22)	(23)	(24)	(25)
Population A												
SDSSJ005700.18+143737.7	1.00 ± 0.18	2400 ± 288	0 ± 10	...	...	...	...	...	...	1.00 ± 0.12	2792 ± 335	1494 ± 179
SDSSJ132012.33+142037.1	0.92 ± 0.17	3030 ± 364	0 ± 10	...	...	...	...	...	...	1.00 ± 0.12	3030 ± 364	1876 ± 225
SDSSJ135831.78+050522.8	1.00 ± 0.18	2720 ± 326	0 ± 10	...	...	...	...	...	...	1.00 ± 0.12	4231 ± 508	1033 ± 124
Q 1410+096	1.00 ± 0.18	2604 ± 312	278 ± 58	...	...	...	...	...	...	1.00 ± 0.12	1607 ± 193	1253 ± 150
SDSSJ161458.33+144836.9	1.00 ± 0.18	3319 ± 398	0 ± 10	...	...	...	...	...	...	0.00	...	...
SDSSJ210524.49+000407.3	1.00 ± 0.18	2577 ± 309	0 ± 10	...	...	...	...	...	...	1.00 ± 0.12	3672 ± 441	771 ± 93
SDSSJ210831.56−063022.5	1.00 ± 0.18	3156 ± 379	0 ± 10	...	...	...	...	...	...	1.00 ± 0.12	2177 ± 261	2102 ± 252
SDSSJ212329.46−005052.9	1.00 ± 0.18	3125 ± 375	0 ± 10	...	...	...	...	...	...	0.00	...	...
SDSSJ235808.54+012507.2	1.00 ± 0.18	3243 ± 389	0 ± 10	...	...	...	...	...	...	1.00 ± 0.12	3204 ± 384	111 ± 13
Median	...	2760 ± 552	...	...	...	...	...	...	...	...	2298 ± 1224	1143 ± 597
Population B												
SDSSJ114358.52+052444.9	0.50 ± 0.10	3967 ± 476	0 ± 10	0.50 ± 0.05	7038 ± 1253	2842 ± 369	0.02 ± 0.01	1000 ± 178	0 ± 10	0.00	...	...
SDSSJ115954.33+201921.1	0.64 ± 0.13	4999 ± 600	0 ± 10	0.36 ± 0.03	6563 ± 1168	1998 ± 260	0.01 ± 0.01	733 ± 130	0 ± 10	0.00	...	...
SDSSJ120147.90+120630.2	0.70 ± 0.14	3999 ± 480	0 ± 10	0.30 ± 0.03	7046 ± 1254	2207 ± 287	0.01 ± 0.01	999 ± 178	0 ± 10	0.00	...	...
SDSSJ141546.24+112943.4	0.64 ± 0.13	4101 ± 492	0 ± 10	0.36 ± 0.03	7365 ± 1311	3134 ± 407	0.10 ± 0.01	1062 ± 189	0 ± 10	0.00	...	...
SDSSJ153830.55+085517.0 [(a)]	1.00 ± 0.20	3104 ± 372	28 ± 16	...	...	...	0.00	...	...	1.00 ± 0.12	3141 ± 377	783 ± 94
Median	0.64 ± 0.06	3999 ± 134	...	0.36 ± 0.05	7042 ± 206	2524 ± 760	...	999 ± 83	...	...	...	...

Notes. [(a)] UV line profiles of this source were fitted with Lorentzian shapes. See note in the Appendix A (Fig. A.14).

Table 10. Measurements on the C IVλ1549+He IIλ1640 full line profiles and SPECFIT analysis.

Source	C IVλ1549 full profile							C IVλ1549									He IIλ1640								
								BLUE			BC			VBC			BLUE			BC			VBC		
	FWHM [km s^{-1}]	A.I.	Kurt.	$c(\frac{1}{4})$ [km s^{-1}]	$c(\frac{1}{2})$ [km s^{-1}]	$c(\frac{3}{4})$ [km s^{-1}]	$c(\frac{9}{10})$ [km s^{-1}]	I/I_{tot}	*FWHM* [km s^{-1}]	Shift [km s^{-1}]	I/I_{tot}	*FWHM* [km s^{-1}]	Shift [km s^{-1}]	I/I_{tot}	*FWHM* [km s^{-1}]	Shift [km s^{-1}]	I/I_{tot}	*FWHM* [km s^{-1}]	Shift [km s^{-1}]	I/I_{tot}	*FWHM* [km s^{-1}]	Shift [km s^{-1}]	I/I_{tot}	*FWHM* [km s^{-1}]	Shift [km s^{-1}]
(1)	(2)	(3)	(4)	(5)	(6)	(7)	(8)	(9)	(10)	(11)	(12)	(13)	(14)	(15)	(16)	(17)	(18)	(19)	(20)	(21)	(22)	(23)	(24)	(25)	(26)
Population A																									
SDSSJ005700.18+143737.7	8648 ± 562	−0.38 ± 0.01	0.40 ± 0.01	−4951 ± 334	−3994 ± 181	−3272 ± 272	−2604 ± 326	0.81 ± 0.05	13187 ± 1846	−2318 ± 278	0.19 ± 0.05	2808 ± 298	0 ± 10	...	...	...	0.67 ± 0.04	13187 ± 1846	−4249 ± 510	0.33 ± 0.02	2808 ± 298	0 ± 10	...	...	...
SDSSJ132012.33+142037.1	5549 ± 399	−0.36 ± 0.01	0.37 ± 0.01	−2956 ± 263	−2407 ± 124	−1830 ± 177	−1419 ± 190	0.72 ± 0.04	8739 ± 1223	−1446 ± 174	0.28 ± 0.03	3278 ± 348	0 ± 10	...	...	...	0.60 ± 0.04	9837 ± 1377	−3388 ± 407	0.40 ± 0.02	3278 ± 348	0 ± 10	...	...	...
SDSSJ135831.78+050522.8	7365 ± 655	−0.27 ± 0.03	0.30 ± 0.01	−3188 ± 416	−2460 ± 190	−1808 ± 256	−1556 ± 187	0.52 ± 0.03	11983 ± 1678	−1909 ± 229	0.48 ± 0.02	4404 ± 468	0 ± 10	...	...	...	0.55 ± 0.03	11983 ± 1678	−3386 ± 406	0.45 ± 0.03	4404 ± 468	0 ± 10	...	...	...
Q 1410+096	6311 ± 552	−0.18 ± 0.05	0.33 ± 0.01	−2604 ± 374	−1746 ± 179	−1052 ± 172	−1691 ± 90	0.41 ± 0.03	10881 ± 1523	−1526 ± 183	0.59 ± 0.01	3293 ± 350	0 ± 10	...	...	...	0.53 ± 0.03	9369 ± 1312	−7880 ± 946	0.47 ± 0.03	3292 ± 350	0 ± 10	...	...	...
SDSSJ161458.33+144836.9	5790 ± 554	−0.27 ± 0.03	0.30 ± 0.02	−2779 ± 327	−2394 ± 139	−1894 ± 190	−1519 ± 168	0.59 ± 0.04	9333 ± 1307	−1609 ± 193	0.41 ± 0.01	3816 ± 406	0 ± 10	...	...	...	0.66 ± 0.04	9556 ± 1338	−5483 ± 658	0.34 ± 0.02	3816 ± 406	0 ± 10	...	...	...
PKS 2000−330	4950 ± 346	−0.33 ± 0.01	0.39 ± 0.01	−2373 ± 226	−1923 ± 104	−1465 ± 154	−1155 ± 169	0.70 ± 0.04	7340 ± 1028	−1300 ± 156	0.30 ± 0.02	3142 ± 334	0 ± 10	...	...	...	...	...	...	...	...	...	...	...	...
SDSSJ210524.49+000407.3	8443 ± 592	−0.15 ± 0.01	0.43 ± 0.01	−5060 ± 297	−4695 ± 134	−4452 ± 228	−4175 ± 279	0.89 ± 0.05	10418 ± 1459	−3926 ± 471	0.11 ± 0.02	3504 ± 372	−82 ± 20	...	...	...	0.55 ± 0.03	10418 ± 1459	−8749 ± 1050	0.45 ± 0.03	3504 ± 372	−81 ± 20	...	...	...
SDSSJ210831.56−063022.5	9389 ± 619	−0.30 ± 0.01	0.42 ± 0.01	−5744 ± 365	−4982 ± 177	−4284 ± 264	−3709 ± 334	0.87 ± 0.05	13618 ± 1907	−3250 ± 390	0.13 ± 0.01	4340 ± 461	0 ± 10	...	...	...	0.70 ± 0.04	13618 ± 1907	−3250 ± 390	0.30 ± 0.02	4340 ± 461	0 ± 10	...	...	...
SDSSJ212329.46−005052.9	7978 ± 524	−0.21 ± 0.01	0.42 ± 0.01	−3752 ± 332	−3311 ± 139	−2876 ± 231	−2551 ± 277	0.72 ± 0.04	10217 ± 1430	−2694 ± 323	0.28 ± 0.01	5457 ± 580	0 ± 10	...	...	...	0.63 ± 0.04	10217 ± 1430	−4233 ± 508	0.37 ± 0.02	5457 ± 580	0 ± 10	...	...	...
SDSSJ235808.54+012507.2	6504 ± 398	−0.25 ± 0.01	0.44 ± 0.01	−3197 ± 245	−2727 ± 114	−2312 ± 186	−2029 ± 235	0.80 ± 0.05	8302 ± 1162	−2163 ± 260	0.20 ± 0.01	3468 ± 369	0 ± 10	...	...	...	0.49 ± 0.03	9231 ± 1292	−5323 ± 639	0.51 ± 0.03	3468 ± 369	0 ± 10	...	...	...
Median	6934 ± 2406	−0.27 ± 0.10	0.39 ± 0.08	−3192 ± 1828	−2593 ± 1426	−2103 ± 1359	−1860 ± 1062	0.72 ± 0.19	10317 ± 2820	−2036 ± 1053	0.28 ± 0.19	3486 ± 927	...	...	...	...	0.60 ± 0.11	10217 ± 2427	−4249 ± 2095	0.4 ± 0.11	3504 ± 1048	...	...	...	...
Population B																									
SDSSJ114358.52+052444.9	7078 ± 766	−0.30 ± 0.05	0.27 ± 0.01	−3049 ± 511	−2059 ± 230	−1375 ± 204	−1147 ± 185	0.60 ± 0.06	14345 ± 1037	−1497 ± 180	0.24 ± 0.04	5055 ± 365	0 ± 10	0.16 ± 0.02	11848 ± 2109	3822 ± 515	0.57 ± 0.06	14345 ± 1037	−3216 ± 433	0.17 ± 0.02	5055 ± 365	0 ± 10	0.26 ± 0.03	11848 ± 2109	2540 ± 342
SDSSJ115954.33+201921.1	5741 ± 585	−0.08 ± 0.05	0.29 ± 0.01	−1671 ± 444	−1851 ± 122	−1516 ± 166	−1253 ± 174	0.54 ± 0.05	9933 ± 718	−1307 ± 157	0.32 ± 0.05	5716 ± 413	0 ± 10	0.14 ± 0.01	8458 ± 1506	4397 ± 592	0.36 ± 0.04	9933 ± 718	−1307 ± 176	0.07 ± 0.01	5716 ± 413	0 ± 10	0.58 ± 0.06	8458 ± 1506	4397 ± 592
SDSSJ120147.90+120630.2	4995 ± 475	−0.08 ± 0.04	0.32 ± 0.01	−1354 ± 284	−1133 ± 104	−1061 ± 148	−1015 ± 132	0.50 ± 0.05	7464 ± 540	−1454 ± 174	0.35 ± 0.05	3945 ± 285	0 ± 10	0.15 ± 0.01	6710 ± 1194	1508 ± 203	0.44 ± 0.04	7464 ± 540	−4676 ± 630	0.09 ± 0.01	3945 ± 285	0 ± 10	0.47 ± 0.05	6710 ± 1194	1508 ± 203
SDSSJ153830.55+085517.0	5819 ± 448	−0.41 ± 0.02	0.35 ± 0.02	−2841 ± 303	−2108 ± 147	−1381 ± 187	−961 ± 185	0.68 ± 0.07	10024 ± 725	−992 ± 119	0.32 ± 0.05	4313 ± 312	0 ± 10	...	...	...	0.48 ± 0.05	10024 ± 725	−992 ± 134	0.52 ± 0.08	4313 ± 312	0 ± 10	...	...	...
Median	5780 ± 1474	−0.17 ± 0.21	0.30 ± 0.06	−2256 ± 1563	−1955 ± 783	−1378 ± 342	−1081 ± 252	0.57 ± 0.15	9978 ± 2162	−1380 ± 415	0.30 ± 0.07	4129 ± 1268	...	0.15 ± 0.01	8458 ± 2569	3822 ± 1444	0.46 ± 0.16	9978 ± 2087	−2261 ± 2920	0.14 ± 0.24	4129 ± 1255	...	0.47 ± 0.16	8458 ± 2569	2540 ± 1444

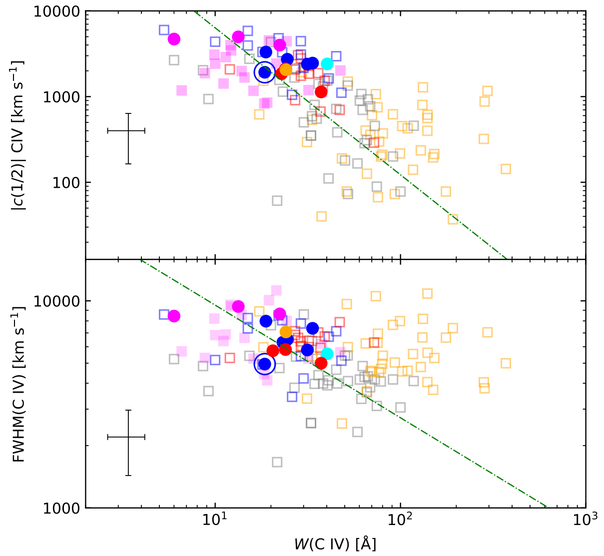

Fig. 7. Comparison between the different properties of the C IV emission line profile. *Top*: relation between centroid velocity at 1/2 intensity ($c(1/2)$) and rest-frame equivalent width of C IVλ1549. *Bottom*: FWHM of C IVλ1549 versus W(C IV). Colour scheme for our sample is the same as in Fig. 4. Filled magenta squares indicate data from Martínez-Aldama et al. (2018). Blue and red open squares represent Pop. A and Pop. B HE sources from S17. Low-z FOS data from S07 are represented by grey (Pop. A) and orange (Pop. B) squares. Green point-dashed lines indicate the linear regression obtained through the bisector method including only the Pop. A sources from the four samples. Error bars refer to 1σ level of confidence and were estimated only for our sample.

This relation is in good agreement with previous results (e.g. Coatman et al. 2016; Marziani et al. 2016b; Sulentic et al. 2017; Sun et al. 2018; Vietri et al. 2018, and references therein). As the blueshift of C IV increases, FWHM(C IV) is likely to increase as well. Both C IV FWHM and blueshift parameterised by $c(1/2)$ show a clear increase from spectral types A1 to A3, the latter being those with the highest blueshifts (median value ≈ -4500 km s^{-1}) and the widest FWHM (median ≈ 9000 km s^{-1}).

In the case of C IVλ1549 in Pop. B sources, the shifts at 1/2 flux intensities are also displaced towards blue wavelengths with average value of $c(1/2) = -1681$ km s^{-1} and mean $FWHM \approx 5940$ km s^{-1}, somewhat smaller than for Pop. A. However, the $c(1/2)$ values for the Pop. B sources from our sample are still higher than the majority of the low-luminosity and low-redshift quasars, which usually present a $c(1/2) \leq 200$ km s^{-1}. Low-luminosity Pop. B spectra show a sort of dichotomy in the C IVλ1549 shift distribution: a fraction of sources remains unshifted or with modest shifts to the blue (the orange and grey "cloud" of points in Fig. 8). The FOS low-luminosity and low-redshift sources tend to present smaller $c(1/2)$ in the C IVλ1549 emission line when compared with our data. This indicates that the C IVλ1549 blueshifted components seen in higher-luminosity sources are more prominent than the ones observed in quasars of lower luminosities.

5.3.3. Si IVλ1397+O IV]λ1402

Table 11 presents the measurements on the full profile of Si IVλ1397+O IV]λ1402. We report values of FWHM (Col. 2), A.I. (Col. 3), kurtosis (Col. 4), $c(1/2)$, (Col. 5), and $c(9/10)$ (Col. 6). Si IVλ1397+O IV]λ1402 BC is set at rest-frame and our initial guess for this component takes into account the results obtained for the C IV$_{\rm BC}$ after fitting the C IVλ1549+He IIλ1640 region. SDSSJ141546.24+112943.4 has very strong and wide absorption lines in this region of the UV spectra, which makes it difficult to perform a reliable fitting (see Fig. A.12).

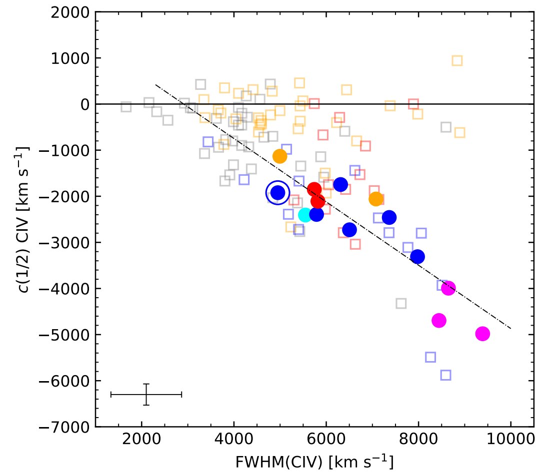

Fig. 8. Centroid velocity at 1/2 flux intensity, $c(1/2)$, for the C IVλ1549 emission line versus the FWHM of the full profile of C IV. Filled circles represent our sample and the colour scheme is the same as in Fig. 4. Blue and red open squares are high-redshift sources from S17. Low-z Pop. A and Pop. B are represented by grey and orange open squares, respectively. Dashed line represents the least squares linear regression presented in Eq. (2), including only Pop. A sources. Error bars refer to 1σ level of confidence for our sample.

Table 11. Measurements on the full profiles of Si IVλ1397+O IV]λ1402.

Source (1)	*FWHM* [km s^{-1}] (2)	A.I. (3)	Kurtosis (4)	$c(1/2)$ [km s^{-1}] (5)	$c(9/10)$ [km s^{-1}] (6)
Population A					
SDSSJ005700.18+143737.7	8659 ± 1202	−0.34 ± 0.02	0.36 ± 0.03	−2110 ± 377	−858 ± 443
SDSSJ132012.33+142037.1	5128 ± 859	−0.26 ± 0.05	0.34 ± 0.01	−376 ± 249	131 ± 293
SDSSJ135831.78+050522.8	7438 ± 1658	−0.27 ± 0.07	0.31 ± 0.01	−150 ± 534	499 ± 395
Q 1410+096	5430 ± 790	0.00 ± 0.09	0.40 ± 0.01	750 ± 157	666 ± 335
SDSSJ161458.33+144836.9	7370 ± 860	−0.26 ± 0.06	0.48 ± 0.01	−392 ± 227	680 ± 844
PKS 2000−330	3494 ± 329	0.32 ± 0.13	0.55 ± 0.02	888 ± 63	54 ± 112
SDSSJ210831.56−063022.5	9253 ± 1880	−0.24 ± 0.05	0.28 ± 0.03	−2613 ± 481	−1618 ± 452
SDSSJ212329.46−005052.9	6157 ± 892	−0.06 ± 0.05	0.40 ± 0.01	−868 ± 190	−635 ± 396
SDSSJ235808.54+012507.2	7135 ± 974	−0.14 ± 0.03	0.40 ± 0.01	−533 ± 252	−55 ± 443
Median	7135 ± 1888	−0.14 ± 0.20	0.40 ± 0.04	−392 ± 718	−55 ± 1134
Population B					
SDSSJ114358.52+052444.9	7070 ± 1027	−0.11 ± 0.05	0.40 ± 0.01	184 ± 242	394 ± 439
SDSSJ115954.33+201921.1	6813 ± 1372	−0.12 ± 0.07	0.34 ± 0.01	257 ± 396	644 ± 378
SDSSJ120147.90+120630.2	5000 ± 717	−0.18 ± 0.20	0.34 ± 0.04	667 ± 156	609 ± 315
SDSSJ153830.55+085517.0	5906 ± 1222	−0.18 ± 0.02	0.36 ± 0.01	159 ± 416	504 ± 413
Median	6359 ± 1197	−0.15 ± 0.06	0.35 ± 0.03	220 ± 181	556 ± 141

Regarding the BLUE of Si IVλ1397+O IV]λ1402, they are very wide (even if they are apparently not as wide as in C IVλ1549+He IIλ1640), reaching more than 6000 km s^{-1} in all cases, and representing a significant percentage of the full emission line profile. The shifts towards shorter wavelength are also smaller than for C IVλ1549, but they are still very high, going from 800 to 2700 km s^{-1}, with the extreme amplitude of SDSSJ135831.78+050522.8 that reaches $\approx$4400 km s^{-1}.

The fluxes of C IVλ1549 and Si IVλ1397 presented in Table 8 indicate that on average Pop. A presents higher values of the C IVλ1549/Si IVλ1397 ratio ($\approx$0.69) than Pop. B ($\approx$0.49). This discrepancy may be linked to differences in chemical abundances with Pop. A sources being systematically more metal

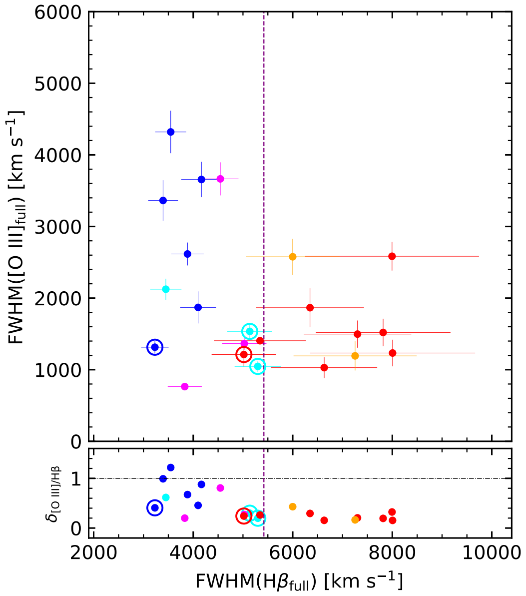

Fig. 9. Relation between Hβ and [O III] emission lines. *Top panel*: FWHM of the full profile of [O III]λ5007 vs. FWHM of the full profile of Hβ. *Bottom panel*: ratio $\delta_{[\mathrm{O\,III}]/\mathrm{H}\beta}$ = FWHM([O III]$_{\mathrm{full}}$)/FWHM(Hβ_{full}) vs. FWHM of the full profile of Hβ. As in Fig. 4, each colour represent one different spectral type, and symbols surrounded by open circles indicate the radio-loud quasars.

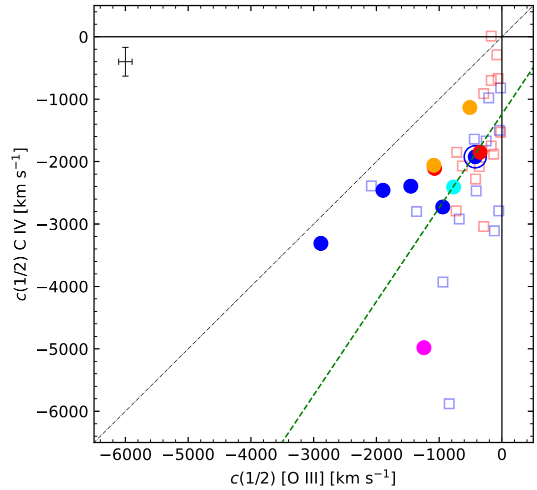

Fig. 10. Centroid velocity at 1/2 flux intensity (c(1/2)) of C IVλ1549 vs. c(1/2) of [O III]$\lambda\lambda$4959,5007. Blue and red open squares show the HE Pop. A and Pop. B sources studied by M09 and S17. Colour scheme is the same as in Fig. 4. The green line indicates the linear regression between c(1/2) of C IVλ1549 and [O III]$\lambda\lambda$4959,5007 obtained through the orthogonal least square method. The error bars refer to 1σ level of confidence for our sample.

rich (cf. Śniegowska et al. 2021; Punsly et al. 2020). However, the issue goes beyond the scope of the present work and will be discussed elsewhere.

6. Discussion

In the previous section, we show that Pop. A and Pop. B sources may reflect different contributions of line emitting gas that produces prominent blueshifted features and is most likely associated with an outflow. To shed further light on the role of outflows, we now report an interline comparison in both the optical and UV spectral regions. We highlight the effect of the outflowing components on the estimate of physical parameters such as black hole mass and Eddington ratio.

6.1. Defining the outflow

6.1.1. Hβ and [O III]$\lambda\lambda$4959,5007

The relation between the FWHM of the full profiles of Hβ and O III]λ5007 is shown in Fig. 9. In general, the two populations present a FWHM(Hβ_{full}) higher than FWHM([O III]$_{\mathrm{full}}$), as expected from previous observations (Sulentic et al. 2004, 2007; Zamfir et al. 2010; M09). At low-z, only in the case of the 'blue-outliers' the [O III]$\lambda\lambda$4959,5007 profiles appear to be very boxy-shaped and with the $FWHM$ > 1000 km s^{-1}. Some of these sources are NLSy1s and the [O III]$\lambda\lambda$4959,5007 FWHM is becoming comparable to the one of the broad Hβ profile sources (Zamanov et al. 2002; Komossa et al. 2008, 2018; Cracco et al. 2016; Berton & Järvelä 2021). At high z and high luminosity the [O III]$\lambda\lambda$4959,5007 profiles often appear much broader, as do also the Hβ broad profiles (Carniani et al. 2015; Fiore et al. 2017; Villar Martín et al. 2020). Two cases in point, taken from previous works, are 2QZJ002830.4−281706 at z = 2. (Cano-Díaz et al. 2012; Carniani et al. 2015) and HE 0940−1050 at z = 3.1 (Marziani et al. 2017a). We have four sources that present [O III]$\lambda\lambda$4959,5007 FWHM above 3000 km s^{-1}, comparable to the Hβ FWHM, with one extraordinary case in which FWHM(Hβ_{full}) is smaller than FWHM([O III]$_{\mathrm{full}}$), (SDSSJ135831.78+050522.8, Pop. A1), with FWHM (Hβ_{full}) ≈ 3550 km s^{-1} and FWHM([O III]$_{\mathrm{full}}$) ≈ 4320 km s^{-1} (see Fig. A.10). Although FWHM of [O III]$\lambda\lambda$4959,5007 $\gtrsim$2000 km s^{-1} are frequently observed at high luminosity, some extreme values should be taken with care because the [O III]$\lambda\lambda$4959,5007 profiles are weak and broad: it is difficult to properly define the [O III]$\lambda\lambda$4959,5007 profiles especially when the broad Hβ red wing is strong.

6.1.2. [O III]$\lambda\lambda$4959,5007 versus C IVλ1549

Figure 10 shows the relation between c(1/2) for [O III]$\lambda\lambda$4959,5007 and C IVλ1549. The HE comparison sample analysed in M09 and S17 is included. The sources that present strong shifts in the [O III]$\lambda\lambda$4959,5007 emission line profiles will also present it in C IVλ1549, in agreement with the HE data. Both lines show a correlation between their widths and shifts (Fig. 6 for [O III]$\lambda\lambda$4959,5007 and Fig. 8 for C IVλ1549) indicating that the broadening is mainly associated with a blueshifted component that is increasing in prominence with increasing shift. The least-squares linear regression of Fig. 10 (considering both HEMS and our sample) is given by:

$$c(1/2)_{\mathrm{C\,IV}} = (1.50 \pm 0.31)c(1/2)_{[\mathrm{O\,III}]} + (-1239 \pm 276), \quad (3)$$

in a good agreement with the study of Coatman et al. (2019). The trend (actually, a weak, marginally significant correlation at a 3σ confidence level) of Fig. 10 raises the issue of the relation between [O III]$\lambda\lambda$4959,5007 and C IVλ1549 outflows. There is evidence suggesting that the semi-broad component of [O III]$\lambda\lambda$4959,5007 W remains almost constant with luminosity (Marziani et al. 2016a, Sect. 4.3), overwhelming the narrow, core component. The narrow component is however mainly associated with the NLR that may extend up to tens of kpc (Bennert et al. 2002, 2006). The dispersion in the relation with more sources around 0 shift in [O III]$\lambda\lambda$4959,5007 might

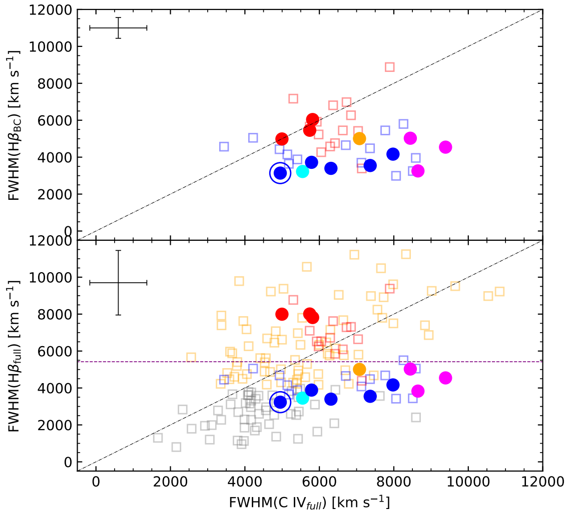

Fig. 11. FWHM(H$\beta_{\rm BC}$) vs. FWHM(C IV$_{\rm full}$) and FWHM(H$\beta_{\rm full}$) vs. FWHM(C IV$_{\rm full}$). Sources are identified according to the different bins of spectral types following colour scheme from Fig. 4. Blue and red open squares represent Pop. A and Pop. B sources from S17 and grey and orange open squares indicate Pop. A and Pop. B from S07, respectively. Horizontal purple line indicates the A-B boundary and the error bars on the *top left of the plots* refer to 1σ level of confidence for our sample.

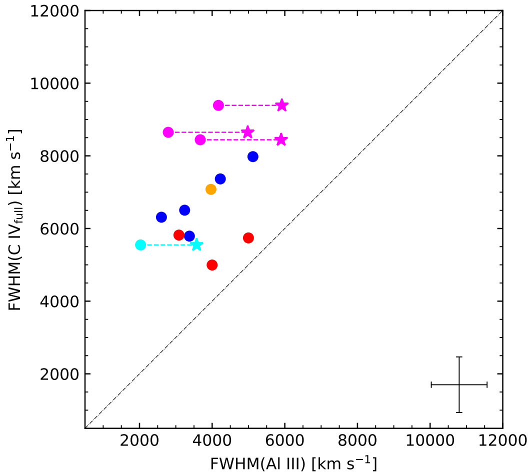

Fig. 12. C IV$_{\rm full}$ relation with Al IIIλ1860. Colour scheme is the same as in Fig. 4. Data points joined by a dashed line are those for which a significant blueshifted emission component has been isolated. The data points to the left refer to the Al IIIλ1860 BC only and the right ones (star symbol) to the full profile FWHM (BC+BLUE). Error bars refer to 1σ level of confidence.

be explained by a narrow component whose strength may depend on the past AGN evolution (Storchi-Bergmann et al. 2018). It is therefore not surprising that, even if a large C IVλ1549 shift is measured, the [O III]$\lambda\lambda$4959,5007 profile may be unshifted or show only a modest blueshift. However, the presence of a shift correlation and the relatively large [O III]$\lambda\lambda$4959,5007/C IVλ1549 FWHM ratio support a physical connection between an inner outflow on scales of a few hundreds gravitational radii where the BLUE C IVλ1549 component is emitted, and an outflow at the outer edge of the BLR, beyond 10^4–10^5 gravitational radii (Zamanov et al. 2002), where the [O III]$\lambda\lambda$4959,5007 semibroad component likely originates. The nature of this connection remains unclear. It is beyond the scope of the present paper and might be investigated elsewhere.

6.1.3. C IVλ1549 versus Hβ

The top panel of Fig. 11 represents the relation between FWHM(H$\beta_{\rm BC}$) and FWHM(C IV$_{\rm full}$), including the S17 sample. Our data is in agreement with this comparison sample in terms of a clear A-B separation. The Pop. A sources seem to present a trend from A1 to A3 in the FWHM(C IV$_{\rm full}$) where the A3 sources show the largest values. The FWHM(C IV$_{\rm full}$) is larger than the FWHM(H$\beta_{\rm BC}$), and the widths of the two lines are not correlated. There is a degeneracy between C IVλ1549 and Hβ: to a single value of Hβ FWHM corresponds a wide range of C IVλ1549 FWHM (cf. S07; Capellupo et al. 2015; Mejía-Restrepo et al. 2016; Coatman et al. 2017). The systematically broader profile can be interpreted as a consequence of the dominance of the outflow component in the C IVλ1549 line profile (Marziani et al. 2019).

The bottom panel of Fig. 11 shows the FWHM(C IV$_{\rm full}$) vs. FWHM(H$\beta_{\rm full}$) where, apart from including S17 data, we also display the low-z sample from S07 for comparison. In this plot, the separation between Pop. A and Pop. B is even clearer: Pop. A sources show broader C IVλ1549, while those of Pop. B have values consistent with, or narrower, than Hβ.

6.1.4. C IVλ1549 versus Al IIIλ1860

Figure 12 shows FWHM of the full profiles of C IVλ1549 versus FWHM of Al IIIλ1860. The FWHM(C IV$_{\rm full}$) presents significantly higher values than FWHM(Al III). This indicates that the relation between C IVλ1549 and Al IIIλ1860 is similar to the one of C IVλ1549 and Hβ. In both cases, the C IVλ1549 FWHM tends to be larger: in particular, always significantly so for Pop. A and larger or consistent for Pop. B. The cyan and magenta dashed lines connect the FWHM estimated from the Al IIIλ1860 BC with and without a BLUE component: without the BLUE (stars), the Al IIIλ1860 FWHM becomes closer to, but remains significantly smaller than the FWHM of the C IVλ1549 full profile.

6.2. *Virial black hole mass estimates*

A comparison between the FWHM of Al IIIλ1860 and Hβ (BC and full) profiles is shown in Fig. 13. The figure includes the data from Marziani et al. (2022b, hereafter M22) that involve exclusively Pop. A sources. The FWHM of H$\beta_{\rm BC}$ is consistent with the FWHM of Al IIIλ1860 for Pop. A: their average ratio (FWHM Al III over FWHM Hβ) in our sample is $\approx 0.87 \pm 0.18$. The right panel of Fig. 13 shows a comparison between FWHM(Al III) vs. FWHM of full Hβ. The purple dotted vertical line indicates the A/B boundary as in Fig. 3. The location of our Pop. A objects remains in agreement with the results from M22, and with those for H$\beta_{\rm BC}$. There is a clear deviation from the 1:1 line in the location of Pop. B sources: for the 5 Population B sources of our sample the average ratio is just 0.57 ± 0.12 (cf. Marziani et al. 2017b). These results provide evidence that Pop. B Al IIIλ1860 is systematically narrower than Hβ full profile, most likely because of the strong VBC contribution. The ratio FWHM Al IIIλ1860 over H$\beta_{\rm BC}$ is in fair agreement $\approx 0.79 \pm 0.16$ for Pop. B, and therefore the Hβ VBC should not be included on the black hole mass estimation. The 20% difference between the FWHM H$\beta_{\rm BC}$

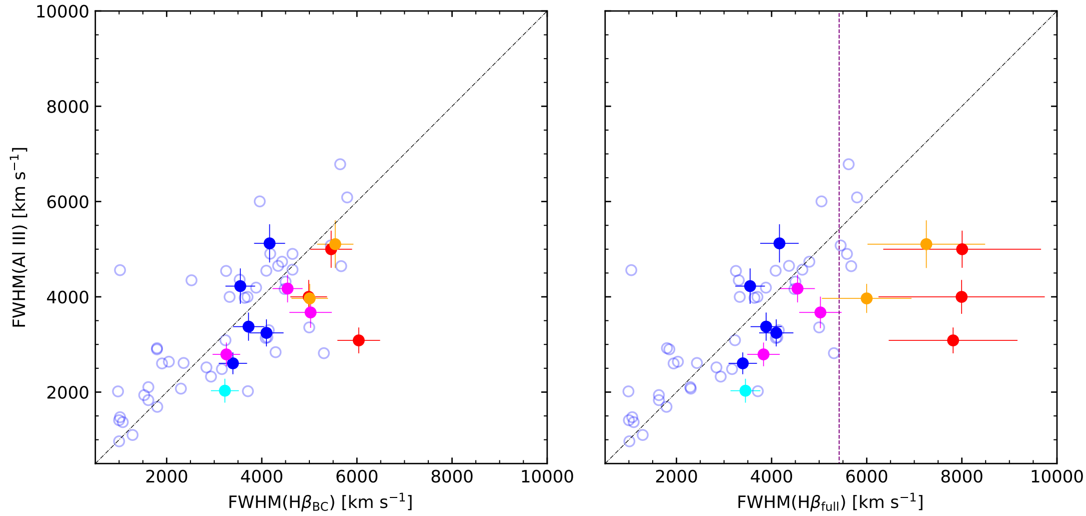

Fig. 13. FWHM(Al III) vs. FWHM(Hβ_{BC}), (*left panel*), and FWHM(Al III) vs. FWHM(Hβ_{full}), (*right panel*). Sources are identified according to the different bins of spectral types following colour scheme from Fig. 4. Blue open circles show the data from M22 Pop. A sources for a comparison. Vertical purple line indicates the A/B boundary for our sample.

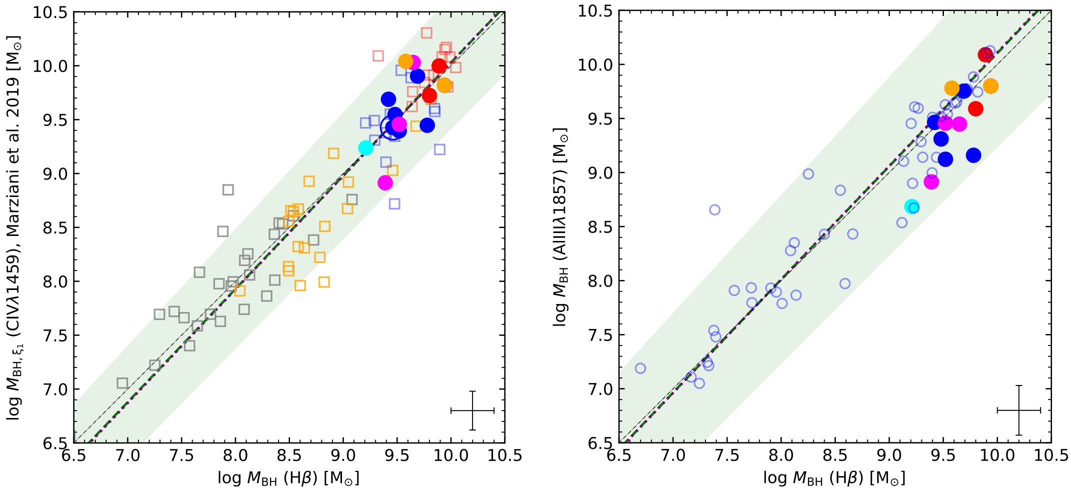

Fig. 14. M_{BH}(Hβ) compared to M_{BH}(C IV), (*left panel*) and to M_{BH}(Al III), (*right panel*). Open squares on the left plot represent the low- and high-redshift sources analysed by Marziani et al. (2019; blue and red for high-z and grey and orange for low-z Pop. A and Pop. B, respectively). Blue dots on the *right panel* are for the M22 data. Green and purple dashed lines indicate the linear regressions using bisector and orthogonal methods, respectively. Colour scheme is the same as in Fig. 4.

and FWHM Al IIIλ1860 for Pop. B sources is marginally significant and should be confirmed by larger samples.

The black hole masses are estimated through different scaling relations using emission lines such as those based on the FWHM of Hβ, Al IIIλ1860, and C IVλ1549. The scaling law of Vestergaard & Peterson (2006, hereafter VP06) was used to estimate the mass M_{BH} with FWHM Hβ_{BC}. We used Eq. (18) from Marziani et al. (2019, σ = 0.33) to estimate M_{BH} with the C IVλ1549 FWHM. The left panel of Fig. 14 presents a comparison between the M_{BH} estimates using the scaling law for C IVλ1549 from Marziani et al. (2019) and the Hβ scaling law of Vestergaard & Peterson (2006). The open squares in this plot indicate the data from Marziani et al. (2019), which include high- and low-z sources. Our sample agrees with the previous estimates and corresponds to the extreme cases, with the largest M_{BH} reaching 10^{10} $M_\odot$.

The plot of $M_{BH,Al\,III}$ vs. $M_{BH,H\beta}$ (right panel of Fig. 14) relies on the M_{BH} scaling law from M22. The $M_{BH,H\beta}$ and $M_{BH,Al\,III}$ values obtained for our sources are compatible within the confidence interval of the M22 scaling law for Al IIIλ1860. We caution that the relation given in this equation has been derived for Pop. A sources and, consequently, it may lead to larger uncertainties for Pop. B quasars. For these sources we apply a correction $\xi = FWHM_{H\beta,BC}/FWHM_{Al\,III} = 1.35 \pm 0.10$ to the FWHM(Al III), (Marziani et al. 2017a, who assumed FWHM Hβ_{BC} as the reference virial broadening estimator).

The equations that describe the relations between M_{BH} estimations using ξ-corrected C IVλ1549 and Al IIIλ1860 are listed in Table 12. Column 1 lists the method used for the linear regression (orthogonal and bisector); Cols. 2 and 3 present the linear and angular coefficients, along with the respective standard deviations; rms error and Pearson correlation coefficient r are reported in Cols. 4 and 5, respectively.

The original C IVλ1549 VP06 relation lacks a correction because of the bias introduced by non-virial broadening (i.e. by the blueshifted component; Brotherton et al. 2015;

Table 12. Linear relations between the different $M_{\rm BH}$ estimates using orthogonal and bisector methods.

Method (1)	$a \pm \delta a$ (2)	$b \pm \delta b$ (3)	rms (4)	CC (5)
	$M_{\rm BH,C\,IV,M19} = a + b * M_{\rm BH,H\beta,VP06}$			
Orthogonal	-0.495 ± 0.306	1.053 ± 0.034	0.315	0.949
Bisector	-0.471 ± 0.289	1.050 ± 0.032		
	$M_{\rm BH,Al\,III,M22} = a + b * M_{\rm BH,H\beta,VP06}$			
Orthogonal	-0.389 ± 0.431	1.050 ± 0.047	0.320	0.948
Bisector	-0.366 ± 0.411	1.047 ± 0.045		

Table 13. Weighted averaged masses, luminosity at 5100 Å, and Eddington ratio ($L/L_{\rm Edd}$), in logarithmic scale.

Source (1)	$M_{\rm BH,H\beta}$ (2)	$M_{\rm BH}$ (3)	L(1450 Å) (4)	L(5100 Å) (5)	$L/L_{\rm Edd}$ (6)
		Population A			
SDSSJ005700.18+143737.7	9.39 ± 1.41	9.37 ± 0.27	46.65 ± 5.60	46.41 ± 5.57	0.10 ± 0.01
SDSSJ132012.33+142037.1	9.21 ± 1.38	9.19 ± 0.14	46.74 ± 5.61	46.42 ± 5.57	0.03 ± 0.01
SDSSJ135831.78+050522.8	9.42 ± 1.41	9.56 ± 0.11	46.97 ± 5.64	46.67 ± 5.60	0.07 ± 0.01
Q 1410+096	9.52 ± 1.43	9.42 ± 0.20	47.11 ± 5.65	46.92 ± 5.63	0.32 ± 0.04
B 1422+231 [(a)]	9.96 ± 1.49	–	–	47.07 ± 5.65	−0.07 ± 0.01
SDSSJ161458.33+144836.9	9.48 ± 1.42	9.49 ± 0.10	47.05 ± 5.65	46.69 ± 5.60	0.04 ± 0.01
PKS 1937–101 [(a)]	10.14 ± 1.52	–	–	47.36 ± 5.68	0.05 ± 0.01
PKS 2000–330	9.46 ± 1.42	9.21 ± 0.04 [(c)]	46.58::	46.94 ± 5.63	0.30 ± 0.04
SDSSJ210524.47+000407.3	9.84 ± 1.48	9.83 ± 0.28 [(b)]	47.16 ± 5.66	46.89 ± 5.63	−0.13 ± 0.02
SDSSJ210831.56–063022.5	9.52 ± 1.43	9.63 ± 0.12	46.98 ± 5.64	46.43 ± 5.57	−0.26 ± 0.03
SDSSJ212329.46–005052.9	9.69 ± 1.45	9.77 ± 0.08	47.19 ± 5.66	46.92 ± 5.63	0.05 ± 0.01
SDSSJ235808.54+012507.2	9.78 ± 1.47	9.57 ± 0.31	46.85 ± 5.62	47.11 ± 5.65	0.15 ± 0.02
		Population B			
HE 0001–2340 [(a)]	9.63 ± 1.44	–	–	46.48 ± 5.58	−0.33 ± 0.04
[HB89] 0029+073 [(a)]	9.71 ± 1.46	–	–	46.81 ± 5.62	−0.07 ± 0.01
CTQ 0408 [(a)]	10.20 ± 1.53	–	–	47.26 ± 5.67	−0.12 ± 0.01
H 0055–2659 [(a)]	9.69 ± 1.45	–	–	46.75 ± 5.61	−0.12 ± 0.01
SDSSJ114358.52+052444.9	9.58 ± 1.44	9.75 ± 0.25	47.16 ± 5.66	46.39 ± 5.57	−0.05 ± 0.01
SDSSJ115954.33+201921.1	9.89 ± 1.48	9.90 ± 0.05	47.36 ± 5.68	46.84 ± 5.62	−0.23 ± 0.03
SDSSJ120147.90+120630.2	9.94 ± 1.49	9.89 ± 0.2	47.19 ± 5.66	47.09 ± 5.65	0.03 ± 0.01
SDSSJ141546.24+112943.4	9.80 ± 1.47	9.78 ± 0.07 [(b)]	47.08 ± 5.65	46.64 ± 5.60	−0.33 ± 0.04
SDSSJ153830.55+085517.0	9.80 ± 1.47	9.76 ± 0.24	47.23 ± 5.67	46.50 ± 5.58	−0.47 ± 0.06
PKS 2126–15 [(a)]	9.78 ± 1.47	–	–	47.11 ± 5.65	0.16 ± 0.02

Notes. [(a)]The C IVλ1549 and the 1900 Å blend regions were not fitted in these cases. [(b)]We compute the weighted averaged mass between the Hβ and Al IIIλ1860 estimates only. [(c)]We compute the weighted averaged mass between the Hβ and C IVλ1549 estimates only.

Coatman et al. 2017; Marziani et al. 2019, hereafter M19). If $M_{\rm BH}$ estimated with the uncorrected VP06 relations are used, there is a significant deviation in the 1:1 relation between Hβ and C IVλ1549 $M_{\rm BH}$ estimates and a large scatter (rms ≈0.42). We therefore utilise the scaling laws based on Al IIIλ1860 and ξ-corrected C IVλ1549 that may provide less biased estimators with respect to Hβ-based $M_{\rm BH}$ scaling law.

Table 13 lists the individual values of Hβ black hole masses (Col. 2), the weighted averages of $M_{\rm BH}$ (Col. 3), the luminosity at 1450 Å and 5100 Å (Cols. 4 and 5, respectively), as well as the Eddington ratio of each source (Col. 6). We have considered the mass estimates using Hβ, Al IIIλ1860, and C IVλ1549 to determine the weighted average of $M_{\rm BH}$ and used the FWHM errors as weights. In addition, Hβ $M_{\rm BH}$ are reported since they are available for all sources of our sample and needed to compare our data to previous samples. We adopted a bolometric correction of 10 for the optical range in accordance with the value assumed in the previous works we consider for comparison (e.g. Richards et al. 2006; S07; S17; M19), although lower bolometric corrections are expected in the $L_{\rm bol} > 10^{47}$ erg s^{-1} luminosity range (Marconi et al. 2004; Netzer 2019), which may introduce a bias towards higher accretion rates. The bolometric correction adopted in the UV range is 3.5 (Elvis et al. 1994).

6.3. Dependence on accretion parameters

6.3.1. [O III]$\lambda\lambda$4959,5007

Figure 15 shows the dependence of W([O III]) and c(9/10) [O III] on $M_{\rm BH,H\beta}$ and $L/L_{\rm Edd}$. Our sample presents W([O III]) < 25 Å in the majority of the cases, with only two outliers (SDSSJ141546.24+112943.4 with ≈34 Å and H 0055−2659 with ≈41 Å). The W([O III]) of our sample is relatively small when compared with low-z sources. However, our data more frequently show blueshifts in c(9/10).

The right panels of Fig. 15 consider only sources that present $c(9/10) < -250$ km s^{-1}. In this case, all the sources fit within W([O III]) $\lesssim$ 25 Å and are found in a wide range of $M_{\rm BH}$ as for the distribution of the full samples. Sources with $c(9/10) < -250$ km s^{-1} have an average Eddington ratio of −0.09: at high Eddington ratios, the [O III]$\lambda\lambda$4959,5007 profiles tend to be strongly affected or dominated by the blueshifted SBC. In addition, the [O III]$\lambda\lambda$4959,5007 W remains roughly constant over a wide range of masses (and luminosity), indicating that the luminosity of the blueshifted SBC is proportional to the continuum luminosity. This result provides evidence that the outflow traced by the blueshifted [O III]$\lambda\lambda$4959,5007 is directly related to the active nucleus, as proportionality between line and continuum luminosity is a classical proof of photoionisation (Osterbrock & Shuder 1982).

6.3.2. C IVλ1549

In Fig. 16, we provide an analysis of the dependence of C IVλ1549 shift measured by c(1/2) on luminosity and $L/L_{\rm Edd}$. We include the data analysed by Marziani et al. (2019), along with the present sample data. The same trend appears to be followed by both ours and Marziani et al. (2019) samples. Sources that present the largest values of C IVλ1549 c(1/2) are Population A, with two xAs (SDSSJ210524.47+000407.3 and SDSSJ210831.56−063022.5), reaching $c(1/2) \approx -5000$ km s^{-1}.

As in S17, the left plot of Fig. 16 indicate a clear relation (with a Pearson correlation coefficient of 0.59) between c(1/2) of C IVλ1549 and $L/L_{\rm Edd}$, given by the following equation for the absolute value of the centroid shift at 1/2:

$$\log |c(1/2)|_{\rm C\,IV} = (0.43 \pm 0.06) \log L/L_{\rm Edd} + (3.25 \pm 0.04). \quad (4)$$

A similar relation can also be derived between the absolute value of C IVλ1549 c(1/2) and $L_{\rm bol}$(1450 Å), (right panel of Fig. 16):

$$\log |c(1/2)|_{\rm C\,IV} = (0.18 \pm 0.03) \log L_{\rm bol} + (-5.70 \pm 1.46). \quad (5)$$

The Pearson correlation coefficient in this case is 0.54. These relations are consistent with those of S17 who found slope ≈0.5 and ≈0.2 for the dependence on Eddington ratio and luminosity, respectively. Since the S17 data were included in the linear regression, we can say that the new data confirm the slope difference that suggests a major role of the $L/L_{\rm Edd}$ for governing the shift amplitude and a secondary effect of luminosity.

6.4. Redefining optical properties of high-z sources

Figure 17 shows the relation between the Eddington ratio and the bolometric luminosity. The distinction between Pop. A and

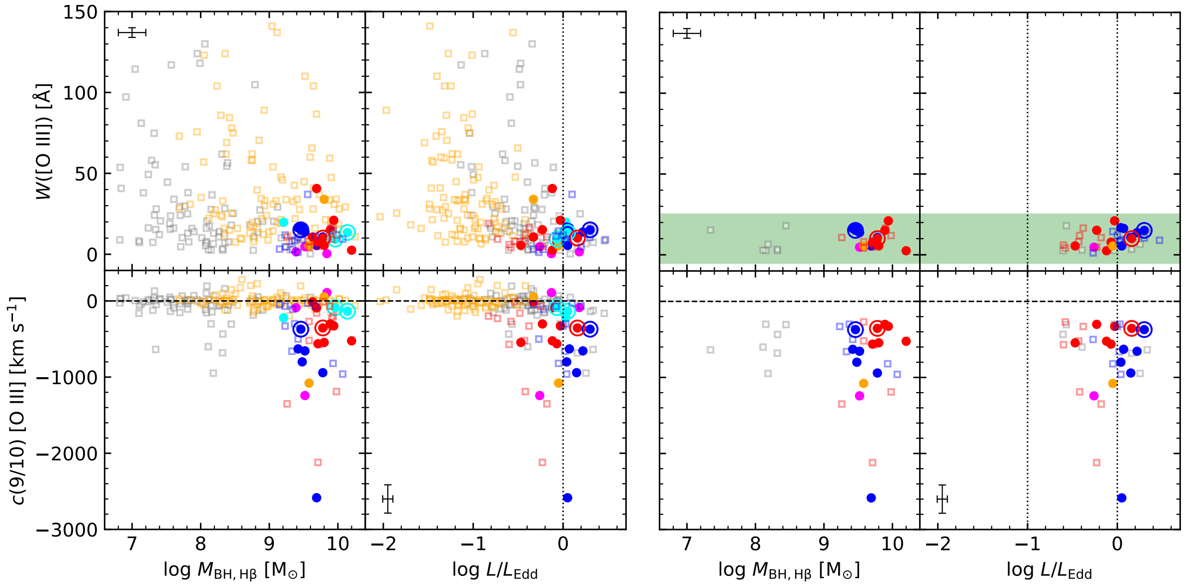

Fig. 15. [O III]$\lambda\lambda$4959,5007 dependence on physical parameters. *Left panel*: our full sample in comparison with the full M03 (grey for Pop. A and orange for Pop. B) and HE (blue for Pop. A and red for Pop. B) samples. *Right panel*: only sources with $c(9/10) < -250$ km s^{-1}. Our data follow the same colour scheme as in Fig. 4.

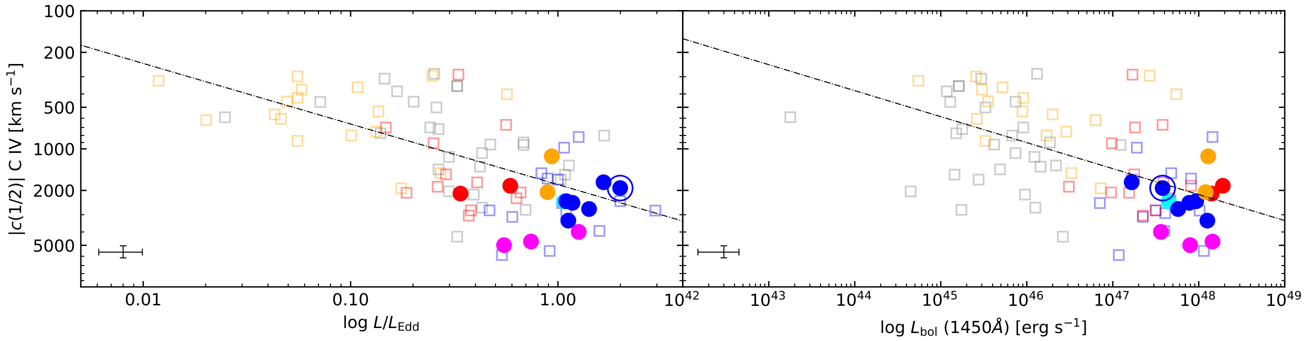

Fig. 16. Dependence of C IV on different parameters. *Left panel*: relation between C IV $c(1/2)$ and $L/L_{\rm Edd}$. *Right panel*: C IV $c(1/2)$ vs. $L_{\rm bol}$ (1450 Å). Grey and orange squares represent low-z Pop. A and Pop. B quasars respectively, while blue and red open squares indicate HE Pop. A and Pop. B sources from S17. Colour scheme is the same as in Fig. 4. Linear regressions are shown by the dashed lines. The errors refer only to our sample.

Pop. B is very clear in both low- and high-redshift samples including our sample as well as the data analysed by S07 and S17. The systematically higher Eddington ratio of the high-luminosity samples may be in part the result of a Malmquist type bias (Sulentic et al. 2014) on the assumption of a constant bolometric correction over a wide range in luminosity, orientation effects, and intrinsic evolution of the Eddington ratio (e.g. Cavaliere & Vittorini 2000; Volonteri et al. 2003; Shankar et al. 2009). For instance, the radio-loud sources from our sample seem to be the more extreme cases of their respective population, reaching $L/L_{\rm Edd} \sim 1$. They are core-dominated and presumably beamed in the direction of the observer. The line profiles appear composite, in the sense that they show a narrower core superimposed on a VBC. The width of the narrower core may be lowered if the emitting regions are constrained within a flattened geometry that is seen pole-on. This effect blurs the distinction between Pop. A and B, letting sources that are intrinsically Pop. B enter into the domain of Pop. A in the MS optical plane (Fig. 3; Marziani et al. 2001; Zamfir et al. 2008).

The right panel of Fig. 17 presents the median values of the Eddington ratio for each individual spectral type, distinguishing between higher ($L > 10^{47}$ erg s^{-1}) and lower ($L < 10^{47}$ erg s^{-1}) luminosity sources (S07; M09; S17, together with our sample). The Eddington ratio is consistently higher in Pop. A sources rather than in Pop. B sources for both cases of luminosity and redshift separation. Low-redshift, low-luminosity sources present very small $L/L_{\rm Edd}$ values for Pop. B. The more extreme case is for low-redshift Pop. B1++, with a $L/L_{\rm Edd} \approx -1.65$. On the converse Pop. A sources have more similar values at low and high luminosity. There is no notable difference between high and low-luminosity and high and low-redshift distribution on the spectral type and log $L/L_{\rm Edd}$ plane, which may indicate that the more luminous sources present the highest Eddington ratios because of a Malmquist-type bias (Sulentic et al. 2014) rather than evolutionary effects on $L/L_{\rm Edd}$.

Of the four quasars that are radio-loud, B1422+231, PKS 1937−101, and PKS 2000−330 are classified as Pop. A, while PKS 2126−15 is a Pop. B source. From four sources we can only make some preliminary considerations that will be properly discussed in a companion paper involving mainly radio-loud objects. The basic result is that the four RLs do not have outstanding properties with respect to the RQ samples considered in this paper. They share the trends between Hβ and [O III]$\lambda\lambda$4959,5007 RQ profile parameters. A remarkable aspect

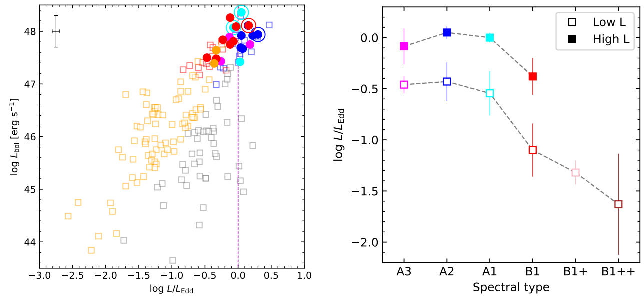

Fig. 17. Distribution of the different spectral types in a luminosity and Eddington ratio ($L/L_{\rm Edd}$) context. *Left plot*: bolometric luminosity $L_{\rm bol}$ vs. $L/L_{\rm Edd}$. Squared symbols identify the samples of S07 (low-z) and of S17 (high-z sources). Vertical purple line indicates $L/L_{\rm Edd}$ = 1. Colour scheme is the same as in Fig. 4. *Right plot*: median values of the Eddington ratio separated into high-luminosity ($\log L > 47$ erg s^{-1}) and low luminosity for each spectral type. We have included our own sources, along with the comparison samples. Error bars indicate the semi-interquartile range.

is that the four RL AGN studied in this paper show high Eddington ratio, a fact that is never observed in powerful RL sources at low-z (Sikora et al. 2007; Zamfir et al. 2008) that are more frequently classified as population B sources. At low-z, low-power, 'jetted' sources for which high Eddington ratio has been estimated to be ~1 are known to exist (the so-called RL NLSy1s; Komossa et al. 2006; Berton et al. 2015; Foschini et al. 2015). Even if $L/L_{\rm Edd}$ might be overestimated, the implication is that there is apparently no empirical inconsistency between powerful jetted emission and high accretion rate.

7. Conclusions

We presented a sample of 22 high-redshift and high-luminosity quasars (12 Pop. A; 10 Pop. B) observed with the VLT/ISAAC spectrograph to cover the Hβ spectral range shifted into the near infrared. A dedicated analysis has been performed on the most prominent emission features in the new optical spectra (Hβ, [O III]$\lambda\lambda$4959,5007, Fe II), as well as in survey or published UV spectra (Al IIIλ1860, C III]λ1909, C IVλ1549, Si IVλ1397, Fe III, Fe IIIλ1914) to measure several parameters related to the emitting gas physical conditions and dynamics. Our main conclusions are as follows.

1. We confirm that the full profile of Hβ may be generally well represented by solely a Lorentzian BC for Pop. A quasars, while two Gaussians (BC and VBC) provide a satisfactory fit for those of Pop. B, with the broader, redshifted VBC accounting for ≈50% of the emission line. Also, some Pop. A Hβ profiles from our sample present outflowing components that seem to be related to those observed in the [O III]$\lambda\lambda$4959,5007 lines.
2. Compared to low-z and low-luminosity samples, our data presents a displacement in the MS in the direction of higher values of FWHM of the Hβ full profile and $R_{\rm Fe\,II}$. The relation between profile parameters and the $M_{\rm BH}$ and $L/L_{\rm Edd}$ differences between Pop. A and B are also confirmed, in the form seen in previous high-luminosity samples.
3. The [O III]$\lambda\lambda$4959,5007 profile is broad and not reproducible with a simple Gaussian. All [O III]$\lambda\lambda$4959,5007 profiles of our sample are blueshifted by more than 250 km s^{-1}. Differently from the low z range, high-z Pop. B [O III]$\lambda\lambda$4959,5007 profiles present significant contribution of blueshifted semi-broad components, even though they are still less strong than the ones found in Pop. A sources. Nevertheless, both population seem to share similar asymmetry indexes, which indicates that their profiles present comparable shapes.
4. In some cases, the [O III]$\lambda\lambda$4959,5007 FWHM reach values comparable to those of Hβ. This effect is found, in particular, for sources with high $L/L_{\rm Edd}$, and may be compared with the case of highly-accreting NLSy1s at low z. Line widths appear extraordinarily large (thousands km s^{-1}) because of the high black hole mass values involved. [O III]$\lambda\lambda$4959,5007 correlations between FWHM and shift, and also between W and shift mirror the correlations seen in C IVλ1549.
5. The [O III]$\lambda\lambda$4959,5007 lines should be avoided for accurate redshift estimates in high-L, high-z quasars, as in most of sources the [O III] lines are dominated by a blueshifted SBC and no rest-frame narrow component could be clearly identified. The average shift of the [O III] profile peak is ~−520 km s^{-1}, which may lead to a considerable systematic blueshift of $\delta z \sim 0.0017$ on the redshift estimation.
6. Several C IVλ1549 correlations (most notably the one between shift and width) and the C IVλ1549 parameters' dependence on Eddington ratio and mass (or luminosity) are confirmed (including the ones of S17). Outflow-dominated profiles tend to have low-W, large FWHM, and shifts. The three parameters are definitely related.
7. We exploit the VP06 scaling law as reference for $M_{\rm BH}$ estimates, and we verified that the scaling law based on Al IIIλ1860 is a reliable estimator with respect to black hole masses derived from Hβ. The C IVλ1549 scaling law requires a FWHM correction.
8. [O III]$\lambda\lambda$4959,5007 and C IVλ1549 seem to follow a very similar, strong correlation between FWHM and shift, as measured by the $c(1/2)$. The [O III]$\lambda\lambda$4959,5007 and C IVλ1549 outflow velocities are related, as suggested by the correlation between their shift amplitudes shown in Fig. 10.
9. The radio loud sources in the high-z range seem to be radiating at high values of Eddington ratio (with $L/L_{\rm Edd} \sim 1$), which is at variance with low-z values, where the most powerful jetted sources belong to Pop. B and radiate at a modest Eddington ratio.

The sample studied in this paper is the first part of a sample involving roughly an equal number of RQ and of RI and RL sources. The data in this paper provide a RQ comparison sample for the ISAAC spectra of RL sources that will be presented in a future paper.

Acknowledgements. The authors thank the anonymous referee for her/his valuable suggestions that helped us to significantly improve the present paper. A.D.M. acknowledges the support of the INPhINIT fellowship from "la Caixa" Foundation (ID 100010434). The fellowship code is LCF/BQ/DI19/11730018. A.D.M., A.d.O., and J.P. acknowledge financial support from the Spanish State Agency MCIN/AEI/10.13039/501100011033 through research grants PID2019-106027GB-C41 and PID2019-106027GB-C43 and the Centre of Excellence Severo Ochoa award to the Instituto de Astrofísica de Andalucía under contract SEV-2017-0709. P.M. acknowledges the support of the IAA-CSIC for a visit in November 2021. A.D.M. is thankful for the kind hospitality at the Padova Astronomical Observatory. This research has made use of the NASA/IPAC Extragalactic Database (NED) which is operated by the Jet Propulsion Laboratory, California Institute of Technology, under contract with the National Aeronautics and Space Administration. Funding for the Sloan Digital Sky Survey IV has been provided by the Alfred P. Sloan Foundation, the US Department of Energy Office of Science, and the Participating Institutions. SDSS-IV acknowledges support and resources from the Center for High Performance Computing at the University of Utah. The SDSS website is www.sdss.org. SDSS-IV is managed by the Astrophysical Research Consortium for the Participating Institutions of the SDSS Collaboration including the Brazilian Participation Group, the Carnegie Institution for Science, Carnegie Mellon University, Center for Astrophysics | Harvard & Smithsonian, the Chilean Participation Group, the

French Participation Group, Instituto de Astrofísica de Canarias, The Johns Hopkins University, Kavli Institute for the Physics and Mathematics of the Universe (IPMU)/University of Tokyo, the Korean Participation Group, Lawrence Berkeley National Laboratory, Leibniz Institut für Astrophysik Potsdam (AIP), Max-Planck-Institut für Astronomie (MPIA Heidelberg), Max-Planck-Institut für Astrophysik (MPA Garching), Max-Planck-Institut für Extraterrestrische Physik (MPE), National Astronomical Observatories of China, New Mexico State University, New York University, University of Notre Dame, Observatário Nacional/MCTI, The Ohio State University, Pennsylvania State University, Shanghai Astronomical Observatory, United Kingdom Participation Group, Universidad Nacional Autónoma de México, University of Arizona, University of Colorado Boulder, University of Oxford, University of Portsmouth, University of Utah, University of Virginia, University of Washington, University of Wisconsin, Vanderbilt University, and Yale University.

References

Adelman-McCarthy, J. K., Agüeros, M. A., Allam, S. S., et al. 2007, ApJS, 172, 634
Ahumada, R., Prieto, C. A., Almeida, A., et al. 2020, ApJS, 249, 3
Allen, J. T., Hewett, P. C., Maddox, N., Richards, G. T., & Belokurov, V. 2011, MNRAS, 410, 860
Assef, R. J., Denney, K. D., Kochanek, C. S., et al. 2011, ApJ, 742, 93
Axon, D. J., Capetti, A., Fanti, R., et al. 2000, AJ, 120, 2284
Bachev, R., Marziani, P., Sulentic, J. W., et al. 2004, ApJ, 617, 171
Barthel, P. D., Tytler, D. R., & Thomson, B. 1990, A&AS, 82, 339
Becker, R. H., White, R. L., & Helfand, D. J. 1995, ApJ, 450, 559
Bennert, N., Falcke, H., Schulz, H., Wilson, A. S., & Wills, B. J. 2002, ApJ, 574, L105
Bennert, N., Jungwiert, B., Komossa, S., Haas, M., & Chini, R. 2006, A&A, 459, 55
Berton, M., & Järvelä, E. 2021, Universe, 7, 188
Berton, M., Foschini, L., Ciroi, S., et al. 2015, A&A, 578, A28
Best, P. N., & Heckman, T. M. 2012, MNRAS, 421, 1569
Bicknell, G. V. 2002, New Astron. Rev., 46, 365
Bischetti, M., Piconcelli, E., Vietri, G., et al. 2017, A&A, 598, A122
Bisogni, S., Marconi, A., & Risaliti, G. 2017, MNRAS, 464, 385
Boller, T., Brandt, W. N., & Fink, H. 1996, A&A, 305, 53
Boroson, T. A. 2002, ApJ, 565, 78
Boroson, T. A., & Green, R. F. 1992, ApJS, 80, 109
Brinkmann, W., & Siebert, J. 1995, A&A, 300, L33
Brotherton, M. S., Runnoe, J. C., Shang, Z., & DiPompeo, M. A. 2015, MNRAS, 451, 1290
Bruni, G., Piconcelli, E., Misawa, T., et al. 2019, A&A, 630, A111
Brusa, M., Bongiorno, A., Cresci, G., et al. 2015, MNRAS, 446, 2394
Buendia-Rios, T. M., Negrete, C. A., Marziani, P., & Dultzin, D. 2022, A&A, accepted [arXiv:2209.05526]
Cano-Díaz, M., Maiolino, R., Marconi, A., et al. 2012, A&A, 537, L8
Capellupo, D. M., Netzer, H., Lira, P., Trakhtenbrot, B., & Mejía-Restrepo, J. 2015, MNRAS, 446, 3427
Capetti, A., Axon, D. J., Macchetto, F., Sparks, W. B., & Boksenberg, A. 1996, ApJ, 469, 554
Carniani, S., Marconi, A., Maiolino, R., et al. 2015, A&A, 580, A102
Cavaliere, A., & Vittorini, V. 2000, ApJ, 543, 599
Coatman, L., Hewett, P. C., Banerji, M., & Richards, G. T. 2016, MNRAS, 461, 647
Coatman, L., Hewett, P. C., Banerji, M., et al. 2017, MNRAS, 465, 2120
Coatman, L., Hewett, P. C., Banerji, M., et al. 2019, MNRAS, 486, 5335
Collin, S., Kawaguchi, T., Peterson, B. M., & Vestergaard, M. 2006, A&A, 456, 75
Collin-Souffrin, S., & Lasota, J.-P. 1988, PASP, 100, 1041
Condon, J. J., Cotton, W. D., Greisen, E. W., et al. 1998, AJ, 115, 1693
Cracco, V., Ciroi, S., Berton, M., et al. 2016, MNRAS, 462, 1256
Cresci, G., Marconi, A., Zibetti, S., et al. 2015, A&A, 582, A63
Dadina, M., Vignali, C., Cappi, M., et al. 2016, A&A, 592, A104
Deconto-Machado, A., del Olmo, A., Marziani, P., Perea, J., & Stirpe, G. 2022, Astron. Nachr., 343, e210084
del Olmo, A., Marziani, P., Ganci, V., et al. 2021, Proc. Int. Astron. Union, 356, 310
Diana, A., Caccianiga, A., Ighina, L., et al. 2022, MNRAS, 511, 5436
Dimitrijević, M. S., Kovačević, J., Popović, L. C., Dačić, M., & Ilić, D. 2007, AIP Conf. Proc., 895, 313
Dix, C., Shemmer, O., Brotherton, M. S., et al. 2020, ApJ, 893, 14
Du, P., Wang, J.-M., Hu, C., et al. 2016, ApJ, 818, L14
Elvis, M., Wilkes, B. J., McDowell, J. C., et al. 1994, ApJS, 95, 1
Ferland, G. J., Hu, C., Wang, J.-M., et al. 2009, ApJ, 707, L82
Fine, S., Croom, S. M., Bland-Hawthorn, J., et al. 2010, MNRAS, 409, 591
Fiore, F., Feruglio, C., Shankar, F., et al. 2017, A&A, 601, A143
Foschini, L., Berton, M., Caccianiga, A., et al. 2015, A&A, 575, A13
Fraix-Burnet, D., Marziani, P., D'Onofrio, M., & Dultzin, D. 2017, Front. Astron. Space Sci., 4, 1
Ganci, V., Marziani, P., D'Onofrio, M., et al. 2019, A&A, 630, A110
Gaskell, C. M., & Harrington, P. Z. 2018, MNRAS, 478, 1660
Gibson, R. R., Jiang, L., Brandt, W. N., et al. 2009, ApJ, 692, 758
Gregg, M. D., Becker, R. H., White, R. L., et al. 1996, AJ, 112, 407
Hazard, C., Morton, D. C., Terlevich, R., & McMahon, R. 1984, ApJ, 282, 33
Jarvis, M. E., Harrison, C. M., Thomson, A. P., et al. 2019, MNRAS, 485, 2710
Jaunsen, A. O., Jablonski, M., Pettersen, B. R., & Stabell, R. 1995, A&A, 300, 323
Kauffmann, G., Heckman, T. M., & Best, P. N. 2008, MNRAS, 384, 953
Kellermann, K. I., Sramek, R., Schmidt, M., Shaffer, D. B., & Green, R. 1989, AJ, 98, 1195
Kollatschny, W., & Zetzl, M. 2011, Nature, 470, 366
Komossa, S., Voges, W., Xu, D., et al. 2006, AJ, 132, 531
Komossa, S., Xu, D., Zhou, H., Storchi-Bergmann, T., & Binette, L. 2008, ApJ, 680, 926
Komossa, S., Xu, D. W., & Wagner, A. Y. 2018, MNRAS, 477, 5115
Kriss, G. 1994, ASP Conf. Ser., 61, 437
Kundic, T., Hogg, D. W., Blandford, R. D., et al. 1997, AJ, 114, 2276
Lawrence, C. R., Neugebauer, G., Weir, N., Matthews, K., & Patnaik, A. R. 1992, MNRAS, 259, 5P
Lee, S.-S., Lobanov, A. P., Krichbaum, T. P., & Zensus, J. A. 2016, ApJ, 826, 135
Lyke, B. W., Higley, A. N., McLane, J. N., et al. 2020, ApJS, 250, 8
Marconi, A., Risaliti, G., Gilli, R., et al. 2004, MNRAS, 351, 169
Marinello, M., Overzier, R. A., Röttgering, H. J. A., et al. 2020, MNRAS, 492, 1991
Martínez-Aldama, M. L., del Olmo, A., Marziani, P., et al. 2018, A&A, 618, A179
Marziani, P., Sulentic, J. W., Dultzin-Hacyan, D., Calvani, M., & Moles, M. 1996, ApJS, 104, 37
Marziani, P., Sulentic, J. W., Zwitter, T., Dultzin-Hacyan, D., & Calvani, M. 2001, ApJ, 558, 553
Marziani, P., Sulentic, J. W., Zamanov, R., et al. 2003, ApJS, 145, 199
Marziani, P., Sulentic, J. W., Stirpe, G. M., Zamfir, S., & Calvani, M. 2009, A&A, 495, 83
Marziani, P., Sulentic, J. W., Negrete, C. A., et al. 2010, MNRAS, 409, 1033
Marziani, P., Sulentic, J. W., Plauchu-Frayn, I., & del Olmo, A. 2013, A&A, 555, A89
Marziani, P., Sulentic, J. W., Stirpe, G. M., et al. 2016a, Ap&SS, 361, 3
Marziani, P., Martínez Carballo, M. A., Sulentic, J. W., et al. 2016b, Ap&SS, 361, 29
Marziani, P., Negrete, C. A., Dultzin, D., et al. 2017a, Front. Astron. Space Sci., 4, 16
Marziani, P., Olmo, A., Martínez-Aldama, M., et al. 2017b, Atoms, 5, 33
Marziani, P., Dultzin, D., Sulentic, J. W., et al. 2018, Front. Astron. Space Sci., 5, 6
Marziani, P., del Olmo, A., Martínez-Carballo, M. A., et al. 2019, A&A, 627, A88
Marziani, P., Deconto-Machado, A., & Del Olmo, A. 2022a, Galaxies, 10, 54
Marziani, P., Olmo, A. D., Negrete, C. A., et al. 2022b, ApJS, 261, 30
Marziani, P., Bon, E., Bon, N., et al. 2022c, Astron. Nachr., 343, e210082
Matthews, B. M., Shemmer, O., Dix, C., et al. 2021, ApJS, 252, 15
Mauch, T., Murphy, T., Buttery, H. J., et al. 2003, MNRAS, 342, 1117
McIntosh, D. H., Rix, H. W., Rieke, M. J., & Foltz, C. B. 1999, ApJ, 517, L73
McLure, R. J., & Dunlop, J. S. 2004, MNRAS, 352, 1390
McLure, R. J., & Jarvis, M. J. 2002, MNRAS, 337, 109
Mejía-Restrepo, J. E., Trakhtenbrot, B., Lira, P., Netzer, H., & Capellupo, D. M. 2016, MNRAS, 460, 187
Negrete, C. A., Dultzin, D., Marziani, P., et al. 2018, A&A, 620, A118
Netzer, H. 2019, MNRAS, 488, 5185
Netzer, H., Shemmer, O., Maiolino, R., et al. 2004, ApJ, 614, 558
O'Dowd, M., Bate, N. F., Webster, R. L., et al. 2017, MNRAS, accepted [arXiv:1708.07535]
Osterbrock, D. E., & Shuder, J. M. 1982, ApJS, 49, 149
Panda, S., Marziani, P., & Czerny, B. 2019, ApJ, 882, 79
Panda, S., Martínez-Aldama, M. L., Marinello, M., et al. 2020, ApJ, 902, 76
Patnaik, A. R., Browne, I. W. A., Walsh, D., Chaffee, F. H., & Foltz, C. B. 1992, MNRAS, 259, 1P
Peterson, B. M., & Ferland, G. J. 1986, Nature, 324, 345
Punsly, B. 2010, ApJ, 713, 232
Punsly, B., Marziani, P., Berton, M., & Kharb, P. 2020, ApJ, 903, 44
Rankine, A. L., Hewett, P. C., Banerji, M., & Richards, G. T. 2020, MNRAS, 492, 4553
Reynaldi, V., & Feinstein, C. 2013, MNRAS, 430, 2221

Richards, G. T., Strauss, M. A., Fan, X., et al. 2006, AJ, 131, 2766
Richards, G. T., Kruczek, N. E., Gallagher, S. C., et al. 2011, AJ, 141, 167
Rokaki, E., Lawrence, A., Economou, F., & Mastichiadis, A. 2003, MNRAS, 340, 1298
Savage, A., Jauncey, D. L., White, G. L., et al. 1990, Aust. J. Phys., 43, 241
Scaringi, S., Cottis, C. E., Knigge, C., & Goad, M. R. 2009, MNRAS, 399, 2231
Schmidt, M., & Green, R. F. 1983, ApJ, 269, 352
Shankar, F., Weinberg, D. H., & Miralda-Escudé, J. 2009, ApJ, 690, 20
Shen, Y. 2013, Bull. Astron. Soc. India, 41, 61
Shen, Y., & Ho, L. C. 2014, Nature, 513, 210
Shen, Y., Richards, G. T., Strauss, M. A., et al. 2011, ApJS, 194, 45
Sigut, T. A. A., & Pradhan, A. K. 1998, ApJ, 499, L139
Sigut, T. A. A., Pradhan, A. K., & Nahar, S. N. 2004, ApJ, 611, 81
Sikora, M., Stawarz, Ł., & Lasota, J.-P. 2007, ApJ, 658, 815
Singh, K. P., Garmire, G. P., & Nousek, J. 1985, ApJ, 297, 633
Sluse, D., Hutsemékers, D., Courbin, F., Meylan, G., & Wambsganss, J. 2012, A&A, 544, A62
Small, T. A., & Blandford, R. D. 1992, MNRAS, 259, 725
Snedden, S. A., & Gaskell, C. M. 2007, ApJ, 669, 126
Śniegowska, M., Kozłowski, S., Czerny, B., Panda, S., & Hryniewicz, K. 2020, ApJ, 900, 64
Śniegowska, M., Marziani, P., Czerny, B., et al. 2021, ApJ, 910, 115
Storchi-Bergmann, T., de Oliveira, B. D., Micchi, L. F. L., et al. 2018, ApJ, 868, 14
Sulentic, J. W., Marziani, P., & Dultzin-Hacyan, D. 2000a, ARA&A, 38, 521
Sulentic, J. W., Zwitter, T., Marziani, P., & Dultzin-Hacyan, D. 2000b, ApJ, 536, L5
Sulentic, J. W., Marziani, P., Zamanov, R., et al. 2002, ApJ, 566, L71
Sulentic, J. W., Zamfir, S., Marziani, P., et al. 2003, ApJ, 597, L17
Sulentic, J. W., Stirpe, G. M., Marziani, P., et al. 2004, A&A, 423, 121
Sulentic, J. W., Repetto, P., Stirpe, G. M., et al. 2006a, A&A, 456, 929
Sulentic, J. W., Dultzin-Hacyan, D., Marziani, P., et al. 2006b, Rev. Mex. Astron. Astrofis., 42, 23
Sulentic, J. W., Bachev, R., Marziani, P., Negrete, C. A., & Dultzin, D. 2007, ApJ, 666, 757
Sulentic, J. W., Marziani, P., del Olmo, A., et al. 2014, A&A, 570, A96
Sulentic, J. W., del Olmo, A., Marziani, P., et al. 2017, A&A, 608, A122
Sun, J., & Shen, Y. 2015, ApJ, 804, L15
Sun, M., Xue, Y., Richards, G. T., et al. 2018, ApJ, 854, 128
Takahashi, R., & Inoue, K. T. 2014, MNRAS, 440, 870
Tonry, J. L. 1998, AJ, 115, 1
Torrealba, J., Chavushyan, V., Cruz-González, I., et al. 2012, Rev. Mex. Astron. Astrofis., 48, 9
Véron-Cetty, M. P., & Véron, P. 2010, A&A, 518, A10
Vestergaard, M., & Peterson, B. M. 2006, ApJ, 641, 689
Vestergaard, M., & Wilkes, B. J. 2001, ApJS, 134, 1
Vietri, G., Piconcelli, E., Bischetti, M., et al. 2018, A&A, 617, A81
Vietri, G., Mainieri, V., Kakkad, D., et al. 2020, A&A, 644, A175
Villar Martín, M., Perna, M., Humphrey, A., et al. 2020, A&A, 634, A116
Voges, W. 1993, Adv. Space Res., 13, 391
Volonteri, M., Haardt, F., & Madau, P. 2003, ApJ, 582, 559
Walter, R., & Fink, H. H. 1993, A&A, 274, 105
Wang, J., & Li, Y. 2011, ApJ, 742, L12
Wang, T., Brinkmann, W., & Bergeron, J. 1996, A&A, 309, 81
Welling, C. A., Miller, B. P., Brandt, W. N., Capellupo, D. M., & Gibson, R. R. 2014, MNRAS, 440, 2474
Wills, B. J., & Browne, I. W. A. 1986, ApJ, 302, 56
Wisotzki, L., Christlieb, N., Bade, N., et al. 2000, A&A, 358, 77
Wolf, J., Salvato, M., Coffey, D., et al. 2020, MNRAS, 492, 3580
Woo, J.-H., & Urry, C. M. 2002, ApJ, 581, L5
Yi, W., Zuo, W., Yang, J., et al. 2020, ApJ, 893, 95
Yuan, M. J., & Wills, B. J. 2003, ApJ, 593, L11
Zakamska, N. L., Hamann, F., Pâris, I., et al. 2016, MNRAS, 459, 3144
Zamanov, R., Marziani, P., Sulentic, J. W., et al. 2002, ApJ, 576, L9
Zamfir, S., Sulentic, J. W., & Marziani, P. 2008, MNRAS, 387, 856
Zamfir, S., Sulentic, J. W., Marziani, P., & Dultzin, D. 2010, MNRAS, 403, 1759
Zhang, K., Dong, X.-B., Wang, T.-G., & Gaskell, C. M. 2011, ApJ, 737, 71

Appendix A: Multicomponent fits in the optical and UV ranges and individual notes

In this appendix, we present the new VLT/ISAAC infrared spectra and the multicomponent fittings for the optical spectral range, including the fits of Hβ+[O III]$\lambda\lambda$4959,5007. An additional analysis of the UV spectra is also presented for the objects with available UV spectra, from the literature or from SDSS. The UV analysis includes fittings for Si IVλ1397+O IV]λ1402, C IVλ1549+He IIλ1640 as well as for the 1900 Å blend. We also include notes for some of the individual objects.

A.1. HE 0001-2340

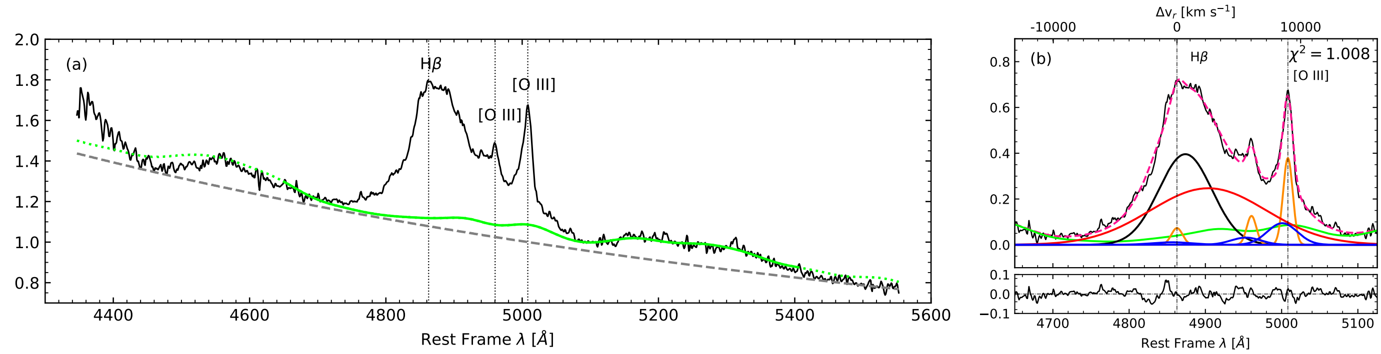

Fig. A.1. HE 0001-2340: *(a)* Rest-frame spectrum covering the Hβ spectral range obtained with VLT/ISAAC. The spectrum is normalised by the continuum at 5100 Å (the flux values are available at Table 4). The grey dashed line traces a power law that defines the continuum level as obtained with the SPECFIT multicomponent analysis. The green line shows the Fe II contribution. For this object Fe II was fitted only with the red Fe II blend due to the presence of atmospheric absorption in the blue. The vertical dotted lines indicate the rest-frame of the main emission lines in the Hβ spectral range and the grey-shaded area indicate the regions that were not considered in the fittings. The white area indicates the region used to anchor both the continuum and the Fe II template. *(b)* Result of the fitting after continuum subtraction (upper panel) and the residuals (bottom panel) for the Hβ region. Pink dashed line shows the final fit. Broad Hβ component (BC) is represented by a black line meanwhile red line show the VBC. Orange lines represent narrow components and the blue ones correspond to the blueshifted components. The region in which the Fe II template was fitted is represented by the solid green line. Dotted green line indicate the expected Fe II contribution for the other parts of the spectra.

A.2. [HB89] 0029+073

Jaunsen et al. (1995) listed this source as a gravitational lens candidate. [HB89] 0029+073 is another case in which the Fe II contribution was measured at $\lambda \geq 5000$ Å and then rescaled to obtain the intensity of the Fe IIλ4570 blend.

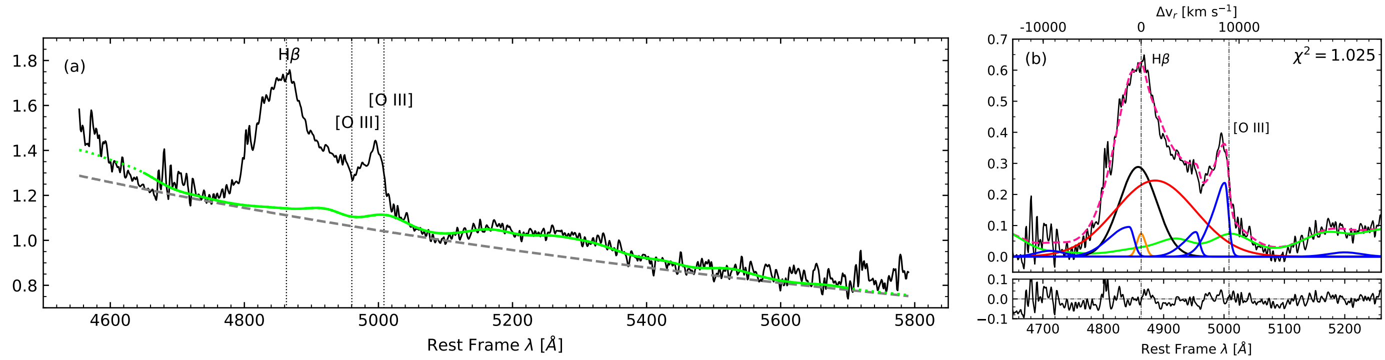

Fig. A.2. [HB89] 0029+073. Colours and lines as Figure A.1.

A.3. CTQ 0408

As in the case of [HB89] 0029+073, the Fe II of CTQ 0408 was fit on the red side of Hβ with $\lambda \geq 5000$ Å. Radio information about this source was found only in the SUMSS catalogue (Mauch et al. 2003). There is no radio map from NVSS nor FIRST for this object, because it is out of the respective survey fields.

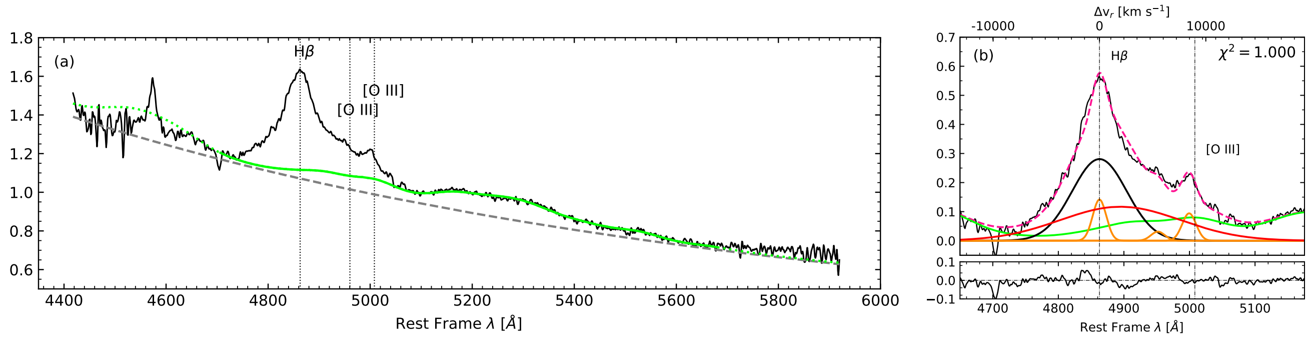

Fig. A.3. CTQ 0408. Details are the same as in Figure A.1.

A.4. SDSSJ005700.18+143737.7

Hβ+[O III]$\lambda\lambda$4959,5007 falls at the red border of the observed spectrum. Consequently, the [O III] measurements should be treated as highly uncertain and special marks have been included in the corresponding tables in the paper. The measurements and the analysis on the [O III] profile were performed with the [O III]λ4959 instead of [O III]λ5007. With respect to the UV spectrum, the object presents strong absorption lines likely associated with intervening absorbers throughout the three UV regions of interest. In the analysis we also included Gaussians profiles for the absorption lines in the fittings. It was necessary to include two blueshifted components for Al IIIλ1860 and Si III]λ1892, otherwise both Al IIIλ1860 and Si III]λ1892 BC are shifted by more than 1000 km s^{-1}.

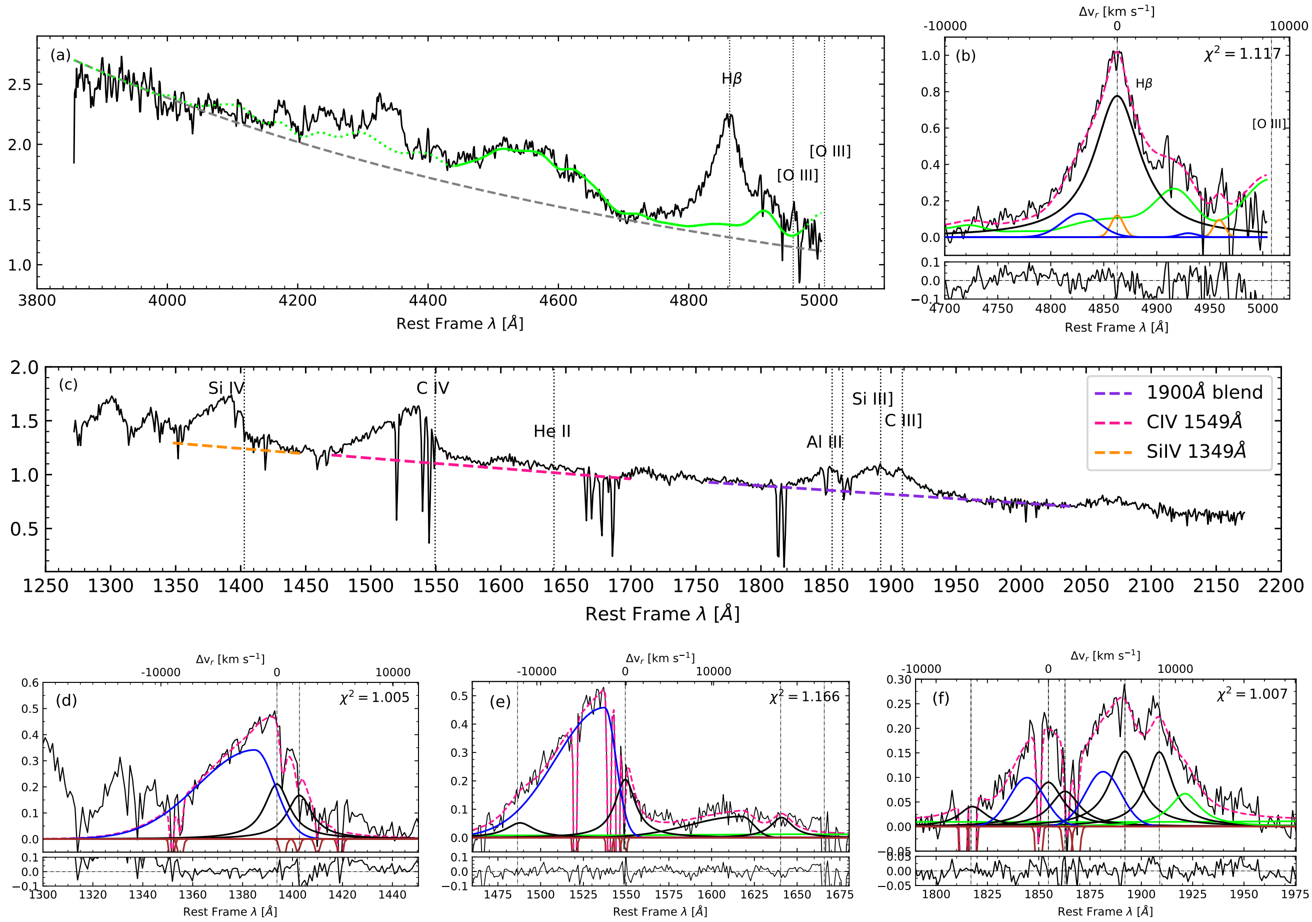

Fig. A.4. SDSSJ005700.18+143737.7. *Top panels:* Details are the same as in Fig. A.1. *(c)* Continuum-normalised UV spectrum from SDSS DR-16 with adopted continuum marked in colour. *Bottom panels:* Fits for (d) Si IVλ1397+O IV]λ1402, (e) C IVλ1549+He IIλ1640, and (f) the 1900 Å blend. Pink dashed lines show the final fitting. Broad components are represented by black lines, while blueshifted components are in blue. Green line represents the additional Fe IIIλ1914 line in the red side of C III], observed in extreme Pop. A sources. Brown lines represent the absorptions seen in the spectrum and modelled as negative-flux Gaussians.

A.5. H 0055-2659

The VLT rest-frame optical spectrum of H 0055-2659 presents a very flat profile and small Fe II multiplets contributions.

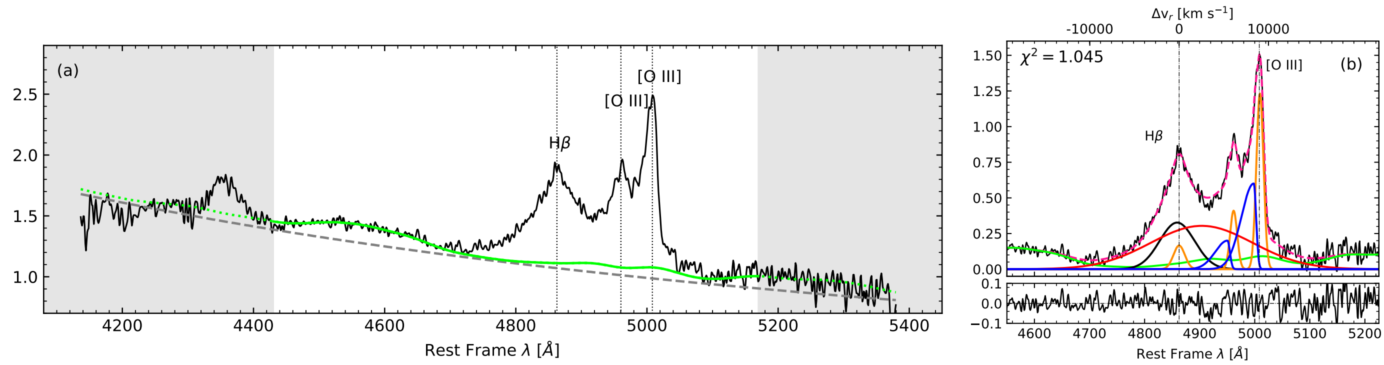

Fig. A.5. H 0055-2659. Details are the same as in Figure A.1.

A.6. SDSSJ114358.52+052444.9

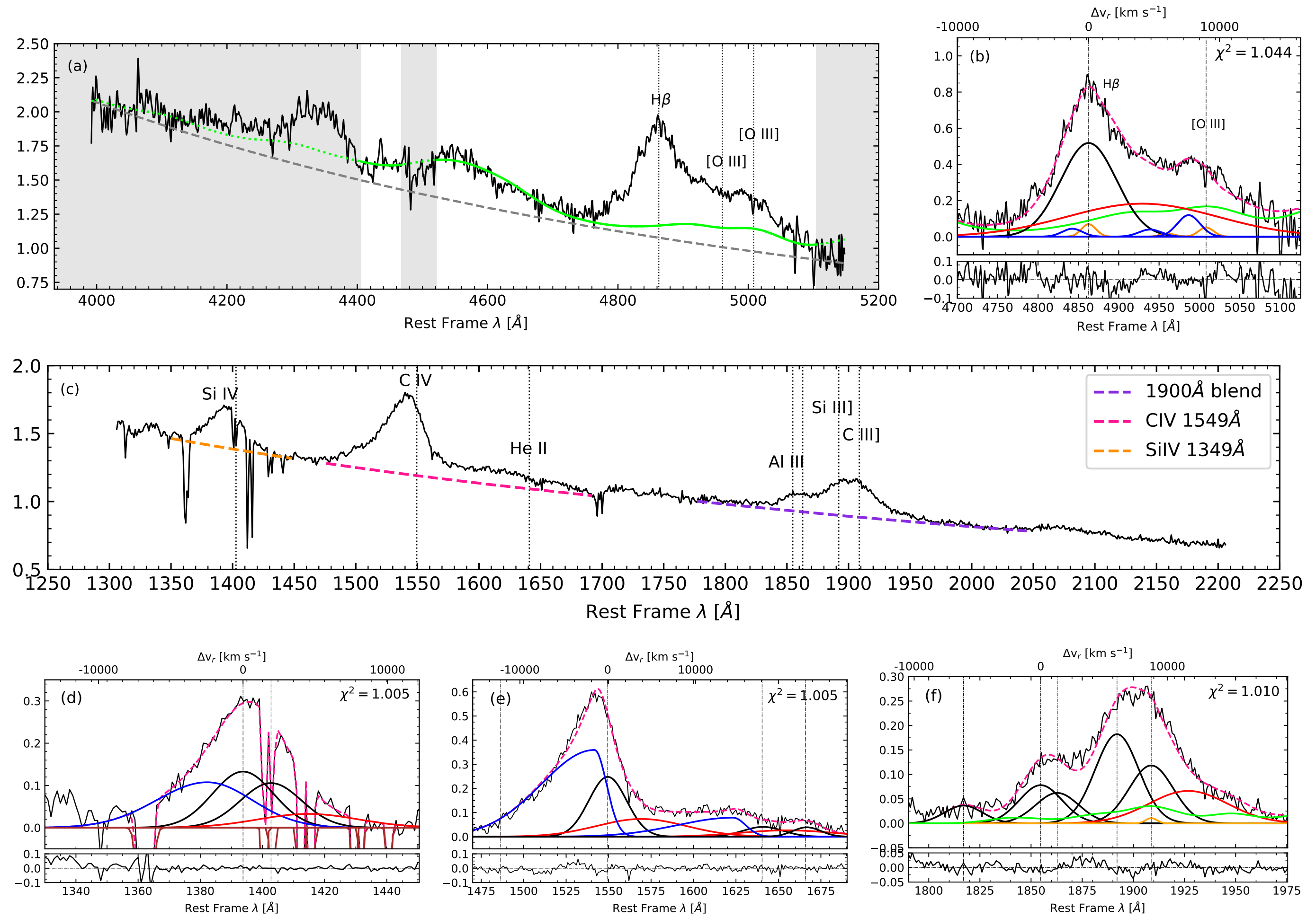

Fig. A.6. SDSSJ114358.52+052444.9. *Top panels:* Details are the same as in Fig. A.1 *Middle and bottom panels:* Same details as in Fig. A.4. Pink dashed lines show the final fitting. Broad components are represented by black lines, while blueshifted components are in blue. Brown lines represent the absorption lines seen in the spectrum.

A.7. SDSSJ115954.33+201921.1

In the optical range, this source presents a very flat spectrum and almost no Fe II contributions.

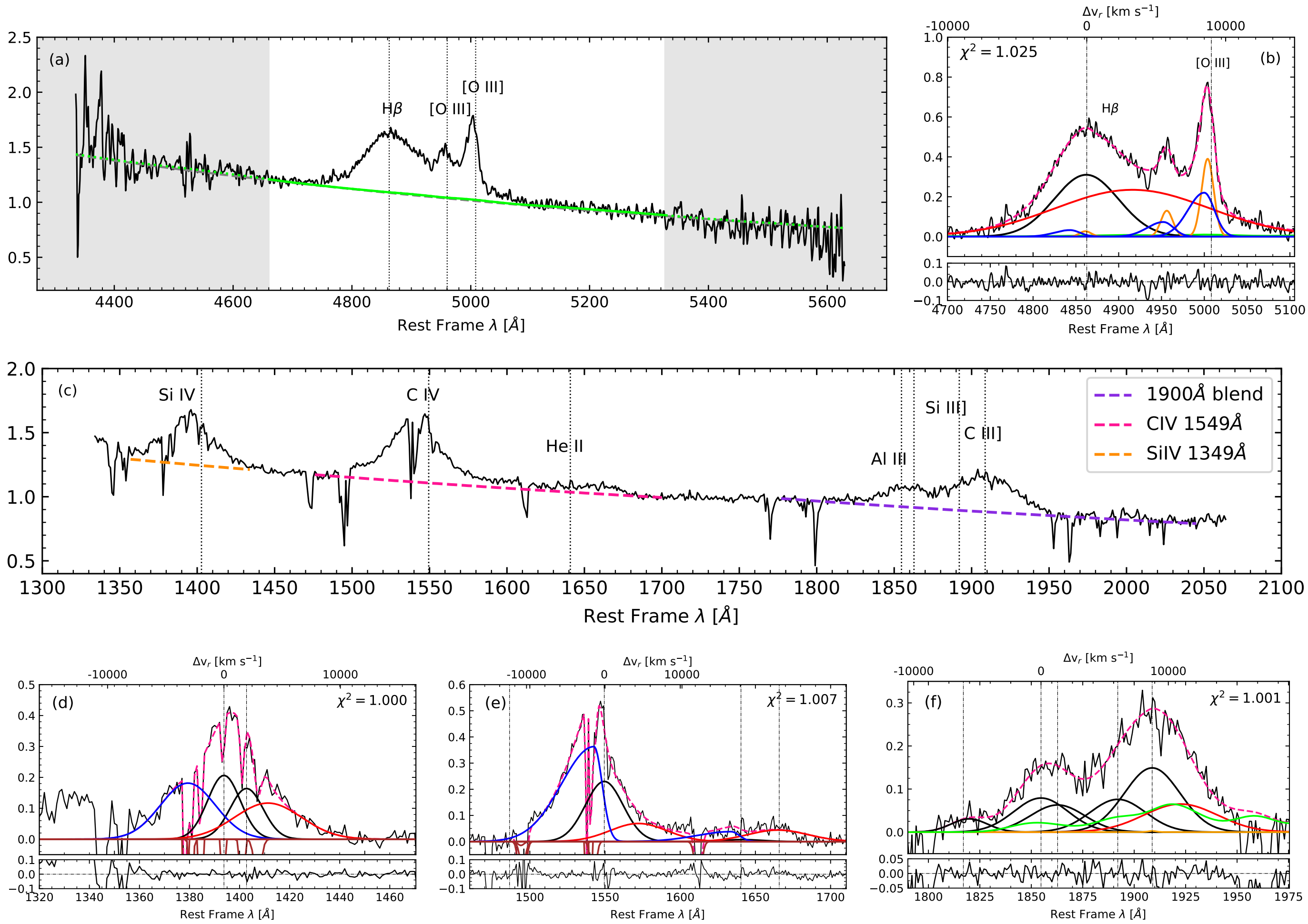

Fig. A.7. SDSSJ115954.33+201921.1. Same details as in Figure A.6.

A.8. SDSSJ120147.90+120630.2

This quasar has observations of the Hβ region at the Large Binocular Telescope (LBT), as reported in Bischetti et al. (2017). We stress that their spectrum is very similar to the one of ISAAC/VLT.

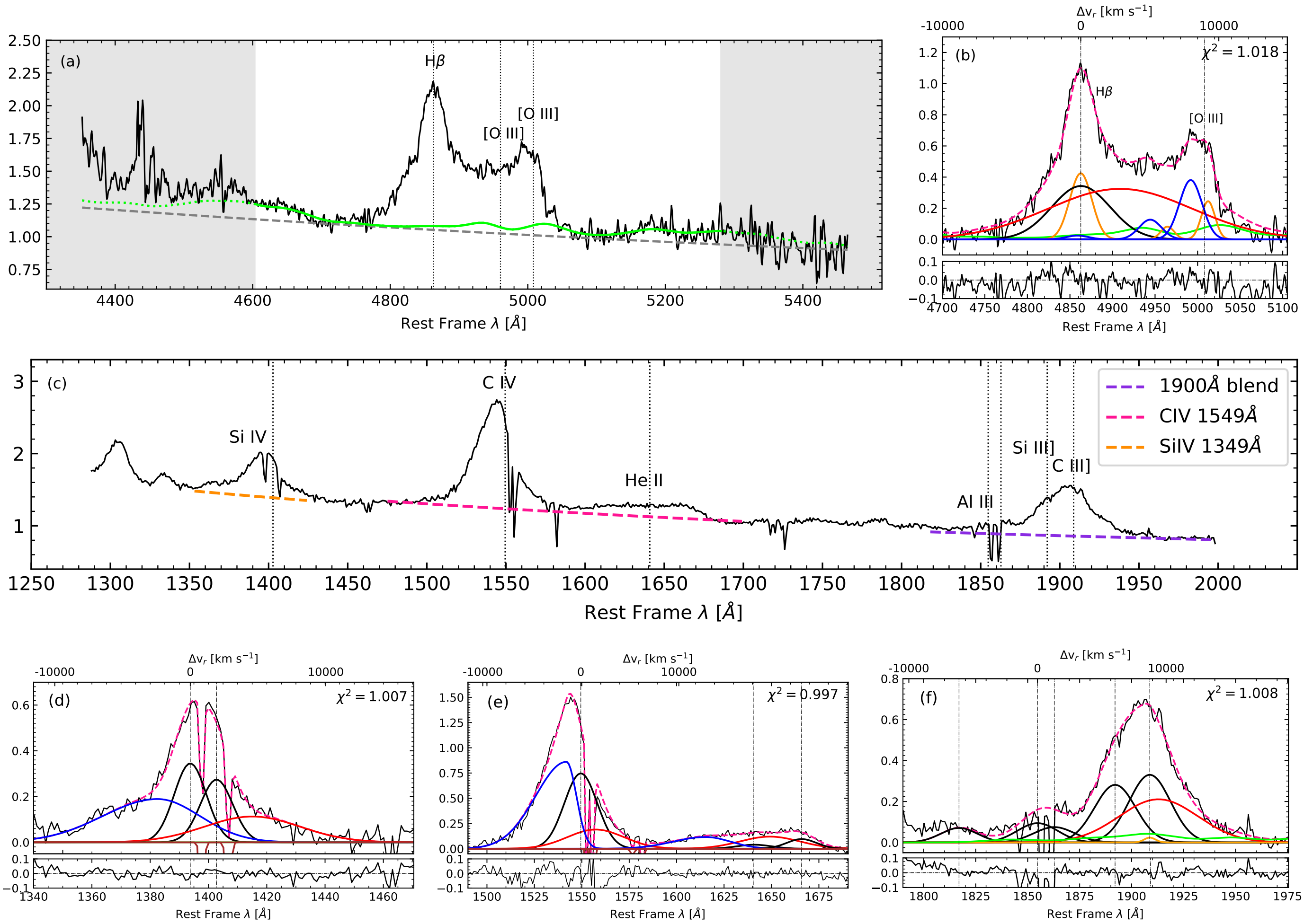

Fig. A.8. SDSSJ120147.90+120630.2. Same details as in Figure A.6.

A.9. SDSSJ132012.33+142037.1

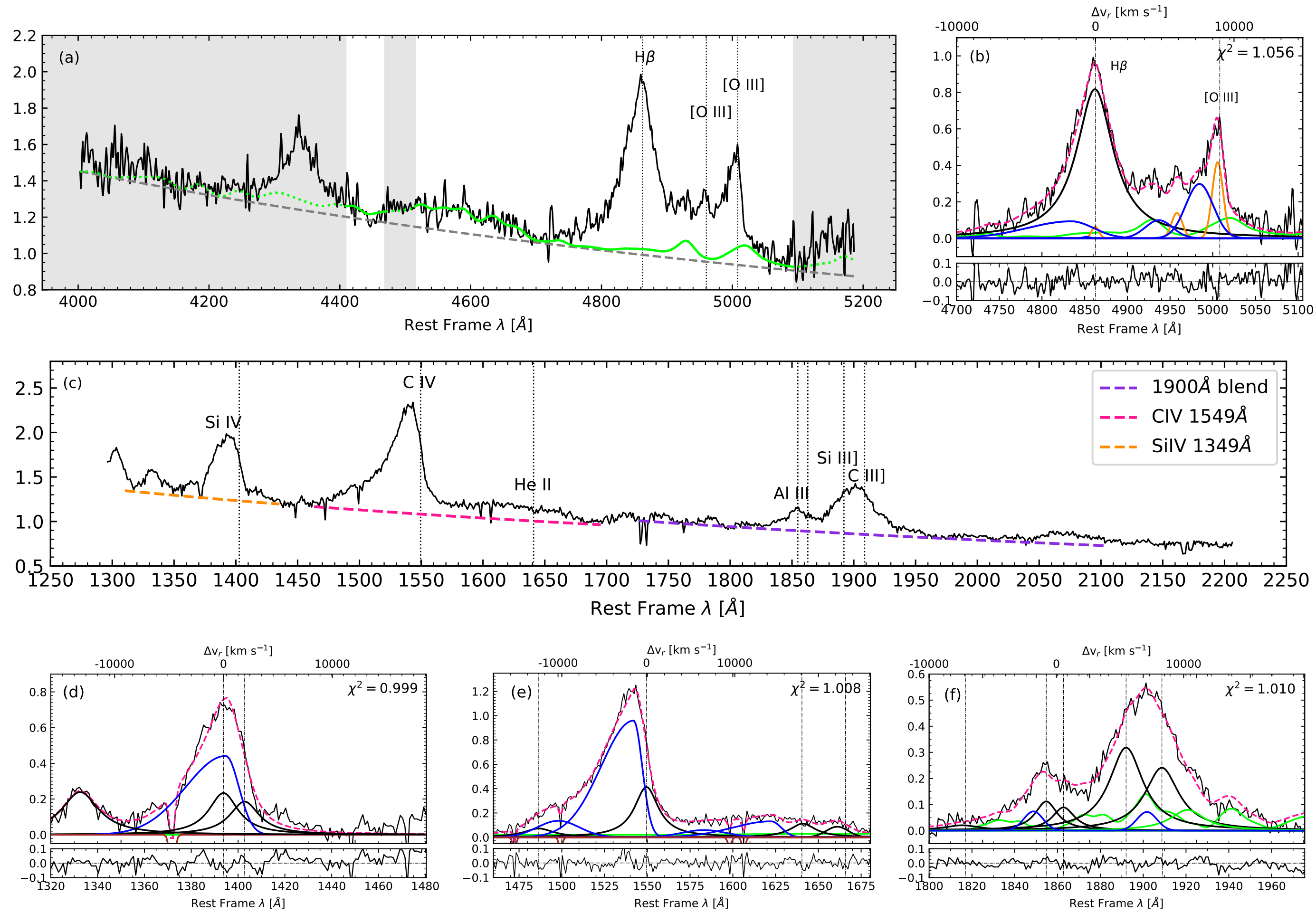

Fig. A.9. SDSSJ132012.33+142037.1. Same details as in Figure A.6.

A.10. SDSSJ135831.78+050522.8

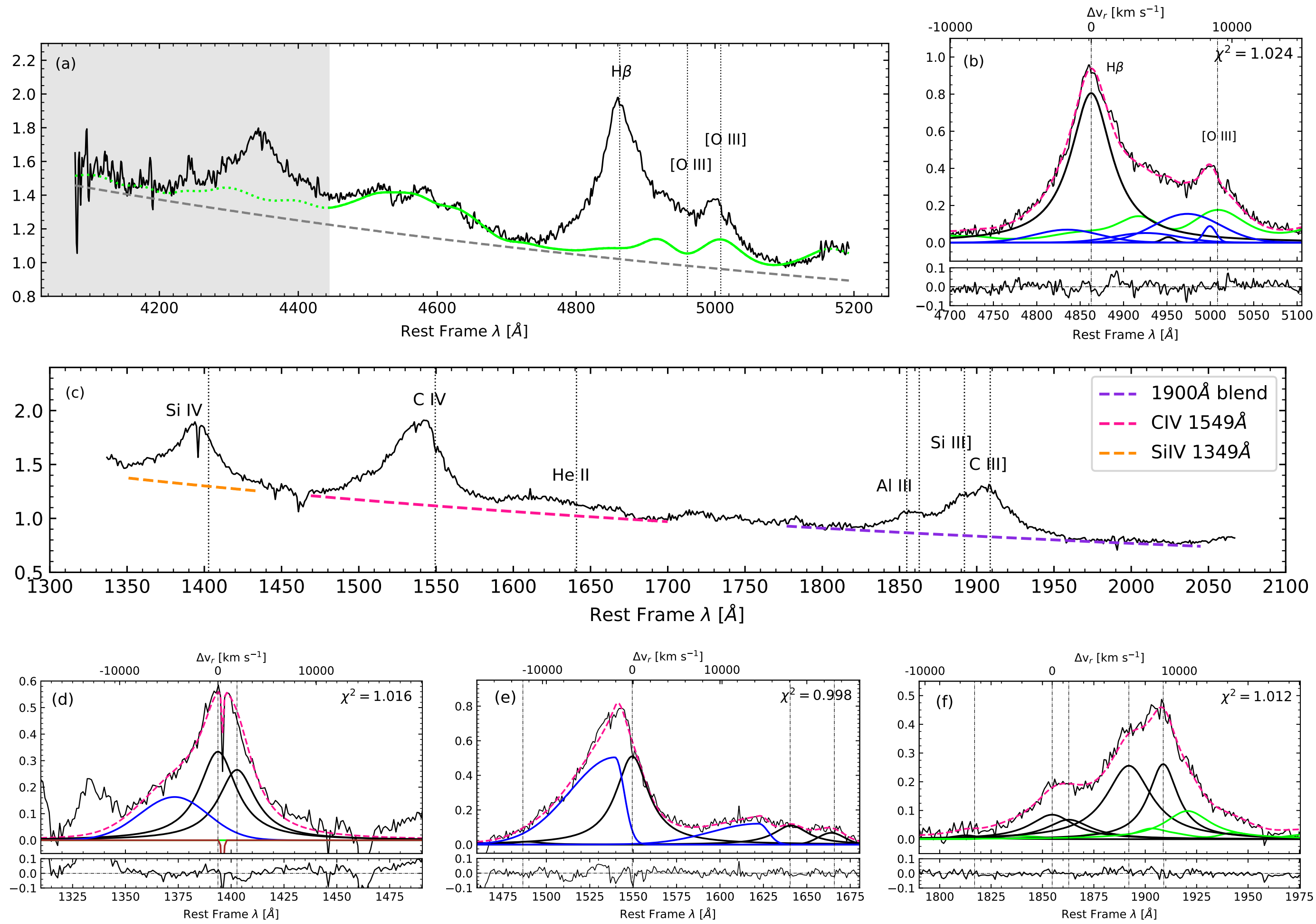

Fig. A.10. SDSSJ135831.78+050522.8. Same details as in Figure A.6.

A.11. Q 1410+096

This source has been identified as a BAL quasar by Allen et al. (2011) and the absorption lines are seen in the regions of the Si IVλ1397 and C IVλ1549 emission lines. In order to account for the multiplet contributions in the optical region, we performed a fitting of this Fe II emission on the red side of Hβ, since the blue part of the FeIIλ4570 region is close to the border of the spectrum and evidently affected by background subtraction or telluric absorption correction.

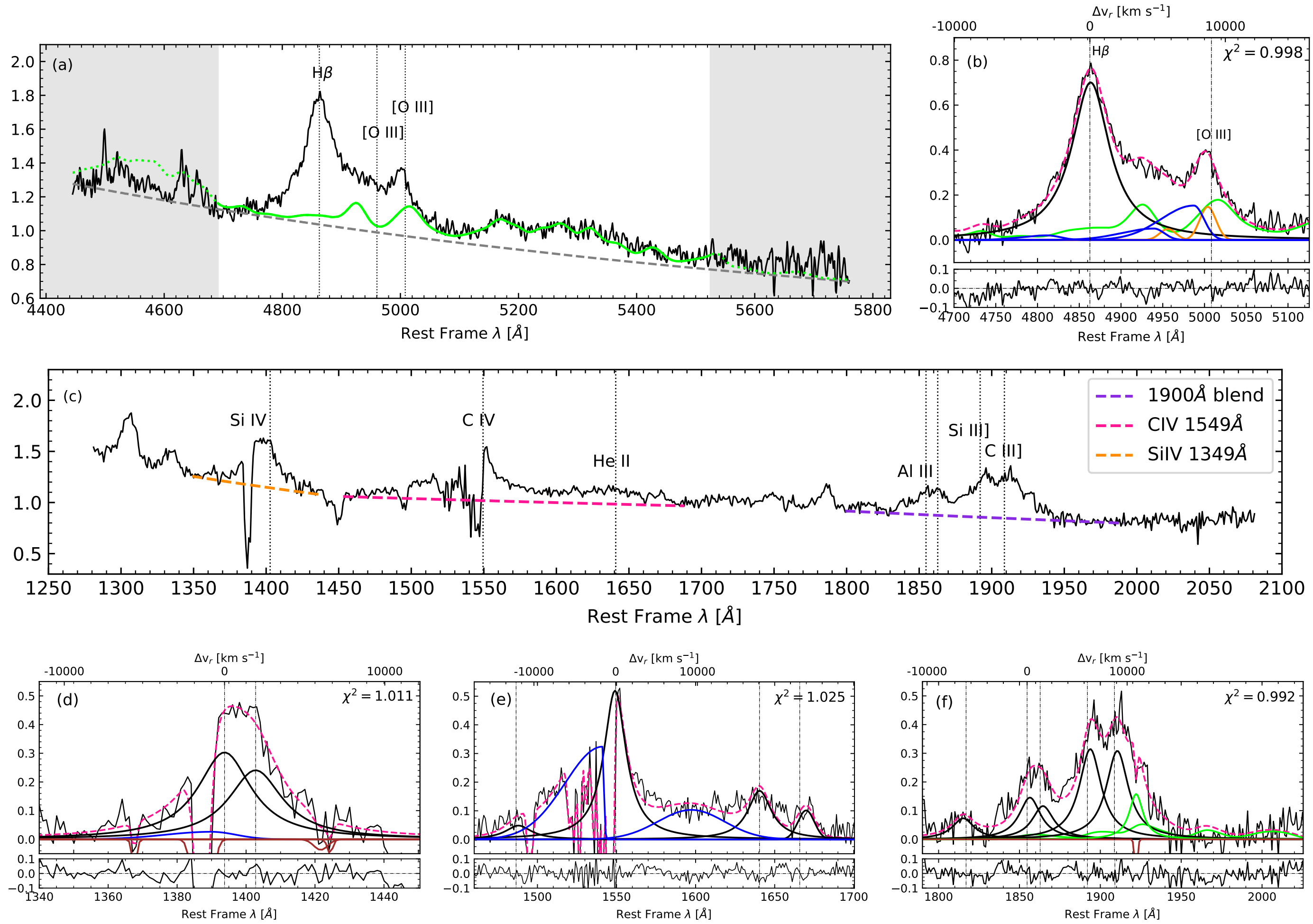

Fig. A.11. Q 1410+096. Same details as in Figure A.6.

For this quasar, we performed the fitting of the C IVλ1549 line based on the He IIλ1640 profile. The Al IIIλ1860 BC of 1410+096 is narrow when compared to Hβ, which may indicate that Hβ might be affected by blueshifted emission. An excess (not included in the fit) is also visible on the blue side of Al IIIλ1860 (bottom rightmost panel of Fig. A.11). This source has also been analysed in detail in Deconto-Machado et al. (2022).

A.12. SDSSJ141546.24+112943.4

This object is known as a weak microlensing candidate in the literature (Sluse et al. 2012; Takahashi & Inoue 2014). According to Welling et al. (2014), the quasar is a gravitationally lensed object split into four images separated by $\sim 1''$. SDSSJ141546.24+112943.4 is a modest core-dominated radio-loud source with a logarithmic radio loudness parameter of 1.09.

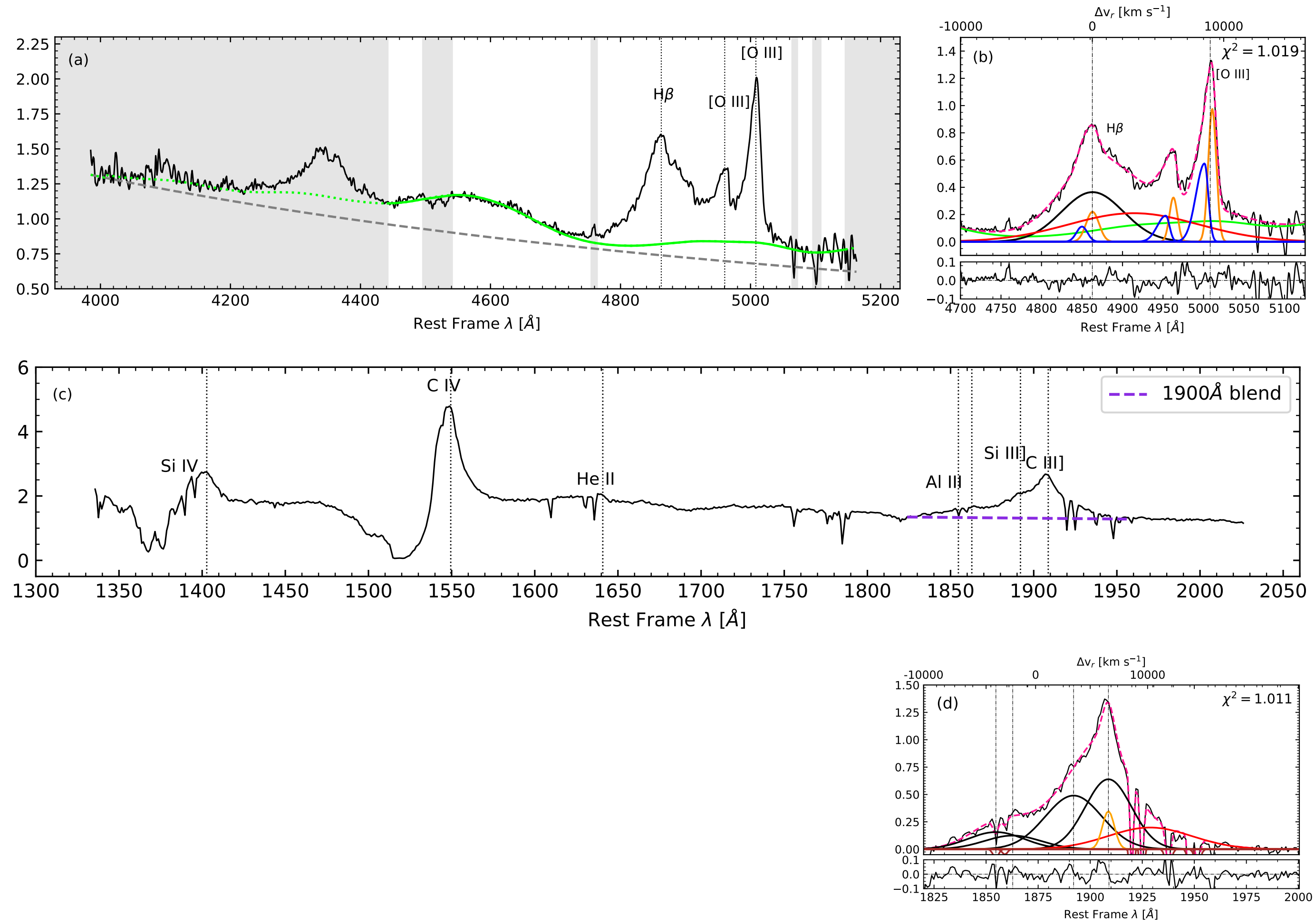

Fig. A.12. SDSSJ141546.24+112943.4. *Top panels:* Colours and lines are the same as in Fig. A.1. *(c)* UV spectrum. *(d)* Fits for the 1900 Å blend. Pink dashed lines show the final fitting. Broad components are represented by black lines, while narrow and very broad components are in orange and red, respectively. Brown lines represent the absorption seen in the spectrum.

As can be seen in the UV spectra presented in Fig. A.12, the source is a BAL quasar, with broad absorption linesm especially in the C IVλ1549 and Si IVλ1397 regions. Hazard et al. (1984) also report broad absorption lines in Al IIIλ1860 that we can see on the blue side of the blend at $\lambda \approx 1820$ Å.

A.13. B1422+231

The source was studied in detail for the first time by Patnaik et al. (1992). It consists of a gravitationally lensed system with a diameter of 1.3 arcsec and four non-resolved components from VLA observations. This quasar is lensed into four images by a galaxy with $z = 0.34$ (Tonry 1998). Dadina et al. (2016) used XMM-Newton to study the matter inflow at the centre of this source and found that its X-ray spectrum is quite similar to the one of a typical Seyfert galaxy. Several UV spectra were found in literature (Tonry 1998; Assef et al. 2011; Kundic et al. 1997; O'Dowd et al. 2017), but are not available for public usage or do not correspond to the regions we want to analyze. No SDSS spectrum was found. It has also been analysed in the infrared by Lawrence et al. (1992) who conclude that the source presents similar structures in both radio and infrared. This is one of the radio-loud sources included in our sample.

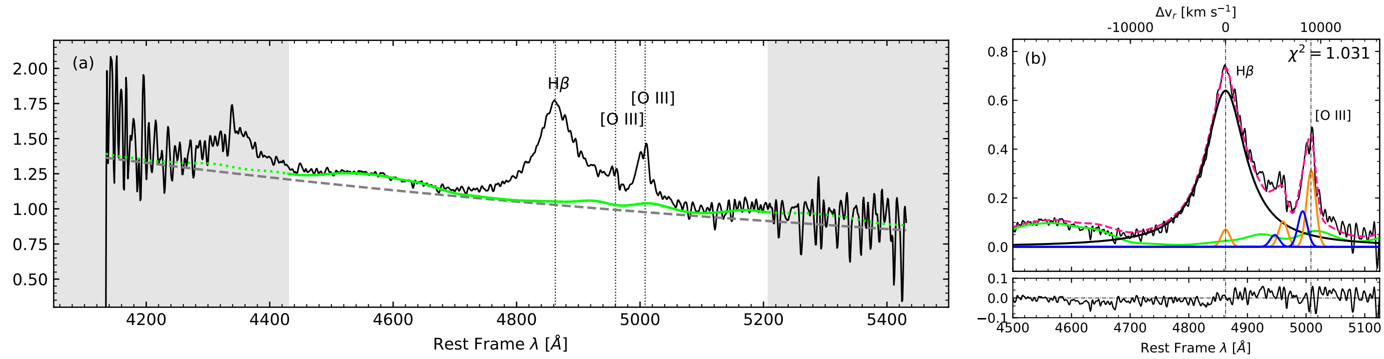

Fig. A.13. B1422+231. Colours and lines as the same as in Figure A.1.

A.14. SDSSJ153830.55+085517.0

When compared with the other sources of the sample, this source presents one of the spectra with lowest S/N. The low S/N might be due to the presence of a star that is located very close to the field of the quasar significantly increasing the background of the spectrum. This also may explain why the UV and the optical spectra of SDSSJ153830.55+085517.0 differ so much: while the optical spectrum shows a Pop. B-like profile, the UV is clearly the expected one for a Pop. A3 quasar. If this discrepancy is real, this would be the first case of discordant population classification from the UV and from the optical spectrum. SDSSJ153830.55+085517.0 had the 1900 Å blend fit as Pop. A since it cannot reproduce any Pop. B model and its UV spectrum presents all the characteristics of a Pop. A quasar. SDSSJ153830.55+085517.0 has previous observations in the *K*-band at LBT (Vietri et al. 2018) and at UKIRT by Dix et al. (2020). In both cases, our NIR spectrum is compatible with those shown for the Hβ region by these authors. As we remarked before, the UV spectrum obtained with BOSS shows a blend at 1900 Å characteristic of the extreme end of Pop. A. An additional old UV SDSS spectrum exists, but it has no information on the 1900 Å blend. A new UV spectrum would be necessary to disentangle its classification and possible peculiarity. Additionally, Bruni et al. (2019) has classified this source as a high-velocity BAL.

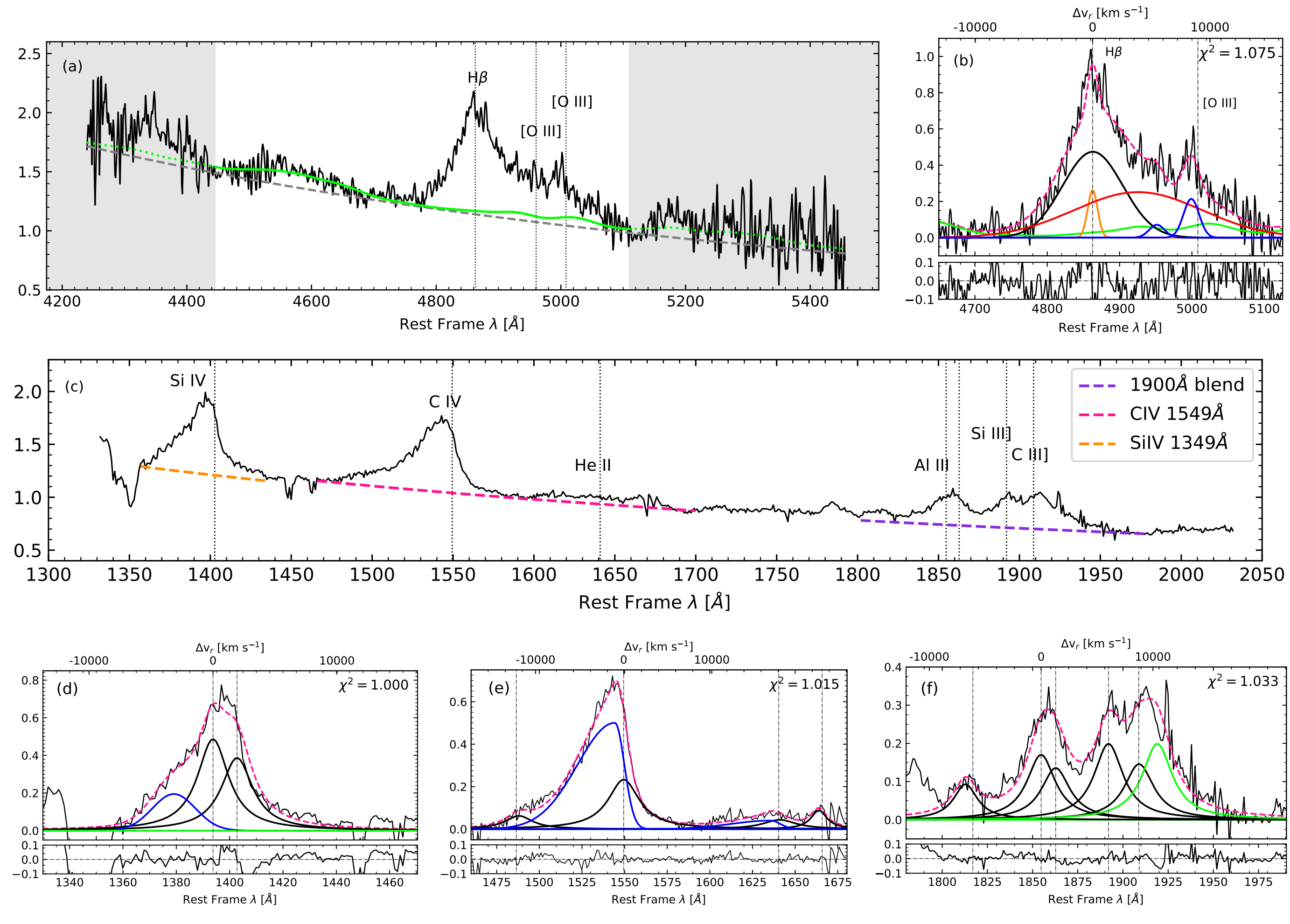

Fig. A.14. SDSSJ153830.55+085517.0. Same details as in Figure A.6.

A.15. SDSSJ161458.33+144836.9

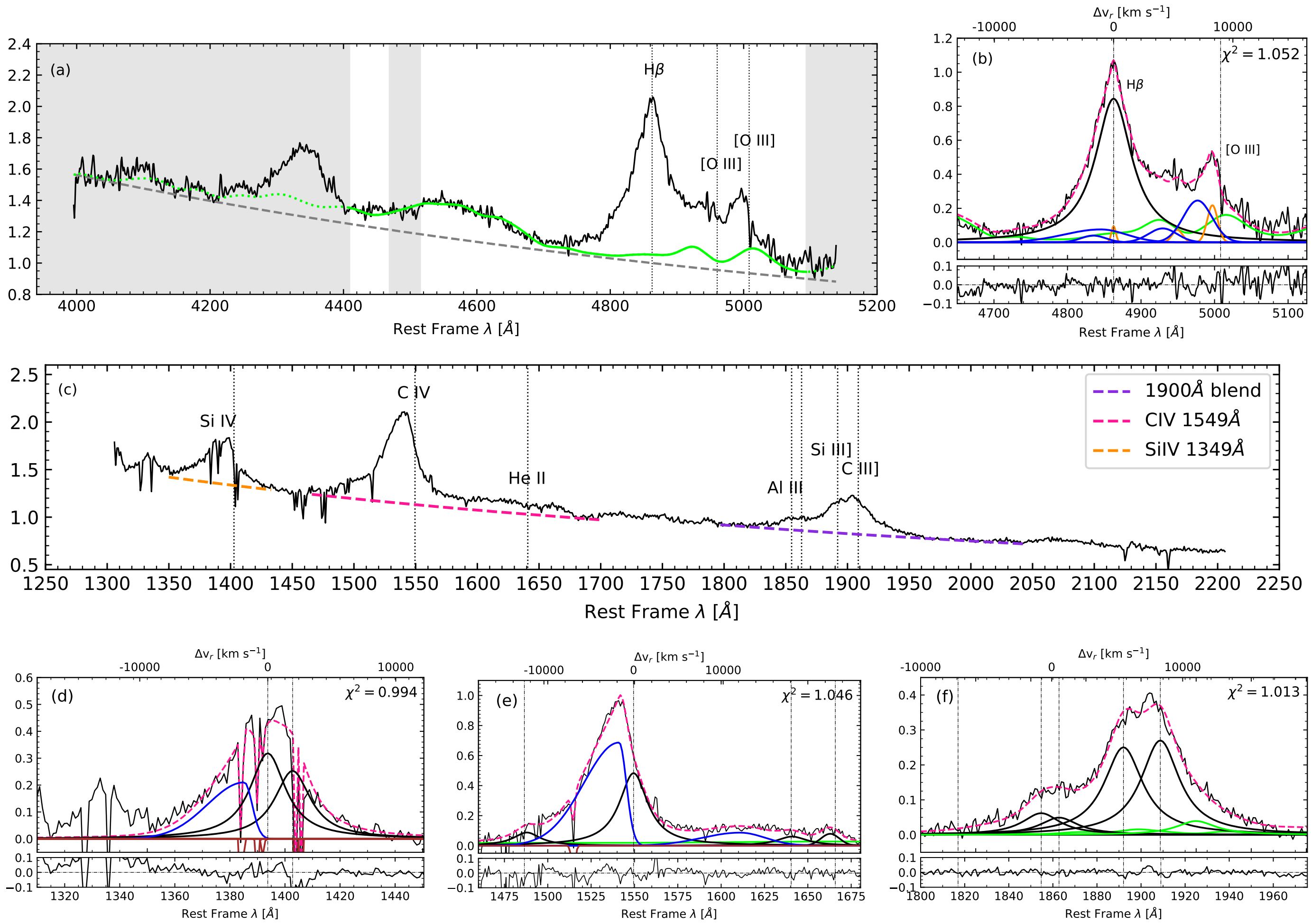

Fig. A.15. SDSSJ161458.33+144836.9. Same details as in Figure A.6.

A.16. PKS 1937-101

This object shows a very faint Fe II emission, as is typical of A1 spectra. A UV spectrum from the MOJAVE/2CM atlas for this source is presented in Torrealba et al. (2012). It is also one of the strongest radio-loud sources analysed in this work. Data from the Parkes 2.7 GHz Survey are shown in Savage et al. (1990). PKS 1937-101 is seen as a compact radio source after analysis of VLBI data (Lee et al. 2016). Brinkmann & Siebert (1995) has reported PKS 1937-101 as one of the most distant objects detected with the ROSAT survey (Voges 1993).

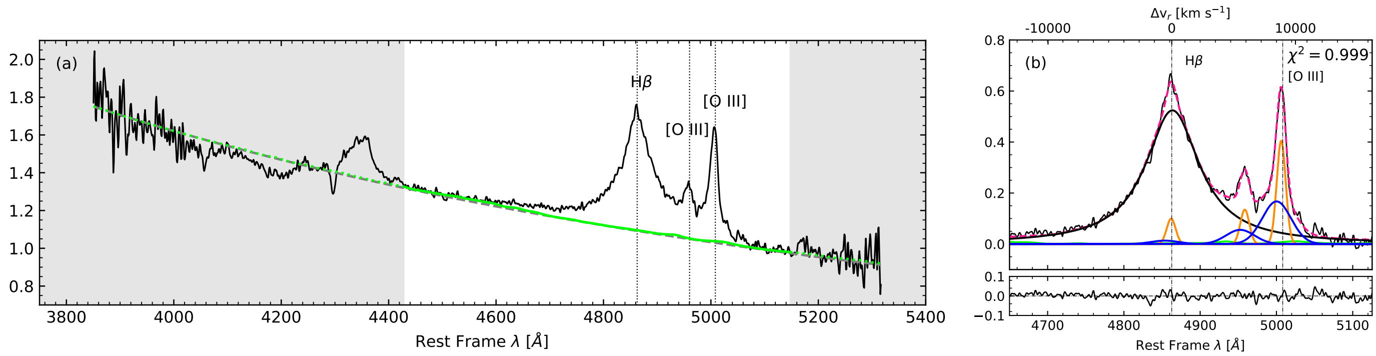

Fig. A.16. PKS 1937-101. Colours and lines as Figure A.1.

A.17. PKS 2000-330

The UV spectrum used in the fittings was obtained through the digitisation of the spectrum from Barthel et al. (1990). However, since this spectrum presents a small wavelength range that does not account either for the 1900 Å blend or for He IIλ1640, we analyse only the Si IVλ1397 and C IVλ1549 emission lines. A detailed comparison between this source and Q 1410+096 is performed in Deconto-Machado et al. (2022).

This quasar is the strongest radio-loud source from the present sample (Savage et al. 1990). The position of this source is not within the area covered by the FIRST catalogue.

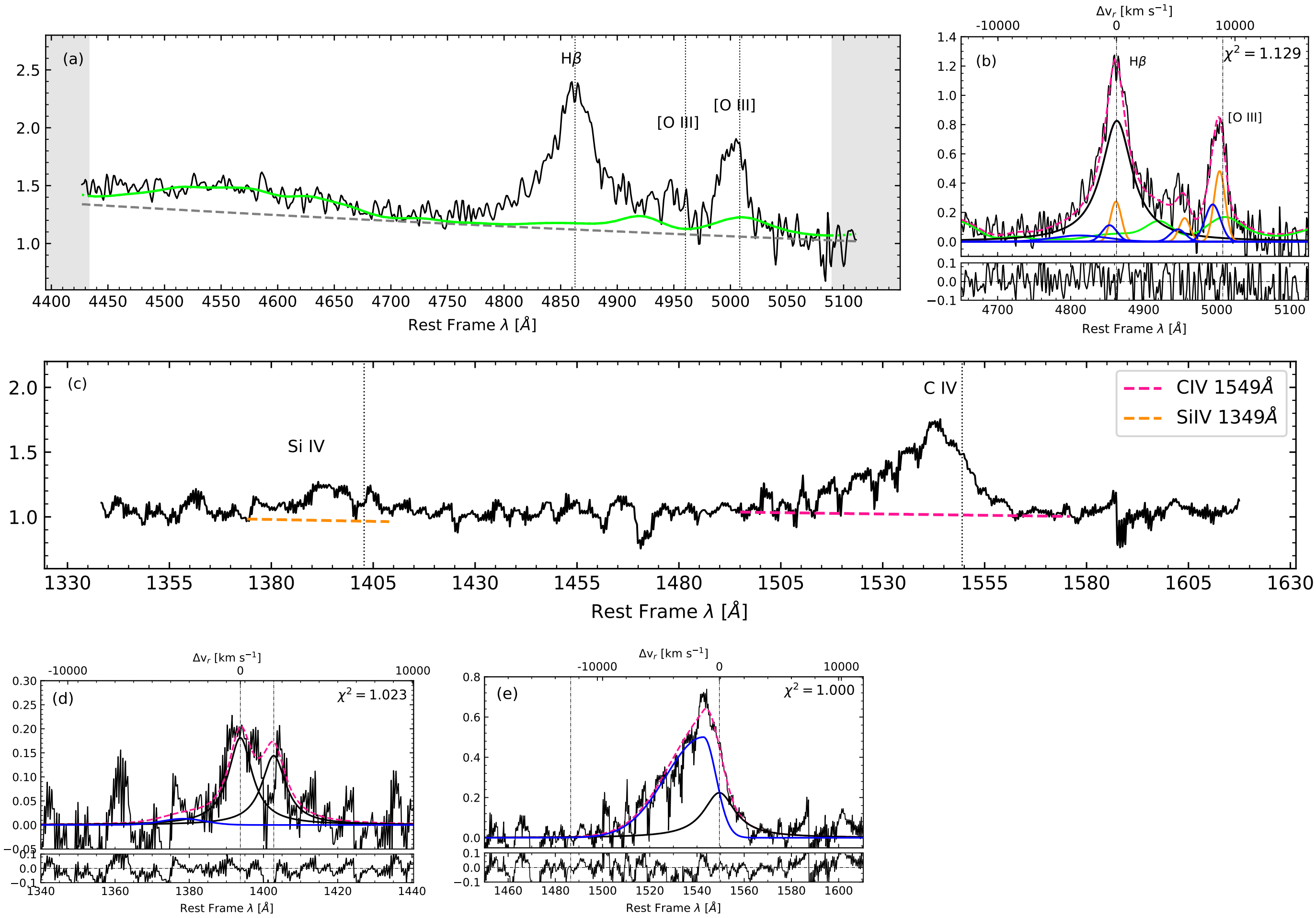

Fig. A.17. PKS 2000-330. *Top panels:* Same details as in Figure A.6. *(c)* UV spectrum. *Bottom panels:* Fits for (d) Si IVλ1397 and (e) C IVλ1549. The UV spectrum was digitised from Barthel et al. (1990).

A.18. SDSSJ210524.49+000407.3

This source presents a $W([\mathrm{O\,III}]) \approx 0.45$ Å. The low equivalent width makes it difficult to discern what corresponds to [O III]$\lambda\lambda$4959,5007 and to Fe II.

The UV region of this source is very unwieldy because of very broad absorption lines shortwards of C IVλ1459. For the 1900 Å blend, we present two different fittings, one including blueshifted components for Al IIIλ1860 and Si III]λ1892 and another without these lines. The motivation here is that if we do not include blueshifted components then the BC of the lines present a displacement of $-1640\,\mathrm{km\,s^{-1}}$, which can be seen as an indicative of some outflowing gas.

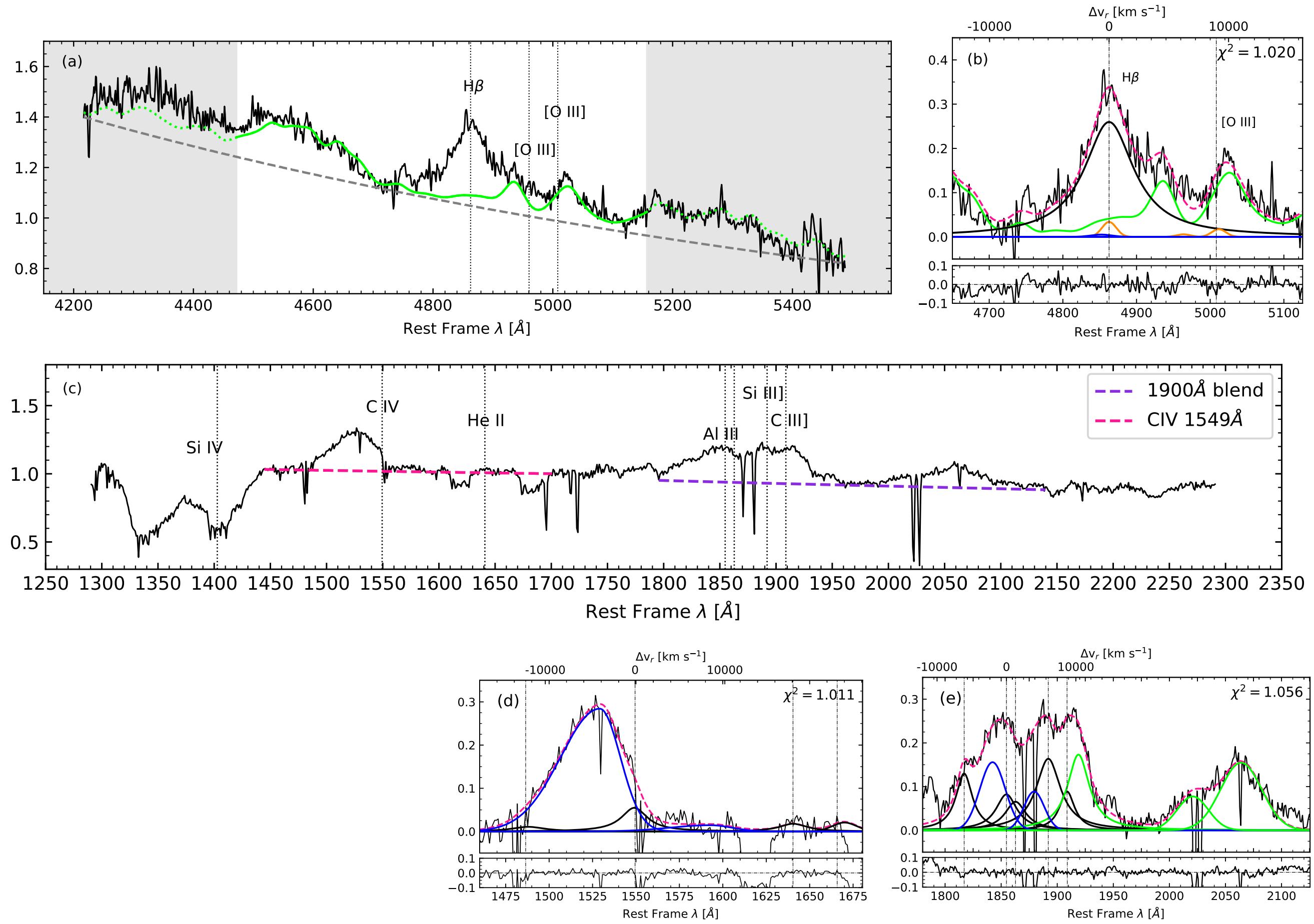

Fig. A.18. SDSSJ210524.49+000407.3. *Top panels:* Colours and lines as in Figure A.1. *(c)* SDSS UV spectrum. *Bottom panels:* Fits for (d) C IVλ1549 and (e) the 1900 Å blend.

A.19. SDSSJ210831.56-063022.5

This is another case in which the Fe II contribution is estimated through the red side of the spectrum. It is difficult to set the [O III]$\lambda\lambda$4959,5007 NC at rest-frame since the region close to these lines is dominated by the Fe II multiplets. Differently from the other Pop. A3 of the sample (SDSSJ005700.18+143737.7 and SDSSJ210524.49+000407.3), for this quasar it was not possible to reach a good χ^2, without including blueshifted components for Al IIIλ1860 and Si III]λ1892. SDSSJ210831.56-063022.5 is a source that presents one of the widest Hβ BC of the sample. It could be that in this case the Hβ BLUE component has been underestimated, since we do find strong blueward asymmetries in the three fitted UV profiles.

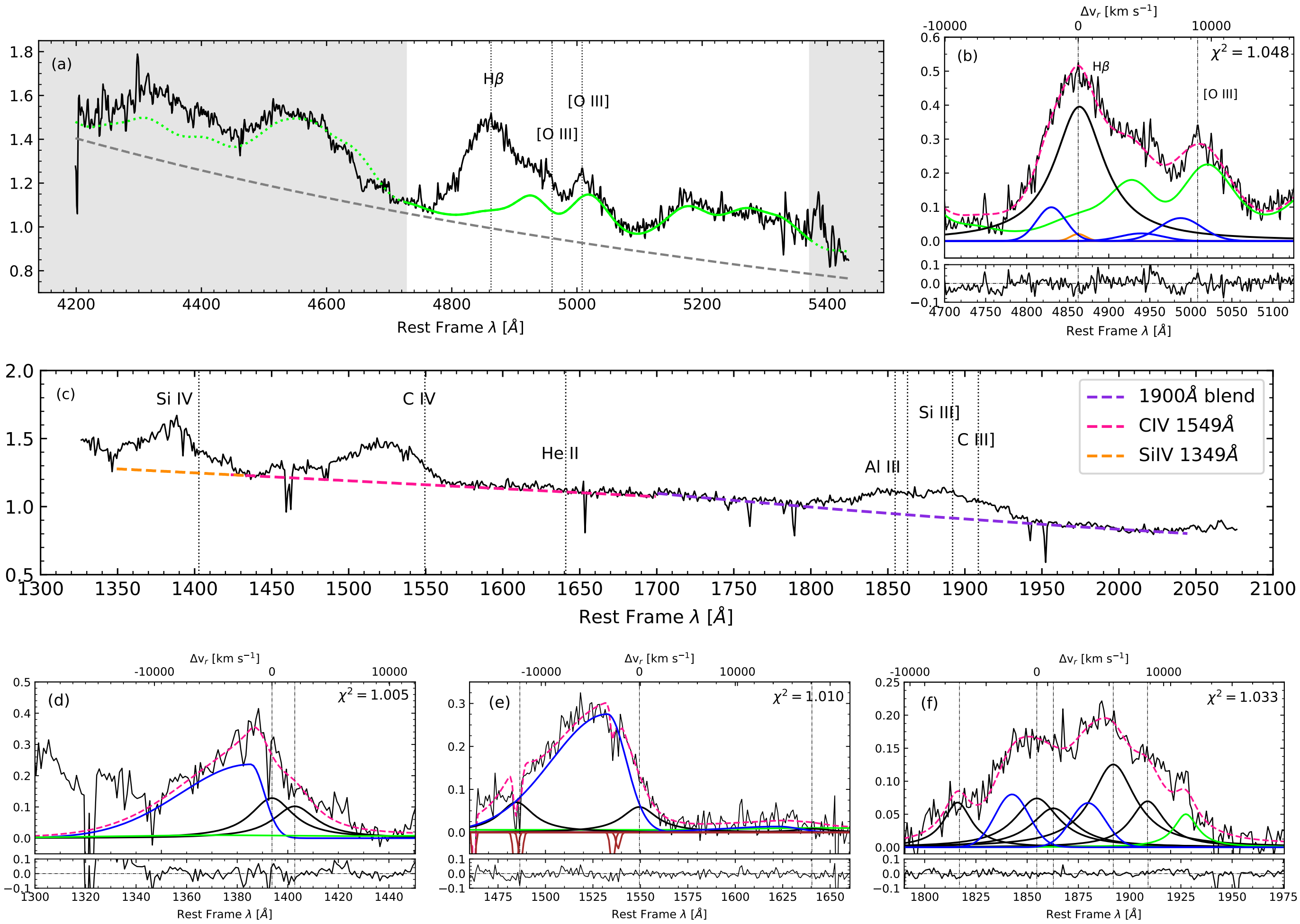

Fig. A.19. SDSSJ210831.56-063022.5. Same details as in Figure A.6.

A.20. SDSSJ212329.46-005052.9

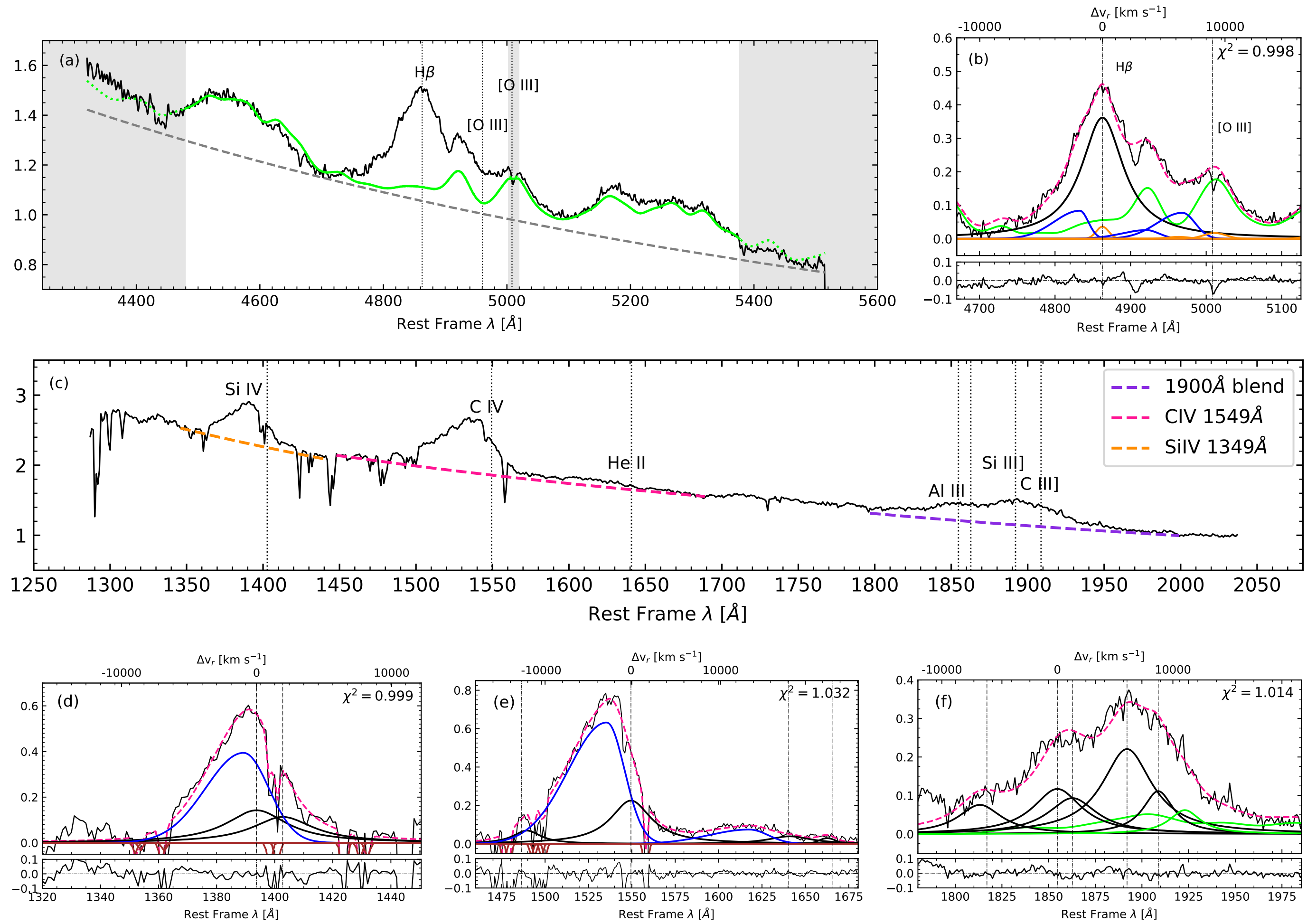

Fig. A.20. SDSSJ212329.46-005052.9. Same details as in Figure A.6.

A.21. PKS 2126-15

This object has been observed in the two runs. Since both observations can be used and present good S/N, we create a new spectrum by combining the two of them through the IRAF task `scombine`. The Fe II multiplets were fitted based on the shape seen in the red side of Hβ due to the fact that the blue side of Hβ is affected by noise and is almost at the border of the spectrum. In order to account for the [O III]$\lambda\lambda$4959,5007 contributions, it was necessary to include two blueshifted components, as can be seen in Fig. A.21. Some UV spectra were found but they do not include the regions we are interested in. PKS 2126-15 is also one of the four radio-loud quasars from the sample.

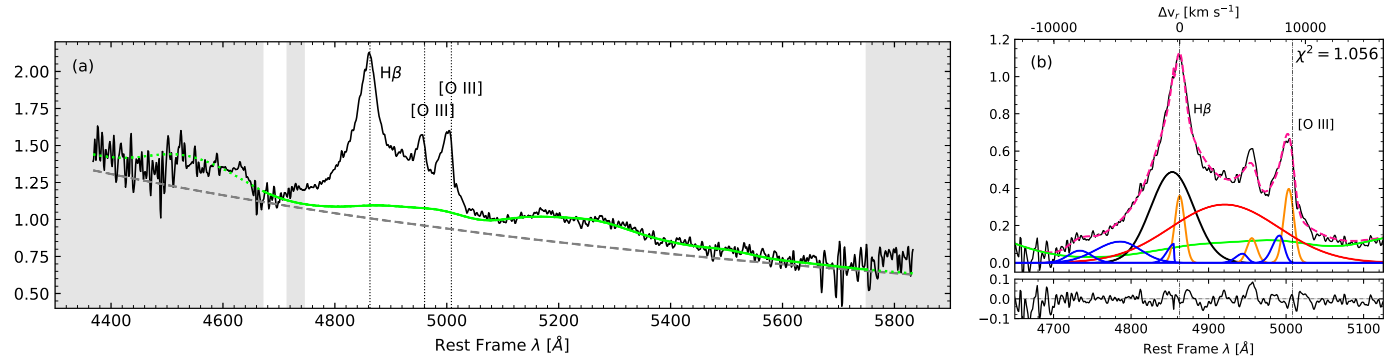

Fig. A.21. PKS 2126-15. Colours and lines are the same as in Figure A.1.

A.22. SDSSJ235808.54+012507.2

The spectrum of this source is of low S/N when compared with the other sources of the sample, which makes it difficult to find the correct intensity of the continuum. As a consequence, caution should be taken when considering the location of the continuum and the Fe II contribution especially in the blue part of the spectrum.

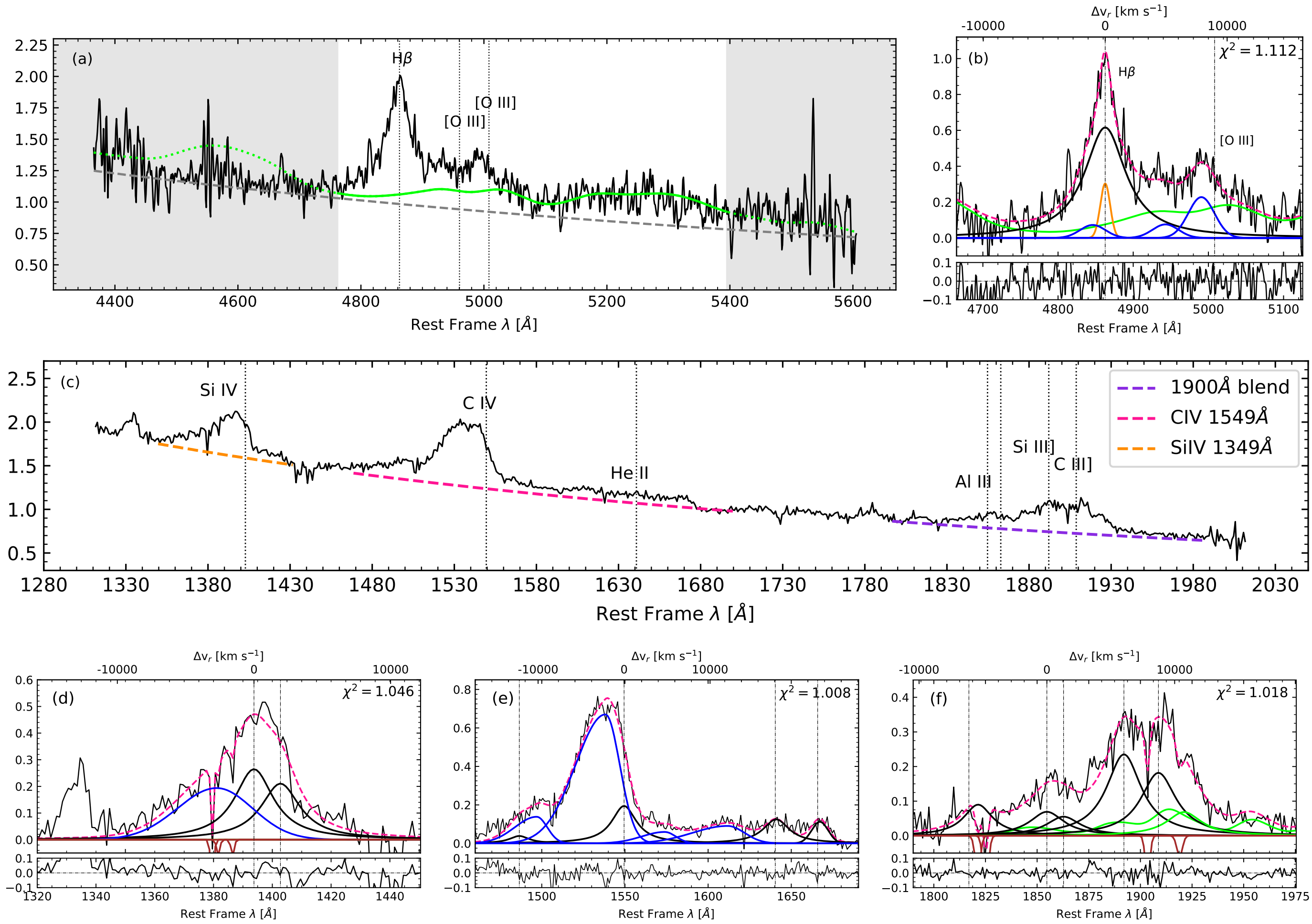

Fig. A.22. SDSSJ235808.54+012507.2. Same details as in Figure A.6.